



Physics and Mathematics

Synthesis and characterization of nano particles decorated graphene oxide via pulsed laser ablation technique

A Thesis submitted in partial fulfillment of the requirements of the degree of

Master of Science in Engineering Mathematics and physics

(Engineering Physics)

by

Basma Saeed Hassan Ali

Bachelor of Science in Electrical Engineering

(Electrical Power and Machines Engineering)

Faculty of Engineering, Benha , 2019

Supervised By

Prof. Sohair EL-Sayed Negm

Prof. Saeed Abdallah Abdelhalim

Dr. Horia Fawzi

Cairo (2026)



Physics and Mathematics

department

Synthesis and characterization of nano particles decorated graphene oxide via pulsed laser ablation technique

by

Basma Saeed Hassan Ali

Bachelor of Science in Electrical Engineering

(Electrical Power and Machines Engineering)

Faculty of Engineering, Benha University, 2019

Examiners' Committee

Name and Affiliation

Signature

Prof. Sohair El-Sayed Negm

.....

Physics and Mathematics , Benha University

Prof. Samia Saafan

.....

Physics department, faculty of science, Tanta University

Prof. Ahmed Bakr

.....

Basic science department, faculty of Technology of Education,

Helwan University

Prof. Saeed Abd-Allah

.....

Physics and Mathematics , Benha University

Statement

This thesis is submitted as a partial fulfillment of Master of Science in physics, Department of Mathematics and Engineering Physics, Faculty of Engineering-Shoubra, Benha University.

The author carried out the work included in this thesis, and no part of it has been submitted for a degree or a qualification at any other scientific entity.

Student name

Basma Saeed Hassan Ali

Signature

.....

Researcher Data

Name : Basma Saeed Hassan Ali.....

Date of birth : ...5/4/1995.....

Place of birth : ...Cairo-Egypt.....

Last academic degree : Bachelor of Science in Electrical Engineering

Field of specialization : Engineering physics.

University issued the degree : Benha University.....

Date of issued degree : 2019.....

Current job : Demonstrator

ABSTRACT

The Au@Fe₃O₄/GO nanocomposites (NC) have superior catalytic capability that makes it promising for the construction of other electrochemical sensors and bioanalysis. It is also suitable for photonic applications, drug delivery applications, and water treatment applications. In this work, we succeeded in synthesizing and characterizing Au@Fe₃O₄/GO NC using an alternative-novel, easy, low cost and nontoxic technique which is pulsed Laser ablation in liquid (PLAL). GO nanosheets were prepared in liquid by PLAL and investigated using high transmission electron microscope (HRTEM), the functional groups were detected using Fourier transform infrared spectroscopy (FTIR). The optical absorption spectra of the sample were measured using UV-visible spectrometer. Magnetite (Fe₃O₄) was loaded on GO, by using the same technique to form Fe₃O₄/GO NCs. Also Au@Fe₃O₄/GO nanocomposites (NCs) was synthesized by PLAL with different Au@Fe₃O₄ to GO ratios (S1=1:1, S2=1:2, S3=1:3 and S4=1:4). The nanocomposites were also characterized by the same ways. The optical parameters: optical conductivity (σ), absorption coefficient (α), bandgap (E_g), Urbach energy (E_U), electronegativity (Δx), refractive index (n), steepness parameter (σ_s), electron-phonon interaction (E_{e-p}), electronic polarizability (α_e) and molar electronic polarizability (α_{me}) were calculated. They were enhanced by adding Fe₃O₄ NC and a further enhancement took place by adding Au.

Furthermore, the thermal parameters: thermal diffusivity (α), thermal effusivity (e), and thermal conductivity (k) for GO, Fe₃O₄/GO Au@Fe₃O₄/GO NCs were measured using photoacoustic (PA) technique. The results show that there is an enhancement of α , e and k for Au@Fe₃O₄/GO NCs than those of GO and Fe₃O₄/GO.

The thermal parameters of Au@Fe₃O₄/GO with different GO concentrations are also measured using PA technique. The results show there is 80 % decrease in k as the ratio of GO increased to Au@Fe₃O₄ NCs.

ACKNOWLEDGMENTS

First and foremost, I am deeply thankful to Allah for giving me the ability to accomplish this work., I am sincerely thankful to my main supervisor, **Prof. Dr. Sohair Negm**, for her valuable guidance, steady support, and insightful feedback throughout this research journey. Her expertise, encouragement, and patience have been instrumental in shaping this thesis.

Furthermore, I would like to express the sincerest gratitude to my supervisor, **prof. Dr. Said Abdalh** for his guidance and support during my research. He constantly encouraged me to learn theoretical knowledge and technologies, allowed me to make mistakes, and most importantly, provided me with an opportunity to explore. Without his supervision and constant help, this thesis would not have been possible.

I extend my heartfelt appreciation to my friend and supervisor, **Dr. Horia Fawzy**, for her constructive criticism, valuable suggestions, and scholarly visions, which have significantly enriched the quality of this work. In addition, I am grateful for the opportunity to work with the mentioned board as teammates and the weekly meeting from the beginning of this research.

I am thankful to **my family** for their solid love, encouragement, and understanding throughout this academic endeavor, especially **my husband**, for his unlimited support and cooperation. His constant support and belief in my abilities has been my source of strength and motivation. I acknowledge with gratitude all those who have directly or indirectly contributed to the completion of this thesis. Their support and encouragement have been indispensable, and I am truly grateful for their assistance.

Basma said

Table of Contents

Abstract	1
Acknowledgment	2
Table of Contents.....	3
List of Tables.....	6
List of Figures	7
List of Abbreviations.....	11
Chapter 1: Introduction.....	13
1.1 Overview	13
1.2 Graphene	13
1.3 Graphene oxide (GO)	15
1.4 Decorating materials (Fe_3O_4 & $\text{Au}@$ Fe_3O_4)	17
1.5 Pulsed laser ablation technique (PLA)	18
1.6 Pulsed laser ablation technique in liquid (PLAL)	20
1.7 Aim of the work	20
1.8 Organization of the thesis	21
Chapter 2: literature survey.....	22
2.1 Graphene oxide	22
2.1.1 History of GO synthesis.....	22
2.1.2 structural models of GO	23
2.1.3 Modern ways of GO synthesis	25
2.1.4 Applications of graphene oxide.....	26
2.2 Magnetite (Fe_3O_4)	27
2.2.1 Applications of Fe_3O_4 /GO NCs.....	28
2.3 Gold nanoparticles	29

2.4 Gold-Magnetite nanocomposite.....	30
2.4.1 Applications of Au@Fe ₃ O ₄ /GO NCs.....	31
2.5 Laser Ablation	32
2.5.1 Laser Ablation In Liquid Medium	42
2.6 Photoacoustic Effect	43
2.6.1 PA Theory.....	44
2.7 Some important related papers in Literature	47
Chapter 3: Experimental work	53
3.1 Materials	53
3.2 Pulsed Laser Ablation System.....	53
3.3 General Experimental Process	53
3.4 Laser source and Measuring devices	55
3.4.1 Nd-YAG Laser.....	55
3.4.2 UV-Visible Spectrophotometer	57
3.4.3 High Resolution Transmission Electron Microscope (HRTEM)	58
3.4.4 Fourier Transform Infrared Spectroscopy (FT-IR)	59
3.4.5 Photoacoustic Characterization	63
Chapter 4: Result and Discussion	68
4.1 characterization of GO nanosheets	68
4.1.1 Transmission Electron Microscopy	68
4.1.2 Fourier Transform Infrared spectroscopy	70
4.1.3 UV-Vis Absorption spectra	70
4.2 Characterization of Fe ₃ O ₄ /GO NCs	72
4.2.1 Transmission Electron Microscopy	72
4.2.2 Fourier Transform Infrared spectroscopy	74
4.2.3 UV-Vis Absorption spectra	77
4.3 Characterization of Au@Fe ₃ O ₄ /GO NCs.....	79
4.3.1 Characterization of of Au@Fe ₃ O ₄ NCs.....	80
4.3.1.1 Transmission Electron Microscopy.....	80

4.3.1.2 Fourier Transform Infrared spectroscopy.....	80
4.3.1.3 UV-Vis Absorption spectra.....	81
4.3.2 Characterization of Au@Fe ₃ O ₄ /GO NCs.....	83
4.3.2.1 Transmission Electron Microscopy.....	84
4.3.2.2 Fourier Transform Infrared spectroscopy.....	85
4.3.2.3 UV-Vis Absorption spectra.....	86
4.4 Optical properties of GO, Fe ₃ O ₄ /GO and Au@Fe ₃ O ₄ /GO NCs.....	87
4.5 Thermal properties of GO, Fe ₃ O ₄ /GO and Au@Fe ₃ O ₄ /GO NCs.....	95
4.5.1 Thermal properties of Au@Fe ₃ O ₄ /GO NCs with different concentration of GO...98	
Conclusion	102
References	104

List of Tables

Table 3-1: Quanta-Ray lab 150 series energy per pulse.	56
Table 3-2: Quanta-Ray lab 150 series pulse width.	56
Table 3-3: Quanta-Ray lab 150 series beam specifications	56
Table 4-1 : Bandgap (E_g), Urbach energy (E_u), electronegativity (ΔX), refractive index (n), steepness parameter (σ_s), electron phonon interaction (E_{e-p}) of GO, Fe_3O_4/GO and $Au@ Fe_3O_4/GO$ NC respectively.....	92
Table 4-2: Electronic polarizability (α_e), molar volume (v_m), molar refraction (R_m) and molar electronic polarizability (α_{me}) of GO, Fe_3O_4/GO and $Au@Fe_3O_4/GO$ NC respectively.....	94
Table 4-3: Thermal diffusivity (α_t), thermal effusivity (e) and thermal conductivity (k) of GO, Fe_3O_4/GO and $Au@Fe_3O_4/GO$ NC respectively.....	97

List of figures

Figure 1.1: Schematic diagram of graphene structure, graphite, carbon nanotubes and buckyballs.....	13
Figure 1.2: Schematic diagram of sigma and the overlapping pi bonding of carbon atoms.....	14
Figure 1.3: Graphene and graphene oxide.....	16
Figure 1.4: Bottom-up assembly and top-down fabrication.....	18
Figure 1.5: Laser ablation setup technique.....	19
Figure 2.1: Summary of several older structural models of GO.....	25
Figure 2.2: Micro spinel structure of Fe_3O_4	28
Figure 2.3: Ferrofluids under external magnetic field.....	29
Figure 2.4: The schematic diagram of a typical experimental setup for PLAL..	33
Figure 2.5: Laser power as a function of pulse frequency for a commercial DPSS laser.....	35
Figure 2.6 : a) Effect of nanosecond laser, b) femtosecond laser, and their SEM image at c) and d) respectively.....	37
Figure 2.7: Gaussian beam profile and the expression for calculating the beam intensity as a function of radial position.....	38
Figure 2.8: The focal region of a laser beam and the expressions for calculating the minimum spot diameter and the depth of focus.....	39
Figure 2.9: Changes in spot overlap as the effect of different values of spot diameter, pulse frequency and writing speed.....	40
Figure 2.10: Spot overlap as a function of distance from the center line of a track written with a circular laser spot.....	41
Figure 2.11: Cross-sectional view of cylindrical photoacoustic Cell.....	45
Figure 3.1 Experimental setup for nanoparticles synthesis, by laser ablation technique..	53
Figure 3.2: Experimental set up of GO preparation.....	54

Figure 3.3: The preparation steps of Fe ₃ O ₄ /GO NCs.....	54
Figure 3.4: The preparation steps of Au@Fe ₃ O ₄	55
Figure 3.5: Schematic diagram of synthesized Au@Fe ₃ O ₄ / GO nano fluid.....	55
Figure 3.6: Photograph of (a) V-670 UV-Vis Spectrophotometer, (b) specular reflectance accessory, and (c) integrating sphere accessory.....	58
Figure 3.7: (a) Photograph and (b) ray diagram for HRTEM, Model JEOLJEM-2100 and (c) Image of a grid used in sample preparation for TEM.....	59
Figure 3.8: The different types of vibrations in infrared spectroscopy.....	60
Figure 3.9: The three main measurement techniques Transmission, Attenuated Total Reflection (ATR), and Reflection respectively.....	62
Figure 3.10: Alpha II FTIR with Platinum ATR Module.....	62
Figure 3.11: A schematic diagram of photoacoustic technique.....	63
Figure. 3.12: Extra support screws installed at the front of the detector.....	64
Figure 3.13: Sample holder with brass inserts and small and large cups.....	64
Figure 3.14: Lack- in amplifier model (SR 830).....	65
Figure 4.1: HRTEM images of GO at different resolutions a) 200 nm, b) 20 nm and SAED image at 5 nm.....	68
Figure 4.2: FT-IR spectra of the prepared GO nanosheets.....	70
Figure 4.3: The absorption spectra of the prepared GO nanosheets.....	71
Figure 4.4: Variation of $(\alpha h\nu)^2$ with the photon energy (h ν) for GO.....	72
Figure 4.5: HRTEM images of Fe ₃ O ₄ NPs at different resolutions a) 100 nm, b) 20 nm inset image in a) is the histogram of NPs.....	72
Figure. 4.6: HRTEM images of Fe ₃ O ₄ /GO NCs at different resolutions a) 100 nm, b) 50 nm the inset figures in a) and b) include the SAED images.....	73

Figure. 4.7: HRTEM images of Fe ₃ O ₄ /GO NCs at different resolutions a) 200 nm, b) 50 nm. The inset figures include SAED image at 5 nm.....	74
Figure. 4.8: FT-IR spectra of the prepared Fe ₃ O ₄ NPs and Fe ₃ O ₄ /GO NCs.....	75
Figure. 4.9: FT-IR spectra of the prepared Fe ₃ O ₄ /GO NCs at 5, 10, 15, 20, 25 and 30 min.....	76
Figure. 4.10: FT-IR spectra of the prepared Fe ₃ O ₄ /GO NCs at 20, 25 and 30 min.....	77
Figure. 4.11: The absorption spectra of the prepared Fe ₃ O ₄ and its band gap (a,b) respectively.....	78
Figure4.12: The absorption spectra of the prepared Fe ₃ O ₄ /GO and its band gap (a,b)..	79
Figure. 4.13:HRTEM images of Au@Fe ₃ O ₄ NCs at different resolutions a) 200 nm, b) 20 nm . the inset image is at resolution 5 nm.....	81
Figure 4.14: FT-IR spectra of the prepared Au@ Fe ₃ O ₄ NCs.....	81
Figure 4.15: The absorption spectra of the prepared Au@Fe ₃ O ₄ NCs for different ablation time.....	82
Figure 4.16: The absorption spectra of the prepared Au, Fe ₃ O ₄ and Au@Fe ₃ O ₄ NCs...	83
Figure. 4.17: HRTEM images of Au@Fe ₃ O ₄ / GO NCs at different resolutions 200 nm, 20 nm . a) without sonication, b) with 30 min. sonication.....	84
Figure 4.18: FT-IR spectra of the prepared Au@Fe ₃ O ₄ /GO NCs with sonication.....	84
Figure 4.19: a) The absorption spectra of the prepared Au@Fe ₃ O ₄ /GO NCs at different GO concentration.....	87
Figure4.20: Absorption spectra of GO, Fe ₃ O ₄ /GO and Au@ Fe ₃ O ₄ /GO NCs.....	88
Figure 4.21: a) Absorption coefficient curve of GO, Fe ₃ O ₄ /GO and Au@ Fe ₃ O ₄ /GO NCs. b) Variation of $(\alpha hv)^2$ with the photon energy (hv)of GO, Fe ₃ O ₄ /GO and Au@Fe ₃ O ₄ /GO NCs.....	89
Figure4.22: Variation of the optical band gap (E_g) and Urbach energy (E_u) of GO, Fe ₃ O ₄ /GO and Au@Fe ₃ O ₄ /GO NCs.....	90

Figure 4.23: Variation of both steepness parameter (σ_s) and electron-phonon interaction (Ee-p) of GO, Fe ₃ O ₄ /GO and Au@Fe ₃ O ₄ /GO NCs.....	91
Figure 4.24: Optical conductivity spectrum of GO, Fe ₃ O ₄ /GO and Au@Fe ₃ O ₄ /GO NC.....	93
Figure 4.25: Tan ϕ -1 with $f^{-1/2}$ of a) GO, b) Fe ₃ O ₄ /GO and c)Au@Fe ₃ O ₄ /GO NC.....	96
Figure 4-26: PA amplitude (q) versus (f) of a) GO, b) Fe ₃ O ₄ /GO and c)Au@Fe ₃ O ₄ /GO NC.....	97
Figure 4.27: The plot between[tan(ϕ) -1] with $(1/f)^{1/2}$ for (a)S1=1:1, b)S2=1:2, c)S3=1:3 and d)S4=1:4.....	99
Figure 4.28: PA signal vs. chopper frequency for a)S1, b)S2, c)S3 and d) S4.....	100

LIST OF ABBREVIATIONS

NPs	Nanoparticles
VB	Valence band
CB	Conduction band
FETs	Field effect transistors
GO	Graphene oxide
rGO	Reduced graphene oxide
Fe₃O₄	Magnetite
Au	Gold
MRI	Magnetic resonance imaging
PLA	Pulsed laser ablation
PLD	Pulsed laser deposition
PLAL	Pulsed laser ablation in liquid
PAS	Photoacoustic spectroscopy
PA	photoacoustic
HRTEM	High resolution transmission electron microscope
XRD	X-ray diffraction
FT-IR	Fourier transform - infrared
EDX	Energy dispersive X-ray spectroscopy
SEM	Scanning electron microscope
XPS	X-ray photoelectron spectroscopy
E_g	Energy bandgap
E_U	Urbach energy
DSM	Dynamic structural model
EGO	Electrochemical graphene oxide
SERS	Surface enhanced Raman scattering
NGO	Nanographene oxide
GQDs	Graphene quantum dots

PEG	Polyethylene glycol
CBA	Chemical bond approach model
FCC	Face-centered cubic
T_c	Curie temperature
LSPR	Localized surface plasmon resonance
SEF	Surface enhanced fluorescence
PTT	Photothermal therapy
PDT	Photodynamic therapy
IVD	In vitro diagnostics
DPSS	Diode pumped solid state
HAZ	Heat affected zones
QDs	Quantum dots
PL	Photoluminescence
NIR	Near infrared
MIR	Mid infrared
FIR	Far infrared
PMT	Photomultiplier Tube
PbS	Lead Sulfide
IRM	Included remote module
LCD	Liquid Crystal Display
ATR	Attenuated total reflection
IEC	International Electrotechnical Commission

Chapter 1

INTRODUCTION

Introduction

1.1 Overview

Nanotechnology evolved as the achievement of science in the 21st century. The synthesis, management, and application of materials with a particle size smaller than 100 nm fall under the interdisciplinary umbrella of this field. The significance of nanoparticles (NPs) in technological advancements is due to their adaptable characteristics and enhanced performance over their parent bulk material. Nanoparticles have lots of applications in different sectors such as the environment, agriculture, food, biotechnology, biomedical, medicines, etc. Among these different applications; treatment of waste water, environment monitoring, as a functional food additives and as a antimicrobial agents, for example, Silver nanoparticles exhibit strong antimicrobial activity against a wide range of microorganisms [1].

1.2 Graphene

Graphene is a single-layer 2-dimensional, one atom thick (~ 0.345 nm), material consisting of honeycomb lattice of sp^2 bonded carbon atoms. It is one form of carbon allotropes (Fig.1.1) such as 1D carbon nanotubes, 3D graphite, and 0D fullerenes. The 2010 Nobel Prize in Physics was shared by Andre K. Geim and Konstantin S. Novoselov for their work on graphene. They had isolated single layers of graphene in 2004. The method that they had used, basically using Scotch tape to pull the graphite apart, was simple and accessible, and provided samples still the best available. since then graphene has been subject to intense research by researchers and material scientists[2].

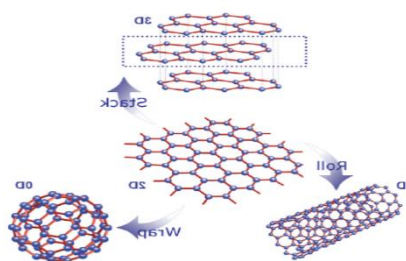


Figure 1.1: Schematic of grapheme structure, graphite, carbon nanotubes and bucky balls

As the sixth element in the periodic table, carbon has a $1s^2 2s^2 2p^2$ ground state electron configuration. For a carbon atom in graphene, the valence orbitals ($2s$, $2p^x$, $2p^y$, and $2p^z$) are sp^2 hybridized (i.e., the mixing of the single $2s$ orbital with two $2p$ orbitals), resulting in three planar σ orbitals separated by 120° with each other and one remaining $2p$ orbital ($2p^z$) oriented along the axis perpendicular to the graphene plane. Each of the three sp^2 orbitals of a carbon atom forms a σ bond with three neighbouring carbon atoms, thereby forming the hexagonal structure of graphene with a basis of two atoms per unit cell. The carbon-carbon σ bonds are strong covalent bonds, which are responsible for the lattice stability and for the elastic properties of graphene. The adjacent interaction among neighbouring $2p^z$ orbitals develops into delocalized π (bonding) and π^* (anti-bonding) bands Fig.1.2, which form the valence band (VB) and the conduction band (CB), respectively.

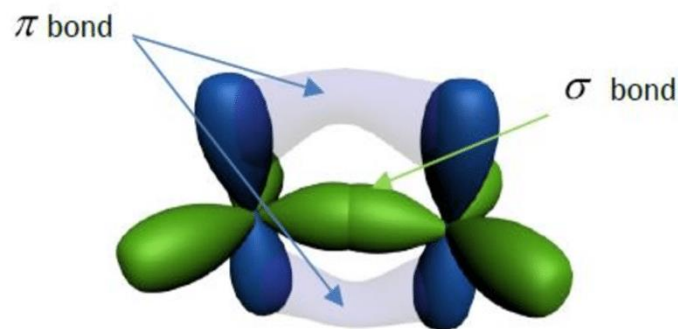


Figure 1.2: Schematic of sigma and the overlapping π bonding of carbon atoms.

Because of this electronic configuration graphene has extremely high electron mobility at room temperature with resistivity of $10^{-6} \Omega \cdot \text{cm}$, which is comparable to or even lower than that of silver ($1.62 \times 10^{-6} \Omega \cdot \text{cm}$), a material widely known for its lowest resistivity at room temperature, large carrier mobility (surpassing $20000 \text{ cm}^2 \text{ V}^{-1} \text{ s}^{-1}$), high thermal conductivity, high mechanical strength (e.g. 200 times greater than steel) and tensile modulus of 1 TPa [3].

Despite its numerous extraordinary properties and huge potential for various applications, one of the greatest challenges in using graphene as an electronic material is the lack of a sizable bandgap [4]. Graphene is intrinsically a zero-gap semiconductor, or a semimetal, it significantly limits the use of graphene in many applications where semiconducting materials with a suitable bandgap are required. For instance, the potential use of graphene in FETs for

digital logic applications has been extensively explored, because of the vast promise held by graphene, including its remarkably high carrier mobility, good transconductance, atomic layer thickness, and mechanical and chemical stability. However, the absence of a bandgap makes it difficult to completely switch off graphene FETs, leading to a low on/off current ratio. While dimensional down-scaling of silicon-based electronics is approaching its limit, semiconducting graphene with a sizable bandgap could potentially replace silicon in the next generation of high performance electronic devices [5]. Researchers have been searching for effective ways to produce semiconducting graphene and have developed various methods to generate a bandgap in graphene, in hopes of harnessing its exceptional properties for semiconductor-based applications, so they roughly categorized methods to produce semiconducting graphene into three groups: (1) morphological patterning of graphene sheets into nanoribbons, nano meshes, or quantum dots to induce quantum confinement (semiconducting nanocrystals often display strong variations in their electronic properties with size due to transformations in the density of electronic energy levels as a function of the size, which is known as the quantum confinement effect, or quantum size effect.) and edge effects; (2) chemical modification, doping, or surface functionalization of graphene to intentionally interrupt the connectivity of the π electron network. For example, if some carbon atoms are substituted by other atoms (e.g., N) in the hexagonal lattice, the lattice symmetry can break, resulting in the formation of a gap between π and π^* bands and (3) other methods e.g., use of two graphene layers arranged in Bernal stacking (or AB stacking) to break the lattice symmetry, and applying mechanical deformation or strain to graphene [6].

1.3 Graphene oxide

Graphene oxide (GO), a type of chemically modified graphene, can be mass-produced and is solution processable. Therefore, GO is a promising precursor for the bulk production of graphene related materials, e.g., semiconducting graphene. The presence of several types of oxygen functional groups (i.e., epoxide (=O) and hydroxyl (-OH) groups on the basal plane, and carbonyl (-C=O) and carboxyl (-COOH) groups on the sheet edge) (Fig.1.3) allows GO to interact with a wide range of organic and inorganic materials through non-covalent, covalent and/or ionic interactions, leading to functional hybrids and composites with unusual properties.

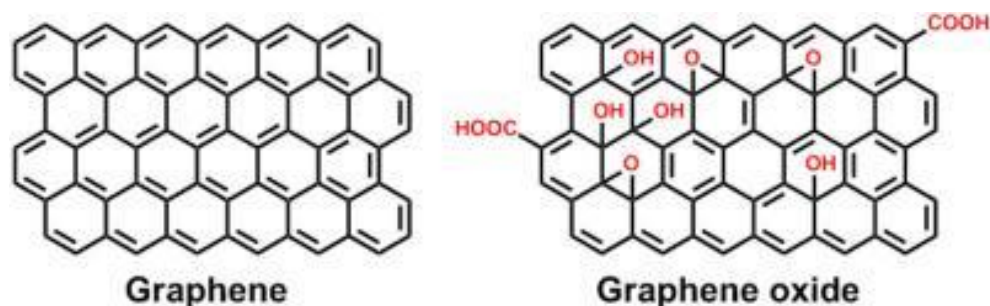


Figure 1.3: graphene and graphene oxide

In GO, most of carbon atoms bonded with oxygen is sp^3 hybridized, which disrupts the extended sp^2 conjugated network of original graphene sheet. The presence of considerable sp^3 carbons makes GO electrically insulating. Therefore, GO is an electronically hybrid material containing both conducting π -states from graphitic sp^2 hybridized carbons and a large energy gap between the σ -states of its sp^3 bonded carbons. The variation of the sp^2 and sp^3 carbon fractions by thermal or chemical treatments could be useful for manipulating its bandgap and therefore controllably transforming GO from an insulator to a semiconductor and ultimately to a graphene-like semi-metal [7]. Of course, reduction of GO further generates various types of defects in the graphene lattice, which affects the resulting transport properties. The disruption of the π network in graphene due to oxidation can open a direct electronic bandgap for graphene. The oxidized sites create strongly repulsive potential barriers for the π -electron wave functions, causing a quantum-confinement-like effect. In the infinite potential limit, a delocalized π -electron wave function will form nodes at these sites, whose spatial distribution will determine the presence or absence of a bandgap [8]. The average tensile modulus of graphene oxide sheet was determined to be 32 GPa [9]. Graphene oxide has potential utilization in various applications such as; renewable energies, electronic devices, transistors, sensors, and solar cells. Graphene oxide decorated with metal nanoparticles have always been amazing components which, owing to their chemical and physical properties, could be used in numerous areas of science such as; power storage, photonics, and catalysis. Graphene decorated by metal oxide and metal nanoparticles, in particular magnetite (Fe_3O_4 NPs) and Gold nanoparticles (Au NPs), displayed outstanding surface enhanced Raman scattering (SERS) efficiency owing to their great structural integrity and high density of locations across as well as between sheets [10].

1.4 Decorating materials (Fe_3O_4 & $\text{Au}@Fe_3O_4$)

Magnetite (Fe_3O_4) is earth abundant and environmentally friendly material. Fe_3O_4 has been extensively used in many fields since it has a high specific surface area, and good dispersion. The existence of trivalent and divalent iron ions (Fe^{3+} and Fe^{2+}) with equal numbers in Fe_3O_4 structure provides higher light absorption and consequently superior electrocatalytic activities and high performance in solar cells compared to other iron oxides[11]. Magnetic nanoparticles are nowadays the subject of extensive research because of their applications in many different technological areas and in particular, biomedicine. In this sense, iron oxide is an ideal material because of its biocompatibility and easy removal from the body after its use following natural routes. Iron oxide nanoparticles in the form of colloidal suspensions have already found application as contrast agents for magnetic resonance imaging (MRI). Moreover, properly conjugated with molecules that have an affinity to tumour cells [12]. Noble metal nanoparticles are having distinct properties compared to other metallic nanoparticles due to their optical, electronic and molecular recognition properties. Additionally they have large optical field enhancements due to the resonant oscillation of their free electrons in the presence of light. Because of these properties noble metal nanoparticles are greatly utilized in optical, imaging, sensors, cosmetics cancer therapy, and drug delivery. Among these noble metals, gold and gold nanoparticles are precious, inert and not easily oxidized when exposing to oxygen or highly acid environments. Gold nanoparticles exhibit different colours such as red, blue or other colours depending on their size, shape and amount of aggregation. Lately, significant efforts have been dedicated to the preparation of multifunctional nanomaterials. Joining diverse properties into one material is the main character of multifunctional materials. These materials including at least two distinct materials acquire properties from their individual segments, and they have distinctive multifunctional features. Therefore, $\text{Au}@Fe_3O_4$ as one of the important multifunctional nanocomposite nanoparticles have gained a great attention in recent years, such as it combines the magnetic properties of Fe_3O_4 with the surface plasmon resonance of Au nanoparticles[13]. $\text{Fe}_3\text{O}_4@Au/rGO$ nanocomposite with high light absorption in NIR region has many applications from catalysis, optics to nanomedicine. Recently, Soysal et al. [55] synthesize of $GO-Fe_3O_4-PANI$ nanocomposite as photosensitizing agent that have strong NIR (~808 nm) absorption, low cytotoxicity, magnetic properties, and excellent stability. Liu et al. [56] show that the $Au-Fe_3O_4-GO$ nanocomposites have superior catalytic capability for hydrazine oxidation and promising for the construction of other electrochemical sensors and

bioanalysis. Li et al. [57] prepare the GO-coated Fe₃O₄ nanocomposite and shown it is an effective and stable candidate for targeted drug delivery.

1.5 Pulsed laser ablation technique (PLA)

A major challenge in nanotechnology is how to fabricate nanostructures with optimized figure-of-merit for different applications and from different materials. Generally, there are two classes of approaches to fabricate nanostructures, namely, bottom-up assembly and top-down fabrication Fig.1.4. Laser ablation of solids is a top-down method, which has attracted much interest ever since the invention of ruby laser in 1960s, because the high-power density near the focus of a pulsed laser ($>10^6$ W/cm²) allows this method to be applied to nearly all classes of materials. However, the generation of micro/nanostructures by bottom-up process may be also formed by nucleation, growth and assembly of clusters from laser ablated species.

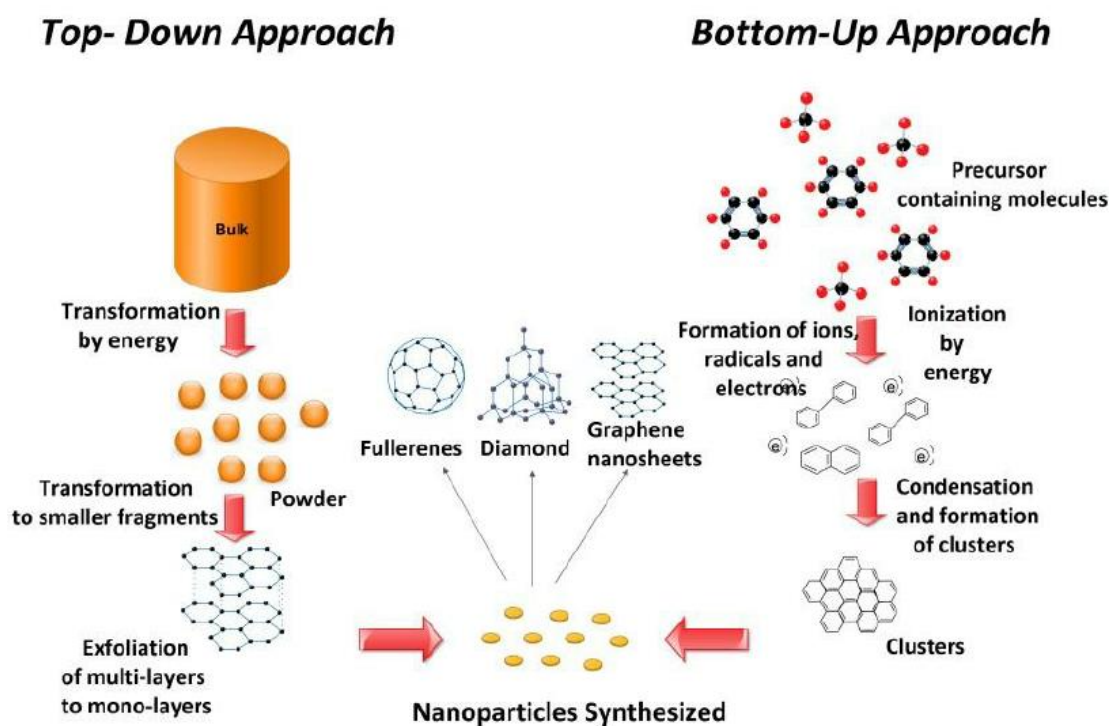


Figure 1.4. bottom-up assembly and top-down fabrication

By definition, laser ablation is the ejection of microscopic amounts of materials from the surface of a solid usually induced by the interaction of short ($\sim 10^{-13}$ to 10^{-8} s), intense ($\sim 10^6$ to 10^{14} W/cm²) laser pulses with the surface (Fig 1.5). The temperature of the irradiated spot

quickly rises when the laser beam is focused on the surface of a solid target material in the surrounding media (gas or liquid), vaporizing the target material. A laser-induced plasma plume is created when evaporating species (atoms and clusters) collide with nearby molecules, excitation of the electron state, light emission, and the creation of electrons and ions. The plasma structures (size and the plume and its emission spectrum) depend on the target material, surrounding media, ambient pressure and laser settings. In principle, this can occur in vacuum, gas, and liquid, providing that the gas or liquid does not strongly attenuate laser energy and the light intensity (fluence) on the solid surface is still enough to perturb the material away from equilibrium state.

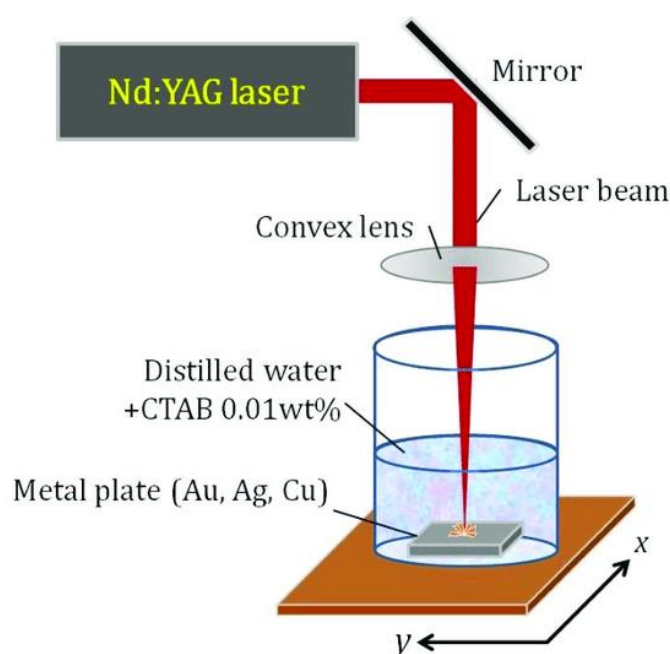


Figure 1.5: laser ablation setup technique

The major application of laser ablation in vacuum or gas is the pulsed laser deposition (PLD) of thin films. While laser ablation in gas has attracted considerable interest since the early 1980s, some researchers started to think about what would happen during laser ablation of solid targets in an even denser and more reactive medium – liquid[14]. Patil et al. are the pioneers to explore the synthesis possibilities at a liquid–solid interface by pulsed laser irradiation of iron in water in 1987. Later, Neddersen et al. reported the synthesis of colloids by laser ablation of metallic targets in water and organic solvents and established this method as a simple yet reliable route to produce clean colloids without residual species. The flourish of pulsed laser ablation in liquid (PLAL) for nanostructure generation started in the early 2000s, promoted by

the synthesis and size control of noble metal nanoparticles (NPs) using laser ablation in aqueous solutions of surfactants[15].

1.6 Photoacoustic spectroscopy

The term photoacoustic effect refers to the generation of acoustic waves by the heat produced through non-radiative de-excitation processes of excited substance created by the absorption of intensity-modulated electromagnetic radiation. In a gas, the thermal energy appears as kinetic energy of the gas molecules, while in a liquid or a solid, the thermal energy is manifested as vibrational energy of ions or atoms. Photoacoustic spectroscopy (PAS) is a technique that measures the PA effect as a form of optical spectroscopy. Using this technique, one can determine sample optical parameters (the optical absorption coefficient β), the thermal parameters (effusivity, diffusivity, and conductivity), or geometrical parameters (sample thickness). In this work, we use PA to measure the thermal parameters of Au@Fe₃O₄/GO.

1.7 Aim of the Work.

This work aims to synthesis a promising material for photonic applications, drug delivery applications and water treatment applications by low cost and single step pulsed laser ablation technique, specially pulsed laser ablation in liquid. First, graphene oxide nanosheets (GO) will be prepared using PLA. Second, magnetite nanoparticles Fe₃O₄ will be added to decorate graphene oxide to form (Fe₃O₄/GO) nanocomposite by the same technique at different ablation time. Finally, different ratios of GO will be added to Au@Fe₃O₄ and sonicated to produce four samples (S1=1:1, S2=1:2, S3=1:3 and S4=1:4) of Au@Fe₃O₄/GO NCs. The structure and average particle sizes of all prepared samples were estimated using high resolution transmission electron microscope (HRTEM). Fourier transform spectroscopy will be used to identify molecular compounds and identify the functional groups present in it. The optical spectra of the samples will be investigated by using UV-visible spectrometers. The optical parameters of the prepared samples will be calculated from the obtained UV-visible spectra. Furthermore, the thermal parameters (diffusivity (α), effusivity (e), and conductivity (k)) will be also obtained.

1.8 Organization of the thesis

This thesis is divided into five chapters. The First Chapter describes nanoparticles chosen and their synthesis techniques. Chapter Two explains in detail a theoretical background approach to characterize the properties of nanoparticles and literature survey. Chapter Three gives the experimental procedures and methodologies adopted in synthesis. Chapter Four describes the experimental results of the studies and its discussions. And conclusions for the current work and future pathway is given in Chapter Five

Chapter2

Literature survey

Literature survey

2. Overview

Laser ablation of a graphite target is an effective method for synthesizing graphene-based nano materials, including graphene oxide (GO), reduced graphene oxide (rGO), and graphene nanoplatelets. Also, laser ablation of graphite is particularly advantageous to produce high-quality graphene materials because it avoids the use of toxic chemicals or solvents, making it an environmentally friendly method. This technique offers precise control over the oxidation/reduction degree, allowing for the tailoring of the material's properties, such as electrical conductivity, surface area, and mechanical strength. Additionally, laser ablation can induce the formation of graphene nanosheets or nanoplatelets, which can further be engineered for a number of applications in various fields, including energy storage, supercapacitors, sensors, and environmental remediation, where high-performance, cost-effective nanomaterials are essential.

2.1 graphene oxide (GO)

2.1.1 History of GO Synthesis

Despite the relative novelty of graphene as a material of broad interest and potential, GO has a history that extends back many decades to some of the earliest studies involving the chemistry of graphite. The first, well-known example came in 1859 when British chemist B. C. Brodie was exploring the structure of graphite by investigating the reactivity of flake graphite [1]. One of the reactions he performed involved adding “potash of chlorate” (potassium chlorate; KClO_3) to a slurry of graphite in fuming nitric acid (HNO_3). Brodie determined that the resulting material was composed of carbon, hydrogen, and oxygen, resulting in an increase in the overall mass of the flake graphite. He isolated crystals of the material, but the interfacial angles of the crystal lattice were unable to be measured via reflective goniometry. Successive oxidative treatments resulted in a further increase in the oxygen content, reaching a limit after four reactions. The C : H : O composition was determined to be 61.04 : 1.85 : 37.11; a net molecular formula of $\text{C}_{2.19}\text{H}_{0.80}\text{O}_{1.00}$. Brodie found the material to be dispersible in pure or basic water, but not in acidic media, which prompted him to term the material “graphic acid.” After heating to a temperature of 220 C, the C : H : O composition of this material changed to 80.13

: 0.58 : 19.29 ($C_{5.51}H_{0.48}O_{1.00}$), coupled with a loss of carbonic acid and “carbonic oxide.” Throughout his studies, Brodie was interested in the molecular formula of “graphite” and its discrete molecular weight. Ultimately, he determined the molecular weight of graphite to be 33, saying: “This form of carbon should be characterized by a name marking it as a distinct element. I propose to term it **Graphon**.” Nearly 150 years later, “graphene” would take the physics and chemistry communities by storm. We now know that Brodie was mistaken in his search for a discrete molecular formula for graphite, and the indeterminate nature of this material shall be discussed more fully in the following sections. Nearly 40 years after Brodie’s seminal discovery of the ability to oxidize graphite, L. Staudenmaier improved Brodie’s $KClO_3$ -fuming HNO_3 preparation by adding the chlorate in multiple aliquots over the course of the reaction (also, with the addition of concentrated sulfuric acid, to increase the acidity of the mixture), rather than in a single addition as Brodie had done. This slight change in the procedure resulted in an overall extent of oxidation similar to Brodie’s multiple oxidation approach ($C : O \sim 2 : 1$), but performed more practically in a single reaction vessel. Nearly 60 years after Staudenmaier, Hummers and Offeman developed an alternate oxidation method by reacting graphite with a mixture of potassium permanganate ($KMnO_4$) and concentrated sulfuric acid (H_2SO_4), again, achieving similar levels of oxidation. Though others have developed slightly modified versions, these three methods comprise the primary routes for forming GO, and little about them has changed.[2]

2.1.2 Structural models of GO

Over the years, the structure of GO was studied in detail using several instrumental techniques: annular dark-field imaging, ultra-high-resolution transmission electron microscopy, X-ray diffraction, and many others. Despite the number of attempts to reveal the structure of GO, several possible structural models exist with no unambiguous one [3]. The main reason for this is the complexity of the material and the originality of every sample with variable stoichiometry. Simplistically, GO is a monolayer sheet of graphite containing hydroxyl, carboxyl, and epoxy oxygen groups on its basal plane and edges, resulting in a mixture of sp^2 and sp^3 hybridized carbon atoms. Many models of GO have been developed based on a number of analyses and theoretical simulations. The first model was suggested by Hofmann and Rudolf in 1939, where a lot of epoxy groups were distributed randomly across the graphite monolayer. Then, in 1946, Ruess updated the model by incorporating hydroxyl groups and alternating sp^2

hybridized carbons with those revealing sp^3 hybridization. In 1969, Scholz and Boem suggested a less organized structure with double bonds C=C and periodically recurring C-C single bonds in the carbon layers that are corrugated with hydroxyls and carbonyls, without ether oxygen. Later, in 1994, Nakajima and Matsuo proposed a model that resembled graphite intercalation compound. Then, in 1998, Lerf and Klinowski created a model (LK model) that contains two different kinds of regions: regions with six-membered aliphatic rings and regions with no oxidized benzene aromatic rings. The size of the two regions is dependent on the level of material oxidation. The model is composed mainly of aromatic bodies, epoxide groups, and double bonds. Wrinkling in the monolayer is caused by the slightly distorted tetrahedral configuration of hydroxyl groups attached to carbon atoms. The oxygen functional groups are attached to the monolayer of carbon above and below, creating two layers of oxygen atoms with variable concentrations composed mainly of epoxide and hydroxyl groups that are very close to each other. All the oxygen functionalities, aromatic bodies, and oxidized rings are distributed randomly across the carbon monolayer. The acidity of GO can be explained by the oxygen groups that are attached to the edges of the lattice, which are hydroxyl and carboxyl groups. This LK model has become one of the most acceptable and used models for moderately oxidized GO (Fig.2-1).[4] After the discovery of graphene, researchers worldwide started to focus on GO and other derivatives. In 2006, Szábó and Dékány examined previous models by several analyses and suggested a model without carboxylic acids composed of two main regions: corrugated hexane ribbons occupied with quinones and ketones, and translinked cyclohexane chairs with 1,3-epoxide and tertiary alcohols. In 2013, Dimiev, Alemany, and Tour proposed a dynamical structural model (DSM) that describes the development of various carbon structures with attached water, contrary to the static LK model. Recently, Liu et al. experimentally observed the evidence of the C=O bonds on the edge of the carbon monolayer, confirming parts of the earlier models, especially the LK model. Real GO also includes some defects, such as topological defects (pentagons, heptagons, octagons, etc.), adatoms, vacancies, and adsorbed impurities.[4]

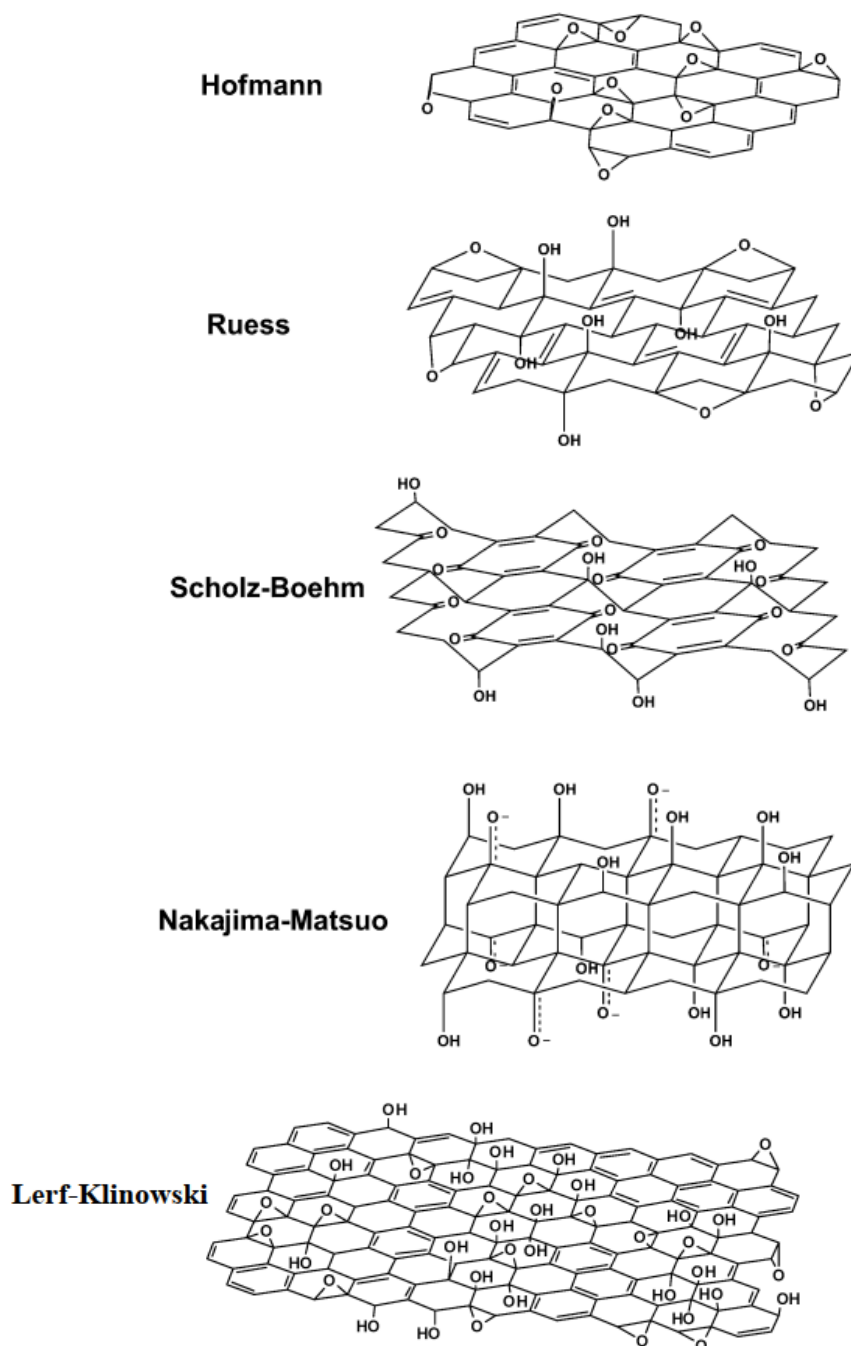


Figure 2.1: Summary of several older structural models of GO.

2.1.3 Modern Ways of GO Synthesis

There are several ways to prepare graphite oxide/graphene oxide. The most common way is to use an oxidizing agent in an acidic environment. Other methods are electrochemical, microbial

and physical[5]. Let us note that GO prepared by chemical routes often displays a highly damaged structure due to the harsh acidic conditions of the synthesis as well as the presence of impurities. Such characteristics are indeed far from being optimal for electronics applications. Apart from the chemical routes, electrochemical synthesis represents another approach to GO synthesis that might be the key to large-scale production [6]. Electrochemical production is more eco-friendly than chemical production due to reusing the electrolyte multiple times and minimal washing of the utensils. The better quality of electrochemical GO (EGO), in contrast to standard procedures, can be explained using aqueous electrolytes and no need for oxidizing agents, hence avoiding impurities. Moreover, thanks to the variety of experimental setups, the level of oxidation and density of defects can be controlled [7]. Interestingly, the usage of biological systems to oxidize graphitic materials is very important to obtain eco-friendly graphene oxide. However, after the microbial cultivation, graphite is not homogeneously oxidized. *Acidithiobacillus ferrooxidans* or *Pseudomonas* have been tested as oxidizing bacteria [8]. recently, Laser-based approaches for graphene oxide synthesis, reduction, modification, cutting and micro-patterning have been developed and applied to the fabrication of various electronic devices. These laser-based techniques exhibit several advantages over alternative methods: low temperature, shorter reaction times, environmentally friendly, energy saving, catalyst free growth on insulating substrates, high productivity, better reproducibility, scalability, excellent control over experimental parameters [9].

2.1.4 Applications of graphene oxide

- Nanographene oxide (NGO) prepared by laser ablation technique showed an excellent results in bioimaging applications, specially, when synthesized under the organic solvent like ethanol, acetone and isopropyl alcohol; where it possesses exceptionally high fluorescent properties. In Polyethylene glycol (PEG) which is an eco-friendly solvent, it exhibits excellent fluorescent characteristics and shows a successful demonstration of in-vitro cytotoxicity analysis on the MCF-7 cancer cell and A549 lung cancer cell lines[16].
- GO has been employed in water filtration and desalination due to its porous structure and ability to remove contaminants, such as heavy metals due to its selective permeability, organic compounds, and bacteria[17].

- GO is used in drug delivery systems due to its biocompatibility and ability to easily functionalize. It also serves as a platform for photothermal therapy and imaging due to its strong absorption in the near-infrared region[18].
- GO is used in the development of chemical and biosensors due to its ability to interact with various analytes. It enhances the sensitivity of sensors by acting as a transducer or electrode material[19].

2.2 Magnetite (Fe₃O₄)

Utilization of magnets as navigational devices extends back to 8th century in China; however, natural magnets, nicknamed loadstones, have been employed as fortune-telling devices since 200 B.C. Natural organisms, known as magnetotactic bacteria, have been using nanoscale (30-100 nm) magnetic particles since ancient times to orient and migrate along geomagnetic fields towards favourable habitats. Magnetic particles utilized by Chinese sailors and magnetotactic organisms are chemically composed of Fe₃O₄, or magnetite; “magnetite,” derives from the district of Magnesia in Asia Minor, where large deposits of magnetite were discovered. Containing both ferrous (reduced) and ferric (oxidized) iron species, magnetite is oftentimes described as iron^{II,III} oxide [10]. Due to its typical magnetic and electrical properties, magnetite is one of the preferred and widely used in numerous industrial processes (e.g., printing ink), environmental applications (e.g., magnetite carrier precipitation processes for metal ion removal and magnetic filtration), and also medical applications (biomolecule separation and contrast agents for NMR imaging), some of which are exciting and are under development at the moment (drug targeting and hyperthermia) [11]. The synthesis of magnetite nanoparticles can be performed by several methods, such as the polyol process, precipitation route, sonochemical synthesis and laser ablation. The micro spinel structure is shown in Fig.2-2.

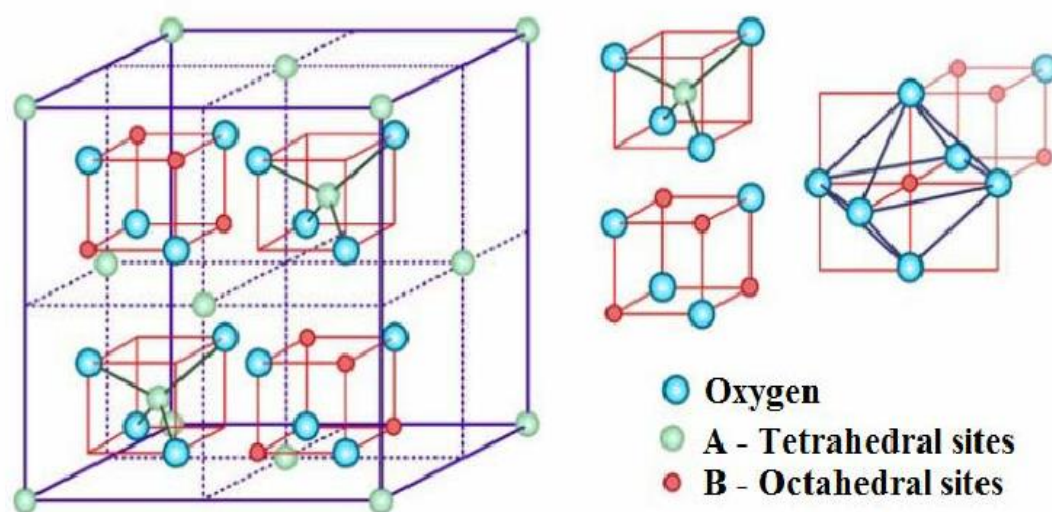


Figure 2.2: Micro spinel structure of Fe₃O₄

Here, oxygen anions form a face-centered cubic (FCC) closed packing and Fe cations occupy the interstitial tetrahedral sites and octahedral sites. The electrons can hop between Fe⁺² and Fe⁺³ ions in the octahedral sites at room temperature, rendering magnetite an important part of half-metallic materials. It has a lattice constant of $a=0.8396$ [12]. Magnetite is ferrimagnetic at room temperature and has a Curie temperature (T_C) of 850 K (the temperature above which a ferromagnetic material loses its ferromagnetic properties and becomes paramagnetic). It has a rather high Curie temperature when compared to other phases of iron oxide. It is a mixed-valence compound. Ferric ions fully occupy the tetrahedral (A) sublattices. Half of the octahedral (B) sublattices are occupied by Fe⁺² ions and the other half are occupied by Fe⁺³ ions. Below T_C , A-site magnetic moments are aligned antiparallel to the B-site magnetic moments. The net effect is that the magnetic contributions of both sites are not balanced and there is a permanent magnetism [13]. So with such great properties Fe₃O₄ was chosen to decorate GO sheets.

2.2.1 Applications of Fe₃O₄/GO NCs

- Fe₃O₄/GO nanocomposites are used in water purification, specifically for removing heavy metals, dyes, and organic pollutants. The magnetic properties of Fe₃O₄ allow for easy recovery and reuse, while GO's large surface area provides an excellent platform for adsorption [20].

- $\text{Fe}_3\text{O}_4/\text{GO}$ nanocomposites are explored for controlled drug delivery systems. The Fe_3O_4 nanoparticles offer magnetically responsive behavior, allowing for targeted drug release at specific locations by applying an external magnetic field, while GO serves as a carrier for drugs due to its high surface area[21].
- $\text{Fe}_3\text{O}_4/\text{GO}$ nanocomposites are used as contrast agents for magnetic resonance imaging (MRI). The iron oxide nanoparticles provide strong magnetic properties, which can enhance the contrast and resolution of MRI scans see Fig.2-3, while GO can help dispersing and stabilizing the nanoparticles in solution[22].

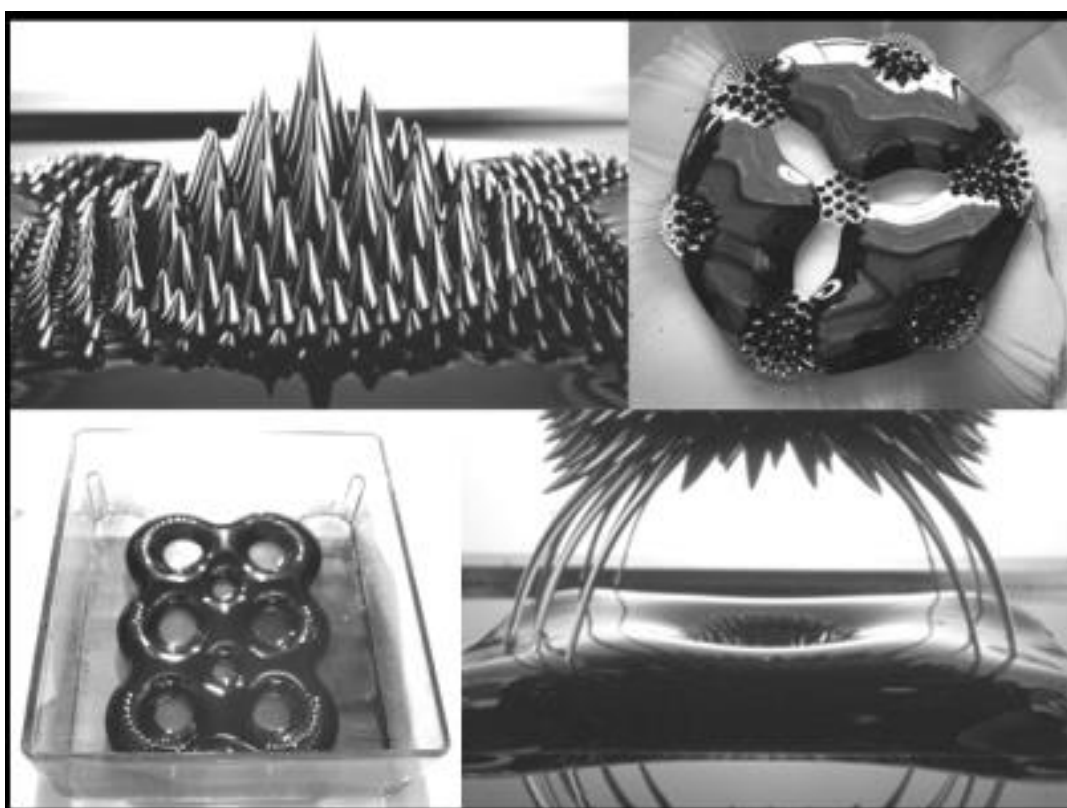


Figure 2.3: Ferrofluids under external magnetic field

2.3 Gold nanoparticles

The original application of gold nanoparticles (AuNPs) in the biomedical field can be traced back to the Middle Ages, the so-called potable gold, known in old Latin texts as *Aurum potable*. Potable gold behaved as a fabulous curative power for various diseases, such as heart and venereal problems, arthritis, epilepsy and tumours, as well as for diagnosis of syphilis. Among the physical properties of AuNPs localized surface plasmon resonance (LSPR),

radioactivity and high X-ray absorption coefficient which are widely used in the diagnosis and treatment of tumours. The LSPR of AuNPs can further lead to surface-enhanced Raman spectroscopy (SERS), surface enhanced fluorescence (SEF), photothermal conversion, photochemical conversion and colorimetric responses. These excellent qualities have been widely applied for non-invasive detection in vivo and in situ, imaging, photothermal therapy (PTT), photodynamic therapy (PDT) and in vitro diagnostics (IVD). The radioactivity of AuNPs can be used for radiotherapy and radionuclide imaging (RNI). The high atomic number of AuNPs has been explored for radiotherapy sensitization. When the atomic number is higher than 53, the absorbed dose of the X-ray will increase. Au has an atomic number of 79, which strongly increases the X-ray absorption coefficient. This can minimize the damage of X-ray to normal tissues and becomes a promising radiotherapy sensitizer for oncotherapy[16]. Owing to their attractive electronic, optical, magnetic, and thermal properties as well as catalytic properties, Au nanomaterials have received a wide variety of applications in the fields of physics, chemistry, catalysis, technology, biomedicine, material science and electrochemical sensors. More interestingly, the intrinsic properties of Au nanomaterials can be controlled by tuning their shape, size, and the surrounding chemical environment. Also, gold nanoparticles (AuNPs) with different shapes, such as spheres, rods, triangles, cubes and nanowires have been prepared by various synthetic techniques[17].

2.4 Gold–Magnetite nanocomposites

Gold-magnetite nanocomposites are hybrid materials that combine gold nanoparticles (AuNPs) with magnetite nanoparticles (Fe_3O_4), creating a composite with unique properties derived from both components. These nanocomposites have garnered significant interest due to their multifunctional characteristics, which combine the biological and catalytic properties of gold with the magnetic properties of magnetite. **Magnetic Properties:** Magnetite nanoparticles impart superparamagnetic properties to the composite, allowing for easy separation using an external magnetic field. This is useful in applications where separation and recovery are essential. In some specific applications, the combination of gold and magnetite nanoparticles could be used to tune the properties (e.g., for biomedical applications like targeted drug delivery), but the magnetism itself would generally decrease due to the non-magnetic nature of gold. **Optical Properties:** Gold nanoparticles provide unique optical properties, including surface plasmon resonance (SPR), which can be tuned by altering the size and shape of the

gold particles. This can be used in imaging, sensing, and diagnostic applications. **Catalytic Properties:** Gold is a well-known catalyst for various reactions, and the combination of gold with magnetite enhances its catalytic activity, particularly in oxidation and reduction reactions. **Biocompatibility:** Both gold and magnetite are generally considered biocompatible, which makes these nanocomposites useful for biomedical applications such as drug delivery, imaging, and biosensing[22]. Therefore, in the present work such a composite has been chosen to decorate GO nanosheets.

2.4.1 Applications of Au@Fe₃O₄/GO nanocomposites

- Au@Fe₃O₄/GO nanocomposites can be used in immunosensors or DNA biosensors for detecting pathogens or specific DNA sequences, with gold nanoparticles enhancing the signal and magnetite allowing for magnetic separation and easy recovery of the sensor.
- Au@Fe₃O₄/GO nanocomposites are utilized for targeted drug delivery, especially in cancer therapy. Gold nanoparticles can be used to load drugs, and the magnetic Fe₃O₄ component allows for external magnetic control of the drug delivery process, enhancing targeting to specific areas. The GO platform provides high surface area for functionalization, allowing for the attachment of ligands, antibodies, or other targeting molecules.
- The magnetic properties of Fe₃O₄ allow Au@Fe₃O₄/GO nanocomposites to be used for the separation of specific substances from complex mixtures. This is particularly useful in environmental cleanup, such as removing heavy metals, dyes, and other pollutants from water. The high surface area of GO provides adsorption sites for contaminants, and the gold nanoparticles may also help in catalytic degradation[23].
- The combination of gold nanoparticles (with their excellent conductivity) and graphene oxide (which has good electrochemical properties) makes Au/Fe₃O₄/GO nanocomposites useful for electrochemical sensors. These nanocomposites can be employed in detecting a variety of substances, including heavy metals, pH changes, and biological markers[24].

2.5 Laser ablation

The study of the interaction of high-power lasers with solid matter is as old as the laser itself. Various, it was termed laser ablation, vaporization, sputtering, desorption, spallation or etching. The physical processes involved are extremely complex. Electromagnetic energy is converted to electronic, thermal, chemical and mechanical energy at the solid surface. The ejected material may include neutral atoms and molecules, positive and negative ions, clusters, electrons and photons. The generated plasmas may have electron temperatures of thousands of degrees. The first archived accounts of laser ablation experiments appeared as abstracts of conference presentations. The very first such account known is a presentation entitled "Optical Micro mission Stimulated by a Ruby Maser" presented by Breech and Cross at the International Conference on Spectroscopy held at the University of Maryland in June 1962. A focused ruby laser was used to vaporize and excite atoms from solid surfaces. The photon spectrum was dispersed and used to characterize the elements composing the surface. This paper had begun the field of laser microprobe emission spectroscopy which was the first real application area of laser ablation. Early application of the laser microprobe involved the elemental analysis of geological, biological or metallic samples[24]. In principle, this can occur in vacuum, gas, and liquid, providing that the gas or liquid does not strongly attenuate laser energy and the light intensity (fluence) on the solid surface is still enough to perturb the material away from equilibrium state. The temperature of the irradiated spot quickly rises when the laser beam is focused on the surface of a solid target material in the surrounding media (gas or liquid), vaporizing the target material. A laser-induced plasma plume is created when evaporating species (atoms and clusters) collide with nearby molecules, excitation of the electron state, light emission, and the creation of electrons and ions[25]. It is possible that the plasma cloud absorbs some of the incident laser energy and thereby only allows a fraction of the laser energy to reach the surface (plasma shielding). The plasma expands and is heated by photon absorption. Later the vapour cools and aerosol particles begin to form. The rest of the energy diffuses into the material via heat transfer. The major application of laser ablation in vacuum or gas is the pulsed laser deposition (PLD) of thin films . An important part of PLD's success came from the ability to deposit vapours in high pressures of reactive gases. Laser ablation in non-vacuum environments has benefits due to the reactions in a dense, but temporally short-lived environment. It must be realized that bimolecular (biparticle) bonding in the gas phase requires a third body to conserve both momentum and energy. As such, the

dense ablation plume near the target is a wealth of interesting particle bonding reactions. While laser ablation in gas has attracted considerable interest since the early 1980s, some researchers started to think about what would happen during laser ablation of solid targets in an even denser and more reactive medium – liquid. Patil et al. are the pioneers to explore the synthesis possibilities at a liquid–solid interface by pulsed laser irradiation of iron in water in 1987. Later, Neddersen et al. reported the synthesis of colloids by laser ablation of metallic targets in water and organic solvents and established this method as a simple yet reliable route to produce clean colloids without residual species. The flourish of pulsed laser ablation in liquid (PLAL) for nanostructure generation started in the early 2000s, promoted by the synthesis and size control of noble metal nanoparticles (NPs) using laser ablation in aqueous solutions of surfactants.

the schematic diagram of a typical experimental setup for PLA is shown in Fig.2.4. The setup basically only needs a pulsed laser, beam delivery optics, and a container to hold the target and certain surrounding medium. The container as well as the target is usually rotating to avoid a deep ablation crater. Alternatively, the laser beam can be delivered by scanner optics to move the ablation spot. The setup may be modified to control the ablation process, but the common features still exist, that is, a laser beam is focused onto a target in a chosen medium[26].

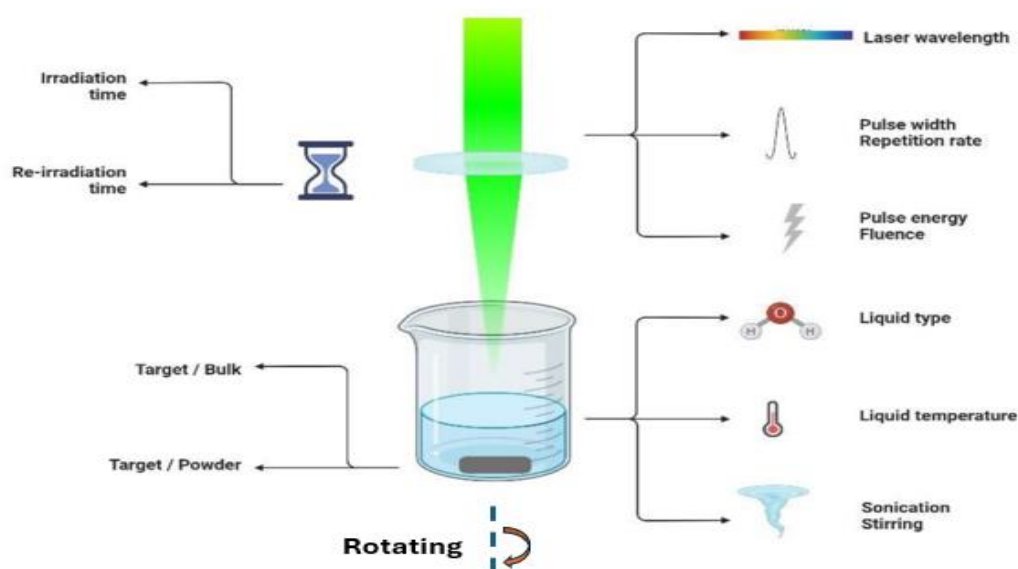


Figure 2.4: The schematic diagram of a typical experimental setup for PLAL

-
- **Laser wavelength:** With very few exceptions, once a type of laser is chosen, the frequency of light emission is fixed. The wavelength (or frequency) of the radiation is one of the most important factors, since it determines the percentage of light reflected, absorbed or transmitted by the material, the depth of beam penetration in the sample and the type of interaction with the solid lattice (both crystalline and amorphous). As a general rule, infrared lasers are a good choice for applying localized heating to a region of the sample surface (photothermal effect). For most materials the penetration depth is in the range between a few microns and hundreds of microns, depending on the wavelength. The dissipation of heat in the sample, dependent on thermal conductivity and the immediate environment, can affect the material adjacent to the illuminated region, giving rise to the so-called “heat affected zone”. For lasers operating in the ultraviolet range, depth of penetration is much smaller (of the order of tens or hundreds of nanometres). Since the beam energy is concentrated in a smaller volume of material, ultraviolet lasers are well suited to perform operations relying on material ablation (cutting, drilling, surface layer removal). Furthermore, the energetic high frequency radiation can break chemical bonds (photochemical effect), opening the possibility to initiate chemical reactions, ionization, or desorption of surface molecules when the operation is performed at lower laser powers[25].
 - **Laser power:** Laser power is directly related to the amount of energy transferred to the material as a function of time. Although the effects of laser power are easily understood at a basic, intuitive level, a great deal of misunderstanding takes place when researchers fail to take into account that laser power (as defined) is time-averaged, giving no indication of instantaneous energy transfer. For example: two pulsed lasers with the same power emitting light at the same wavelength can have completely different effects upon the material if they operate at different combinations of pulse width and frequency. Most commercial pulsed lasers operate at constant pulse energy within a wide frequency range. The power values are just a consequence of different pulse frequencies. Fig. 2.5 shows experimental results of laser power as a function of pulse frequency for a commercial diode-pumped solid state (DPSS) laser operating at the 355 nm wavelength. One should notice that the slope of the curve corresponds to the value of pulse energy. In this case, the pulse energy is reasonably constant ($\sim 200\mu\text{J}$) up to around 90 kHz.

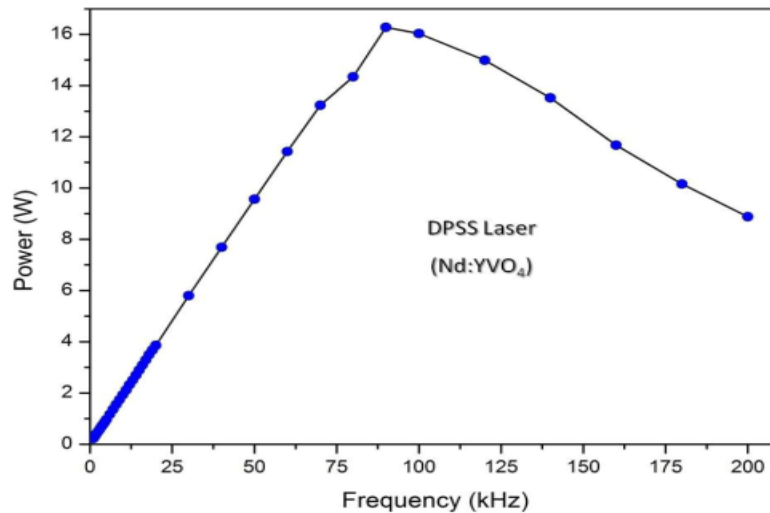


Figure 2.5: Laser power as a function of pulse frequency for a commercial DPSS laser.

- Pulse width:** The amount of time during which the interaction between the laser beam and the material takes place is a key factor that might determine the outcome of a laser treatment, since different phenomena can occur in the material as the time scale for interaction is varied. For a given laser model, pulse width (or duration) is usually constant across the recommended operating range, being determined by the design and arrangement of its internal components. Commercial equipment is available with pulse widths varying in a scale that goes from milliseconds down to femtoseconds. Continuously emitting lasers can be considered a special case, where the active laser medium is uninterruptedly pumped and the radiation is allowed to exit the laser cavity unimpeded, making the “pulse width” essentially infinite. The importance of pulse width can be easily illustrated by considering once again the example mentioned in the preceding section. The graph in Fig. 2.5 shows average power, but for each laser pulse lasting 20 ns (nominal pulse width), the instantaneous power is 5 kW. In other words, the laser pulses are only emitted for a small fraction of the time (low duty cycle), concentrating high levels of energy output. This effect is even more pronounced for lasers operating at the Pico and femtosecond regimes[9]. Here is a comparison between nano and femtosecond lasers

Nanosecond Lasers: Due to the relatively longer pulse duration, energy is spread over a larger period, allowing for thermal effects such as melting, evaporation, and thermal diffusion. The laser energy doesn't vaporize the material, laser heats it, raises their temperature and propagates via heat conduction inside the material. The temperature distribution is governed by the heat conduction equation:

$$\rho C_p \frac{\partial T}{\partial t} = \nabla \cdot (K \nabla T) + (1 - R) I_0 \alpha e^{-\alpha z} \quad (2-1)$$

Where ρ , C_p , K , T : represent density, specific heat, thermal conductivity and temperature, respectively. The second term on the right hand side of equation 2-1 represents the source term which is the laser energy absorbed by the material at a depth z from the surface, where R is the surface reflectivity, and I_0 is the laser irradiance and α is the absorption coefficient (the imaginary part of the complex refractive index, assumed to be constant). This results in: Thermal damage: The material can experience unintended heat-related effects such as the formation of heat-affected zones (HAZ), melting, or even cracks due to thermal stresses. Laser-induced breakdown: For certain materials, the longer pulse duration can create sufficient energy to overcome the material's thermal conductivity limit, causing a plasma or spark formation. For example, laser engraving or laser marking with a nanosecond laser can cause localized heating that leads to discoloration or even surface ablation.

Femtosecond Lasers: Femtosecond pulses are so short that the material absorbs the energy before it has time to heat up. This results in cold ablation, a highly localized, non-thermal material removal process. The extreme shortness of the pulse minimizes heat transfer, and laser-induced breakdown (or plasma formation) happens very close to the surface, often without causing any significant thermal damage to the material. The material is often ablated without melting or significant heat diffusion. Multiphoton absorption: Femtosecond pulses can excite the material in such a way that multiple photons are absorbed simultaneously (this is particularly important for processes like multiphoton polymerization or creating nanostructures). As a result, femtosecond lasers can be used for applications requiring extreme precision, such as micro-machining, microsurgery, and nano-patterning[27]. See Fig. 2.6

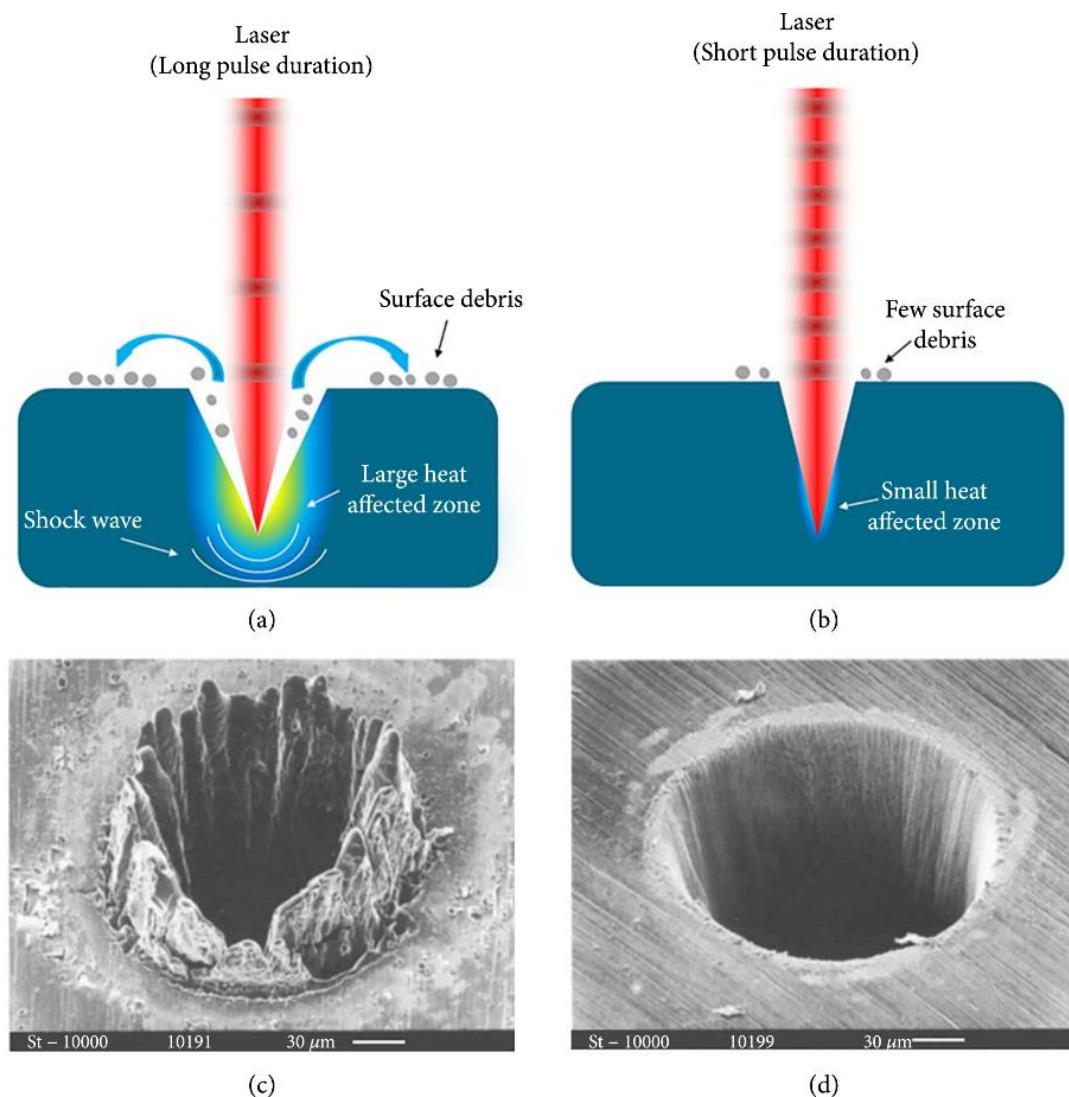


Figure 2.6 : a) Effect of nanosecond laser, b) Effect of femtosecond laser, and their SEM images at c) and d) respectively.

- Fluence:** Laser fluence is perhaps the best quantity for quantifying the laser-matter interaction, because fluence is defined as the energy density at the illuminated surface region of the sample (laser energy per surface area). One should notice that laser fluence may be varied either by changing the pulse energy or by changing the beam spot size. It is normally easier to change fluence by varying the degree of beam focusing, considering the constraints imposed by the specific job being performed. Since most commercial lasers have emission with constant pulse energy, the only way to change the incident energy is by using additional components to optically attenuate the laser beam. Depending on

the laser type and the nature of the job being performed, beam attenuation can be achieved, for example, by using beam-splitters, combinations of polarizers and wave-plates, pinholes, or partially absorbing optical filters.

- **Beam energy profile:** The energy of a laser beam is not usually constant throughout its cross-section. Most lasers used for materials processing have a circular cross-section and a Gaussian beam energy profile (excimer lasers are key exceptions). This energy distribution, illustrated in Fig. 2.7, has important consequences for laser treatments; the most obvious one is that the laser fluence, as discussed in the preceding section, is actually an average. The central region of the laser spot illuminating the surface has a much higher intensity than the edge. One can think in terms of “local fluence” to see the effect of a non-uniform energy profile regarding laser-material interactions. Excimer lasers exhibit rectangular beam cross-sections and an almost constant beam energy profile, usually called “top hat” profile because of the shape resemblance. This energy distribution is more convenient for laser treatments due to the uniformity in laser fluence.

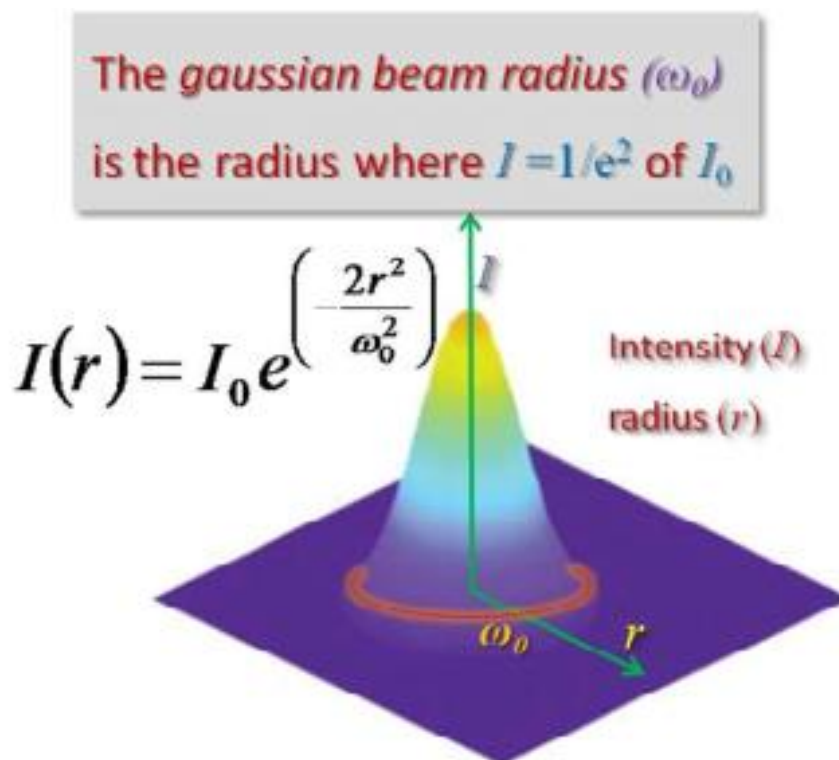


figure 2.7: Gaussian beam profile and the expression for calculating the beam intensity as a function of radial position.

- **Beam focusing:** Although several combinations of lenses could be used, focusing the laser beam using a single converging lens is the most simple and convenient means of increasing the energy density at the material surface. Furthermore, many laser operations are performed with the intent to build micron-scale features in the sample in order to obtain miniaturized devices, thus demanding beam focusing, even in the cases where the increased fluence is not needed. The maximum achievable degree of beam focusing is limited by the wavelength of laser emission and the focal length of the lens. For a laser beam with a Gaussian energy profile (the most common type), the diameter of the focused beam waist and the depth of focus are illustrated in Fig.2.8.

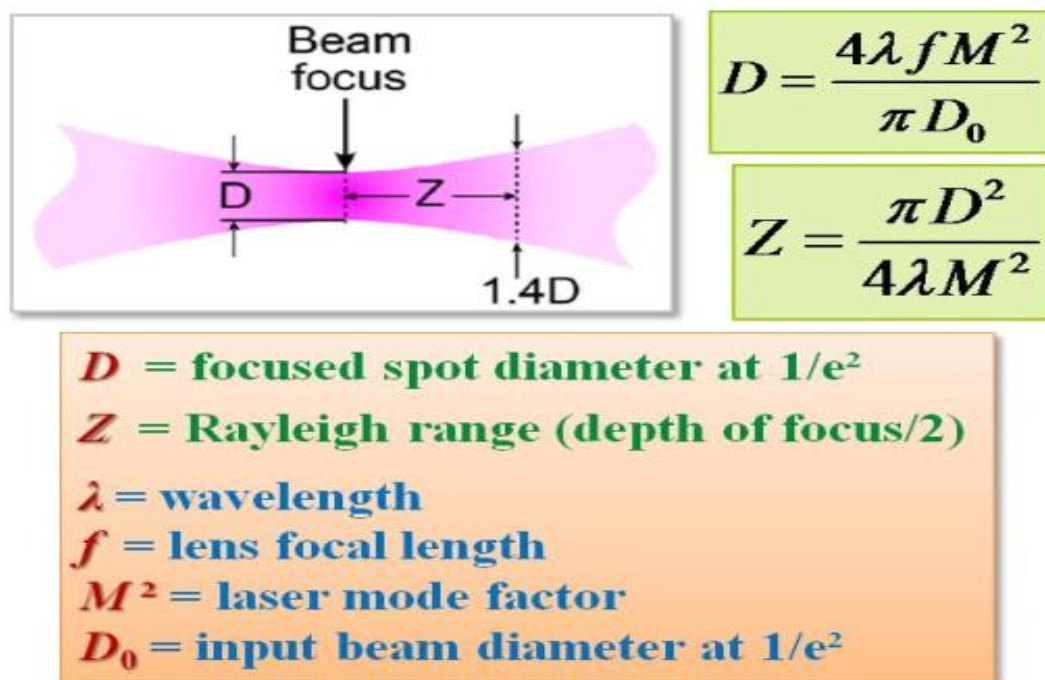


Figure 2.8: The focal region of a laser beam and the expressions for calculating the minimum spot diameter and the depth of focus.

It is useful to notice that once a laser is chosen, the only way to change the focused spot size is to select a lens with a particular focal length. The depth of focus is arbitrarily defined as the distance between two points where the beam diameter is $2^{1/2}$ times the minimum diameter. This parameter is related to

the minimum spot size and gives an indication of how quickly the spot size increases as the laser beam is defocused[26].

- **Writing speed:** The preceding discussion about fluence can be extended to include the relative movement between laser beam and sample surface, necessary for most treatment operations. The total interaction time between the laser beam and the material is determined not only by pulse duration and frequency, but also by spot size and by the speed used for sweeping the beam on the sample surface (normally called “writing” speed). Many different setups for laser treatment systems are possible, including translation stages, galvanometer scanners or a combination of both, but for the purposes of this discussion, these details are irrelevant. Whether the beam or the samples are kept static, it is the relative movement that determines the total energy imparted to a given point on the surface. This is analogous to the concept of “radiation dose” used in the nuclear industry. For continuous lasers, the length of time during which a particular point on the surface will be illuminated is only dependent on spot size and scanning speed. For pulsed lasers it is common to find in the literature the expression “spot overlap”, meaning the percentage of a laser spot area that is covered by the next pulse. Alternatively, spot overlap can be expressed as the number of times a region of the material having the dimensions of the laser spot is illuminated by the laser pulses. This definition gives a more intuitive idea of “laser dose”[27][28]. Fig.2.9 illustrates the effects of the relevant variables on spot overlap for a pulsed laser.

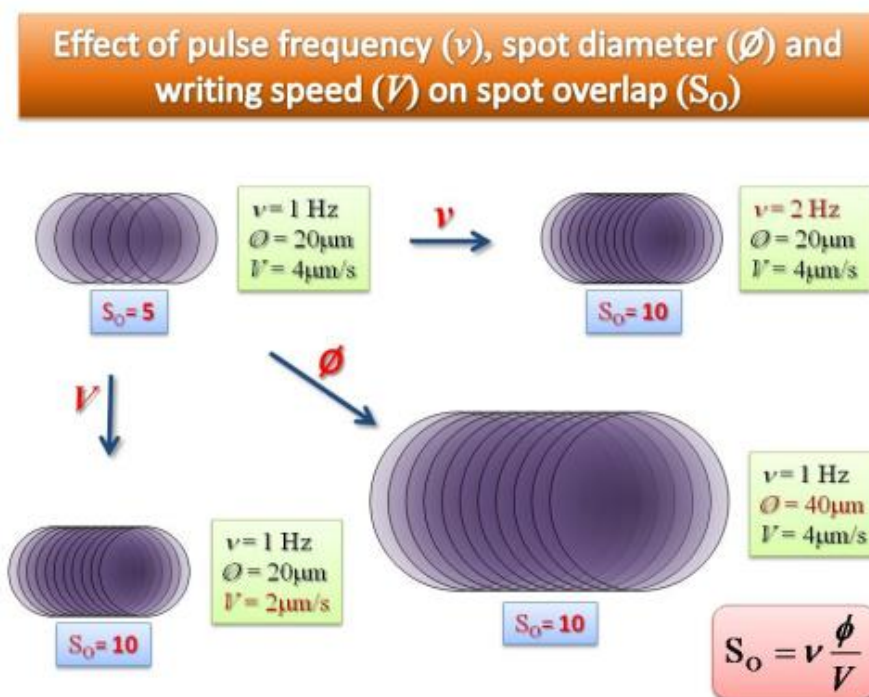


Figure 2.9: Changes in spot overlap as the effect of different values of spot diameter, pulse frequency and writing speed.

The circular shape of the laser spot, by itself, introduces another degree of inhomogeneity in the amount of energy transferred to the written track on the material surface. One should notice in Fig.2.9 that only the central part of the spot fits the definition of spot overlap. The laser dose across a direction perpendicular to the written track, represented as the number of times a region of the material is illuminated by the laser pulses shown in Fig.2.10

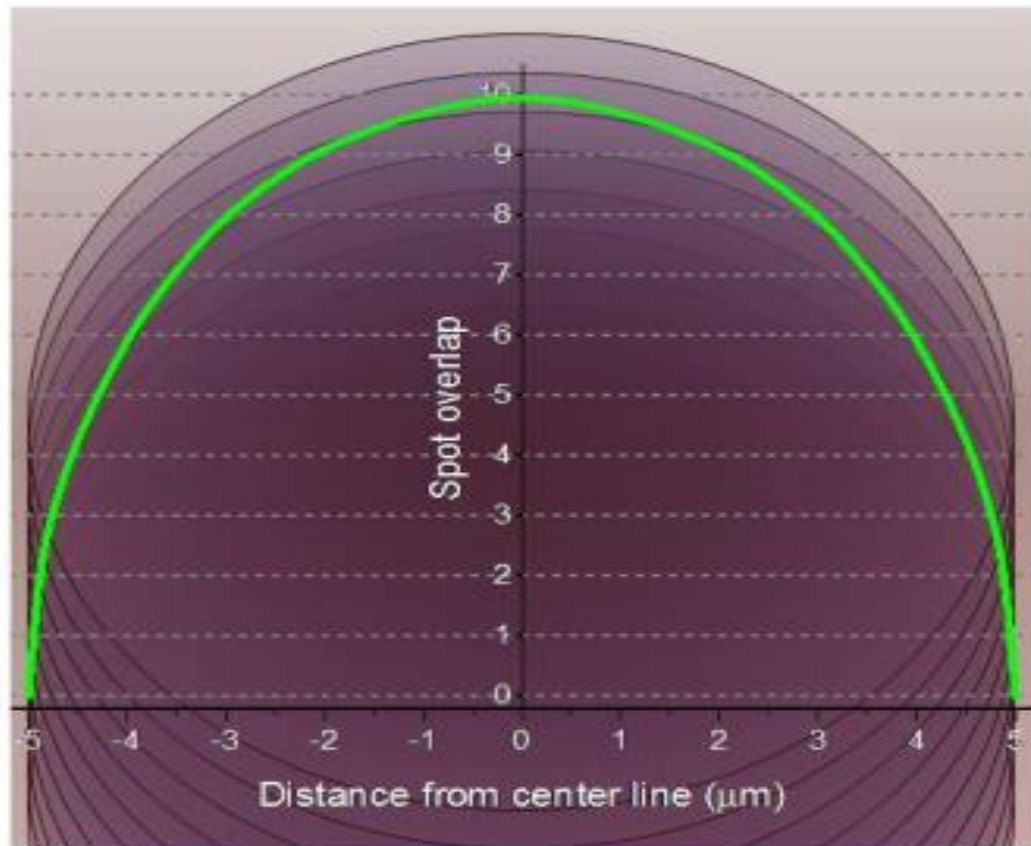


Figure 2.10: Spot overlap as a function of distance from the center line of a track written with a circular laser spot.

- **Local environment:** Most of laser treatments are probably executed with the sample in air, under ambient conditions of temperature and pressure. But the effect of the surrounding environment on the outcome of laser exposure can be decisive, giving rise to new effects and, consequently, to novel properties for the treated area. Laser treatments can be performed with the sample under reduced pressure, controlled atmosphere, controlled temperature, immersed in a liquid and even buried under a

solid film, depending on the objective of the operation. By controlling the immediate environment, one can promote (or inhibit) chemical reactions, diffusion, melting, ablation, etc.

2.5.1 Laser ablation in liquid medium

Laser ablation carried out in a liquid medium is a simple technique that allows the fabrication of several nanomaterials and due to its versatility, low cost and ease of execution has attracted considerable interest. The important difference between laser ablation of solids in a gas ambient and in liquids is that liquids provide a much stronger confinement, restricting the expansion of the plasma plume. The liquid also brings an environment which affects cooling, condensation and phase formation in a way that is different from that of laser ablation in a diluted gas atmosphere or in vacuum[29]. Within the common experimental setup of PLAL, the laser beam has to penetrate a liquid layer before reaching the solid surface. Two phenomena could happen during the process. First, the focal length of the focusing lens will change due to refraction or even self-focusing, typically for picoseconds (ps) and femtosecond (fs) lasers with high intensity, by the liquid layer. Considering the refraction of a focused linear beam, the focal length will increase by

$$\Delta f = l \left(1 - \frac{f}{\sqrt{n^2 f^2 + (n^2 - 1)r^2}} \right) \quad (2-2)$$

where f is the focal length of the focusing lens in air, l is the liquid thickness, n is the refractive index of the liquid, and r is the radius of unfocused laser beam. For $r \ll f$, the formula can be simplified to

$$\Delta f = l \left(1 - \frac{1}{n} \right) \quad (2-3)$$

This is the length that the lens should be moved away from the solid surface to achieve optimum focusing. Strictly speaking, refraction of a laser beam that generally has a Gaussian profile is more complex; nevertheless, Menendez-Manjon et al[15]. have applied the ABCD-transfer-matrix method to this problem and got the same result as Eq. (2-3). They have further analysed other effects that will also affect the focusing, such as the vaporization of the liquid at the liquid–air interface and the self-focusing phenomenon. Second, the laser beam will be attenuated when it passes through the liquid. The attenuation is due to absorption of photons and to their scattering by liquid molecules. This can be caused by other matter in the liquid as well, such as surfactant molecules, ions, and particles produced by previous laser pulses[30]. The light intensity decreases exponentially by

$$I_v = I_{v_0} e^{-\int_0^x \mu_v dx} \quad (2-4)$$

for a path length of x , where ν is the attenuation coefficient composed of the absorption coefficient and the scattering coefficient at the light frequency ν . In systems where absorption dominates, the attenuation can be expressed as the Lambert–Beer law

$$I_{\nu} = I_{\nu_0} e^{-\alpha x} \quad (2-5)$$

Generally, the liquid in PLAL is assumed to be transparent, namely, δ ($\delta = \frac{1}{\alpha}$) is infinite. However, multiphoton absorption by liquid molecules may occur even at relatively low fluence, and this in turn, may cause photothermal heating and/or photodissociation of the liquid especially by lasers of short wavelengths (e.g., UV lasers). These effects could be enhanced by the overlapping of the reflected and incident laser beam. Attenuation by laser-produced particles will be more significant upon the increasing of ablation time which results in higher particle concentration, and especially for metallic nanoparticles, when the laser wavelength is in the excitation range of surface plasmon resonance of the nanoparticles[31]. Absorption of photo energies by laser-produced particles may cause secondary laser processing of the particles, such as heating/melting, welding/sintering, and fragmentation, and could be applied to fabricate unique nanostructures[32].

2.6 photoacoustic effect

Photoacoustic spectroscopy (PAS), is a photothermal detection technique[33]. PAS is distinguished from the conventional techniques chiefly by the fact that, even though the incident energy is in the form of optical photons, the interaction of these photons with the sample under investigation is studied not through subsequent detection and analysis of some of these photons but rather through a direct measure of the energy absorbed by the material because of its interaction with the photon beam. Although more is said about experimental methodology later in chapter 3, a brief description here might be appropriate. In photoacoustic spectroscopy, or PAS, the sample to be studied is placed in a closed cell or chamber. In the case of gases and liquids the sample generally fills the entire chamber. For solids, the sample fills only a portion of the chamber, with the rest of the chamber filled with a non-adsorbing gas such as air. In addition to the sample, the chamber also contains a sensitive microphone. The sample is illuminated with monochromatic light that either passes through an electromechanical chopper or is intensity-modulated in some other fashion. If any of the incident photons are absorbed by the sample, internal energy levels within the sample are excited. Upon subsequent deexcitation of these energy levels, all or part of the absorbed photon energy is then transformed into heat energy through nonradiative deexcitation processes. In a gas this heat energy appears as kinetic energy of the

gas molecules, whereas in a solid or liquid it appears as vibrational energy of ions or atoms. Since the incident radiation is intensity-modulated, the internal heating of the sample is periodic. The periodic heating of a solid or liquid sample from the absorption of the optical radiation results in a periodic heat flow from the sample to the non-absorbing gas[34]. This in turn produces pressure and volume changes in the gas, which are detected by the condenser microphone. This method is quite sensitive, especially for samples with large surface : volume ratios such as powders, and it is capable of detecting temperature rises of 10^{-6} to 10^{-5} C in the sample, or thermal power generation of about 10^{-6} calories / $\text{cm}^3 \cdot \text{sec}$. There are several advantages of photoacoustic spectroscopy. Since absorption of optical or electromagnetic radiation is required before a photoacoustic signal can be generated, light that is transmitted or elastically scattered by the sample is not detected and hence does not interfere with the inherently absorptive PAS measurements. This is of crucial importance when working with essentially transparent media such as pollutant-containing gases that have few absorbing centers [35]. This insensitivity to scattered radiation also permits the investigator to obtain optical absorption data on highly light-scattering materials such as powders, amorphous solids, gels, colloids, etc. Another advantage is the capability of obtaining optical absorption spectra on materials that are completely opaque to transmitted light. Coupled with this, is the capability, unique to photoacoustic spectroscopy, of performing non-destructive depth-profile analysis of absorption as a function of depth into a material[36].

2.6.1 PA theory

Consider a simple cylindrical cell as shown in Fig. 2.11. The cell has a diameter (D) and length (L). Assume that the length (L) is small compared to the wavelength of the acoustic signal and the microphone will detect the average pressure produced in the cell. The sample is considered to be in the form of a disk having a diameter (D) and thickness (l). The sample is mounted so that its front surface is exposed to the gas (air) within the cell and its back surface is against a poor thermal conductor of a thickness (l_b). The length (l_g) of the gas column in the cell is then given by $l_g = L - l - l_b$. The gas and backing materials are assumed to be not light absorbed and the dimensions of the cell are small enough to ignore convective heat flow in the gas at steady-state conditions. Note that, Only a relatively thin layer of air (~ 0.2 cm for a chopping rate of 100 Hz) adjacent to the surface of the solid responds thermally to the periodic heat flow from the solid to the surrounding air.

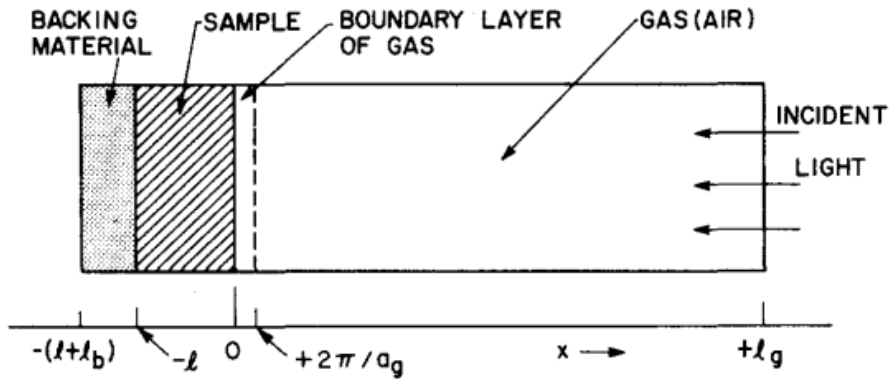


Figure 2.11: Cross-sectional view of cylindrical photoacoustic Cell.

Assume a sinusoidally chopped monochromatic light source with wavelength (λ) incident on the solid with intensity (I):

$$I = \frac{1}{2} I_0 (1 + \cos \omega t) \quad (2-6)$$

where (I_0) = incident monochromatic light flux (w/cm^2), (ω) denotes the chopping frequency of the incident light beam in radians per second. The heat density produced at point (x) due to the light absorbed at that point in solid is given by:

$$\text{Heat density} = \frac{1}{2} I_0 \beta e^{\beta x} (1 + \cos \omega t) \quad (2-7)$$

where (β) is the optical absorption coefficient of the sample in (cm^{-1}) at the wavelength (λ). The temperature in the cell obeys the thermal diffusion equation. The thermal diffusion equation in solid, taking in account the distributed heat source:

$$\frac{\partial^2 \phi_s}{\partial x^2} = \frac{1}{\alpha} \frac{\partial \phi_s}{\partial t} - A e^{\beta x} \text{Re}(e^{i\omega t}) \quad -l \leq x \leq 0 \quad (\text{Solid}) \quad (2-8)$$

Where ϕ is the temperature and

$$A = \beta I_0 \eta / 2k_s$$

where, (k_s) is the thermal conductivity of the sample and η is the efficiency at which the absorbed light at wavelength λ , is converted to heat by the nonradiative deexcitation processes. Here we consider $\eta = 1$, a reasonable assumption for most solids at room temperature. For the backing and the gas, the heat diffusion equations are given by :

$$\frac{\partial^2 \phi_b}{\partial x^2} = \frac{1}{\alpha_b} \frac{\partial \phi_b}{\partial t} \quad -l - l_b \leq x \leq -l \quad (\text{Backing}) \quad (2-9)$$

$$\frac{\partial^2 \phi_g}{\partial x^2} = \frac{1}{\alpha_g} \frac{\partial \phi_g}{\partial t} \quad 0 \leq x \leq l_g \quad (\text{Gas}) \quad (2-10)$$

where, subscripts (s), (g), (b) stands for the solid, gas, and backing material, respectively. The real part of the complex-valued solution $\phi(x, t)$ of Eqs. (2-9)- (2-10) is the solution of physical interest and represents the temperature in the cell relative to ambient temperature as a function of position and time. Thus the actual temperature field in the cell is given by:

$$T(x, t) = \text{Re}\{\phi(x, t)\} + T_0 \quad (2-11)$$

where (T_0) is the ambient temperature.

From optical point of view, sample is classified as an optically opaque when ($l > \mu_B$) while it will be optically transparent in the opposite situation ($l < \mu_B$). On the other hand sample is classified as thermally thick when ($l > \mu_s$) and thermally thin as ($l < \mu_s$). we follow the analysis of Poult and Chambron for thermally thick samples[37]; accordingly the PA amplitude (q) and phase (ϕ) are given by[33]:

$$q = \frac{A\beta\mu_s}{2\pi f e \sqrt{(\beta\mu_s + 1)^2 + 1}} \quad (2-12)$$

$$\tan\phi = \beta\mu_s + 1 \quad (2-13)$$

Where μ_s is the thermal diffusion length, β ($1/\mu_B$) is the optical absorption coefficient, e is sample thermal effusivity and A is constant (not related to the sample) given by [38]:

$$A = \frac{\gamma P_0 I_0 \sqrt{\alpha_g}}{2l_g T_0} \quad (2-14)$$

Where γ is specific heat ratio, I_0 is the incident intensity, P_0 and T_0 are ambient pressure and temperature, l_g is the length of the gas column within the cell, and α_g is the thermal diffusivity of gas. It is obvious that expressions (2-12) and (2-13) are simple and easy to use for measuring thermal properties of thermally thick samples of known β . It is clear that α can be measured using the phase measurements (Eq. (2-13)) as $\mu_s = \sqrt{\frac{\alpha}{\pi f}}$. while e can be measured using amplitude measurements. Determination of e using Eq. (2-12) requires elimination of nonrelated sample constant A . This can be done by normalization using reference sample of known thermal parameters. Accordingly, the inverse normalized amplitude (q_n^{-1}) is obtained by dividing q_r of a reference sample by q of nanofluids sample. If the reference sample has the same β then (q_n^{-1}) can be obtained as[38]:

$$q_n^{-1} = \frac{q_r}{q} = \frac{e \alpha_r^{0.5}}{e_r \alpha^{0.5}} \sqrt{\frac{(\beta \sqrt{\alpha/\pi f + 1})^2 + 1}{(\beta \sqrt{\alpha_r/\pi f + 1})^2 + 1}} \quad (2-17)$$

Eq. (17) indicates that e can be obtained by knowing thermal parameters of the reference sample (e_r and α_r) and both of α and β . The question now is how the PA technique that depends on optical absorption as a heat source can be used to measure thermal properties of non-absorbing liquids. To solve this contradictory, we suggest utilizing a dye agent with a concentration that does not affect thermal properties of the liquids. This method allows production of PA signal due to light absorption within the sample, consequently the condition of effective transparency of samples required by open PA cell technique is not necessary here. As a result, this method is suitable for measuring thermal properties of nanofluids with low as well as high volume concentration[36].

2.7 Some important related papers in Literature

- **Dmitriy A. Dikin, et al. [9]**, They prepared and characterized a free-standing graphene oxide paper by assembling individual graphene oxide sheets using a flow-directed process. They then evaluated its mechanical properties and showed that the resulting material had high stiffness and strength while remaining flexible, which they attributed to an interlocking, tile-like arrangement of the graphene oxide sheets
- **Juyeong Oh, et al. [39]**, They applied high-frequency electrical resonance measurements under electromagnetic illumination to graphene oxide-based devices. By analyzing the resonance spectra and resistance obtained through de-embedding, they investigated the band properties of graphene oxide and their relationship to photon energy, thereby probing both the optoelectronic performance and band structure of the devices.
- **S.S. Fouad, et al. [40]**, They deposited CZTS thin films of varying thicknesses on glass substrates using a chemical bath deposition method and systematically studied how deposition conditions affected their structural, optical, optoelectrical, and electrical properties. They analyzed crystal structure, band gap, nonlinear optical behavior, and temperature-dependent conductivity as functions of film thickness and deposition time. Based on the optimized film properties, they fabricated an Al/n-Si/p-CZTS/Au heterojunction device and evaluated its photovoltaic performance, achieving a solar conversion efficiency of 3.37%.
- **Hanaa Zaka, et al. [41]**, They deposited zinc oxide thin films of different thicknesses on glass substrates at 200 °C and measured the film thickness using a stylus profilometer. They examined the structural properties by X-ray diffraction and found the films to be amorphous. They evaluated a wide range of optical parameters by calculating dispersion properties, determining the optical band gap and Urbach energy using the Tauc model, and analyzing dielectric behavior. In addition, they derived optical, electrical, and thermal conductivities along with related loss and energy parameters to comprehensively characterize the optical performance of the ZnO films.
- **A.S. Hassanien, et al. [42]**, They deposited non-crystalline $\text{Cd}_{50}\text{S}_{50-x}\text{Se}_x$ thin films with varying selenium content onto glass substrates using thermal evaporation under high vacuum, while keeping the deposition rate and film thickness constant. They confirmed the amorphous nature and chemical composition of the films using XRD and EDX.

They investigated the optical properties through corrected transmittance and reflectance measurements, analyzed the variation of the optical band gap and Urbach energy with Se content, and interpreted these trends using the chemical bond approach model. In addition, they evaluated optical constants and conductivity, and applied the Wemple–DiDomenico single-oscillator model to study refractive index dispersion and related energy parameters as functions of selenium concentration.

- **Nagi M. El-Shafai, et al.** They synthesized a GO@Fe₃O₄ quantum dot nanocomposite and investigated its electrochemical and optical properties using cyclic voltammetry, current–voltage measurements, and photoluminescence analysis. They characterized the nanocomposite by TEM, XRD, and zeta potential measurements. They demonstrated that the reduced band gap and high surface area of GO loaded with Fe₃O₄ nanoparticles enhanced charge transfer and optical activity compared to pristine GO. They evaluated photoinduced charge transfer through dye degradation experiments using UV–Vis spectroscopy, analyzed electron–hole recombination behavior by PL and I–V techniques, and assessed the material’s adsorption performance for insecticides and heavy metal ions, finding that the adsorption followed a pseudo-second-order kinetic model.
- **S. Rajeshkumar.** [43], They synthesized gold nanoparticles using an eco-friendly biological method involving marine bacteria *Enterococcus* sp. They monitored nanoparticle formation through color change and surface plasmon resonance spectroscopy, and confirmed crystallinity, morphology, size, elemental composition, and functional groups using XRD, TEM, EDX, and FTIR analyses. They then evaluated the biological activity of the synthesized nanoparticles and demonstrated significant anticancer effects against HepG2 and A549 cancer cell lines, highlighting the potential of this green synthesis approach for biomedical and targeted anticancer applications.
- **Hajipour, et al.**[44], They synthesized nanocrystalline CuO, CuO–GO, and CuO–GO–Ag nanocomposites using a chemical bath deposition method, incorporating graphene oxide nanosheets and silver nanoparticles into the precursor solutions. They characterized the structural, morphological, and chemical properties of the materials using SEM, EDS, elemental mapping, and FTIR. They evaluated the antibacterial performance of the synthesized nanocomposites against *Staphylococcus aureus* and *Escherichia coli* using disc diffusion and MIC tests. They found that the CuO–GO–Ag

nanocomposite exhibited significantly enhanced antibacterial activity under visible light compared to CuO and CuO–GO, which they attributed to reduced agglomeration and the synergistic effects of GO and Ag.

- **Tahereh Shakerian Ardakani, et al.**[45], They synthesized $\text{Fe}_3\text{O}_4@Au/rGO$ nanocomposites with different graphene contents using a hydrothermal method and characterized their structural, morphological, and optical properties using multiple techniques. They experimentally measured the heat generation of nanocomposite suspensions under near-infrared laser irradiation as functions of concentration, irradiation time, and graphene content. They showed that the temperature rise increased with higher graphene content and concentration, and they proposed these nanocomposites as effective nanosources for photothermal applications and related biomedical and sensing uses.
- **M. Nabil, et al.** [46], They prepared Ag/ Fe_3O_4 nanocomposites using laser ablation and studied the effect of adding the surfactant Triton X-100 on their optical absorption and photothermal conversion. The nanocomposites were characterized by EDX, XRD, and HRTEM to confirm composition, crystalline structure, and morphology. They analyzed optical properties, including energy gap, refractive index, and electronic polarizability, and calculated related molar parameters. They found that adding Ag nanoparticles and Triton X-100 enhanced photothermal conversion, optical conductivity, and thermal properties, demonstrating the potential of these nanocomposites as efficient photothermal agents for applications like water desalination.
- **Jassim, et al.**[47], They investigated the random laser behavior of a near-infrared single-dye laser (LDS 821) by incorporating gold nanorods of different sizes and concentrations as scattering centers. They compared laser emission characteristics under varying nanorod dimensions and densities and demonstrated that random laser emission was achieved in all cases. They found that smaller gold nanorods and higher nanorod concentrations enabled coherent laser emission at lower pumping energies, providing insight into the operation of NIR random lasers.
- **Mon, et al.**[48], They prepared nano-liquid samples with different graphene oxide concentrations and measured their thermal diffusivity using the thermal lens method. They analyzed how thermal diffusivity varied with GO concentration and found that it increased up to an optimal level before saturating. They attributed this trend to enhanced

thermal transport mechanisms introduced by GO nanosheets and demonstrated the usefulness of the thermal lens technique for characterizing thermal properties of nanofluids intended for thermal management applications.

Chapter 3

Experimental work

Experimental work

3.1 Materials

First graphite rods from (Sigma Aldrich), Fe_3O_4 cube was supplied from (SAMMLUNG VON) and a high purity Au slab (99.99%) from (Sigma Aldrich). All of the materials were washed using ultrasonic bath for 10 min and then were cleaned with distilled water.

3.2 Pulsed laser ablation system

Fig. 3.1 shows the experimental setup for laser ablation of solid metal target immersed in water or aqueous solution, Nd-YAG laser 1064nm and/or 532 nm (frequency doubled) wavelength was used, where its beam was reflected by a mirror set at 45 degrees and then focused by using a converging lens (focal length=10 cm) onto a target. The ablation process was typically done at room temperature. The target was fixed by a holder at the bottom of a quartz container.

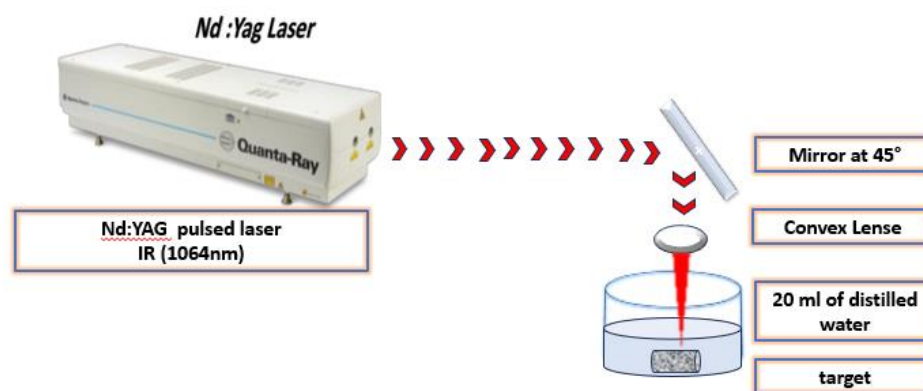


Figure 3.1: Experimental setup for nanoparticles synthesis, by laser ablation technique.

3.3 General experimental process for nanoparticles formation

The graphite rod was fixed at the bottom of 20 ml of distilled water then Q-switched Nd:YAG Laser with wavelength 1064nm, pulse width (8 -12) ns, repetition rate 10 HZ, spot size ≤ 10 mm and 450 mj was focused on the target by a converging lens of 10 cm focal length for 60 min; a solution of GO nanosheets was simply formed. See fig.3.2.

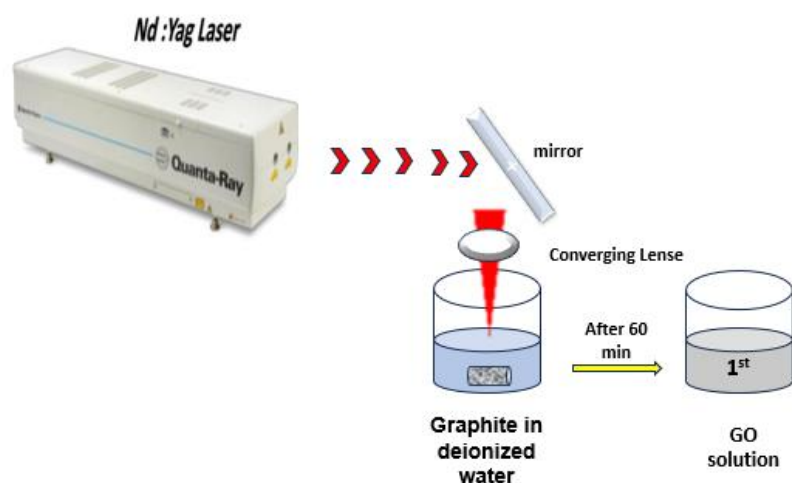


Figure 3.2: Experimental set up for GO preparation

$\text{Fe}_3\text{O}_4/\text{GO}$ has been obtained by immersing a cube of Fe_3O_4 in GO solution which was ablated by laser for 5, 10, 15, 20, 25 and 30 min. The set up is shown in Fig.3.3.

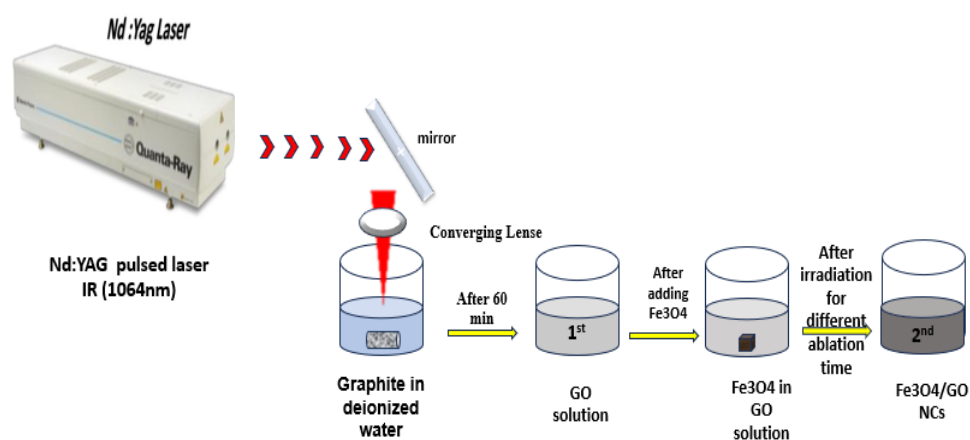


Figure 3.3: experimental set up of $\text{Fe}_3\text{O}_4/\text{GO}$ NCs

Also, $\text{Au}@\text{Fe}_3\text{O}_4$ NCs was prepared by the same technique; first a Fe_3O_4 cube was immersed at 20ml below distilled water surface and radiated for 5min, then Au plate was fixed at the bottom of Fe_3O_4 solution and ablated for 5, 10, 15 25, 45 and 65 min; resulting the formation of $\text{Au}@\text{Fe}_3\text{O}_4$ NCs. see Fig.3.4.

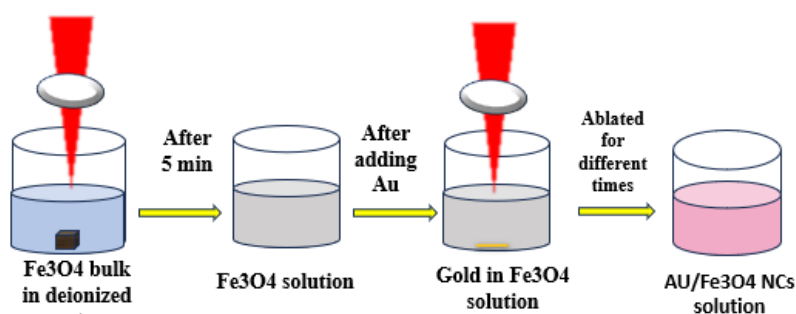


Figure 3.4: The preparation steps of Au@Fe₃O₄

The solution of GO nanosheet (at 60 min.) and Au@Fe₃O₄ solution (at 56 min) were added to each other at different ratios, So four samples of Au@Fe₃O₄: GO at ratios 1:1, 1:2, 1:3 and 1:4 were prepared and then named S1, S2, S3 and S4 respectively. All the samples were sonicated for 30 min.

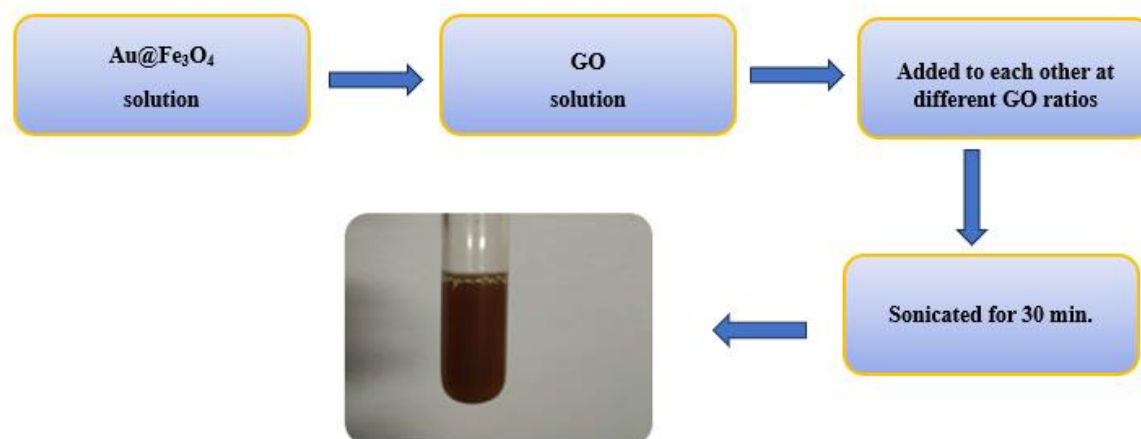


Figure 3.5: systematic diagram of synthesized Au@Fe₃O₄/GO nano fluid.

3.4 Laser source and measurements device

3.4.1 Nd-YAG laser

The Quanta-Ray® Lab series represent the intermediate range of oscillator-only lasers with output energies up to 1 J at 1064 nm. The Lab laser stands above its competitors because of its dual Nd:YAG rod and dual pump chamber oscillator configuration. This proprietary design provides intra-oscillator compensation for thermally-induced birefringence in the Nd:YAG rod, greatly reducing beam depolarization. This results in higher repetition rates, higher average

powers and superior output beam quality than any other oscillator-only Nd:YAG laser on the market. The used model is (Quanta Ray) Lab-150. There are more of its specifications displayed in table 3-1, 3-2 and 3-3[49].

Table 3-1: Quanta-Ray Lab-150- Series energy per pulse.

Product ¹	Lab-130-			Lab-150-		
Repetition Rate	10 Hz	30 Hz	50 Hz	10 Hz	30 Hz	50 Hz
Energy (mJ/p)²						
1064 nm	450 mJ	275 mJ	200 mJ	650 mJ	500 mJ	300 mJ
532 nm	200 mJ	100 mJ	70 mJ	300 mJ	200 mJ	100 mJ
355 nm ²³	90 mJ	40 mJ	30 mJ	150 mJ	100 mJ	40 mJ
EEO-355 nm ^{3, 23}	--	--	--	--	--	--
266 nm	55 mJ	25 mJ	15 mJ	75 mJ	35 mJ	25 mJ

Table 3-2: Quanta-Ray Lab-150- Series pulse width.

Performance Specifications			
Wavelength	Pulse Width ⁵	Short Term Energy Stability ⁶	Long Term Power Drift ⁷
1064 nm	8-12 ns	±2%	<3%
532 nm	1-2 ns <1064 nm	±3%	<5%
355 nm	2-3 ns <1064 nm	±4%	<6%
266 nm	3-4 ns <1064 nm	±8%	<10%

Table 3-3: Quanta-Ray Lab-150- Series beam specifications.

Beam Specifications		
Spatial Mode Profile ⁸	Standard Fit	ESM Fit ⁹
Near Field (1 m)	>70%	Contact Spectra-Physics
Far Field (∞)	>95%	Contact Spectra-Physics
Modulation ¹⁰	<40%	Contact Spectra-Physics
Beam Diameter ¹¹	<10 mm	
Beam Pointing Stability ¹²	<±50 μ rad	
Beam Divergence ¹³	<0.5 mrad	
Lamp Lifetimes ¹⁴	30 million pulses	

The energy of the incident laser pulse was measured using (COHERENT- LASERMATE/D) power meter.

3.4.2 UV- visible spectrophotometer

Absorbance spectra (SPE spectra) of NPs solution were measured by UV- Vis double-beam spectrometer type (JASCO V-670). It utilizes a unique, single monochromator design covering a wavelength range from 190 to 2700 nm. The monochromator features dual gratings (automatically exchanged): 1200 grooves/mm for the UV/VIS region; 300 grooves/mm for the NIR region. PMT detector is provided for the UV/VIS region and a Peltier-cooled PbS detector is employed for the NIR region. Both gratings and detector are automatically exchanged within the user-selectable 800 to 900 nm range. Two graphical user interfaces are included: remote module (IRM) with a color LCD touch screen and Spectra Manager™ II software as depicted in Fig. 3.6(a). The instrument is equipped with two separate sample holders, one for the sample and the other one for the reference. For liquid samples, cuvettes are used to position the samples correctly. The reference sample is needed to compensate for background signal due to the solvents used and the material of the cuvettes and also to compensate for intensity oscillations of the light source. The V-670 type offers flexible support for various liquid and solid samples and measurement methods, and its function is enhanced by a range of optional accessories and programs. Above, the IRM-700 display shows the results of a reflectance spectrum measurement of a film used for food packaging using the SLM-737 single reflection measurement unit Fig. 3.6(b). The film thickness is calculated from the interference fringes using the optional film thickness calculation program. Another accessory is using the ISV-722 integrating sphere accessory and the PSH-001 Powder sample holder to measure the reflectance spectral of the sample Fig. 3.6(c). All spectra were measured at room-temperature in a quartz cell with 1 cm optical path. The obtained absorption curve was used to study the optical parameters of the samples, including bandgap (E_g), optical conductivity (σ), absorption coefficient (α), urbach energy (E_U), electronegativity (Δx), refractive index (n), steepness parameter (σ_s), electron-phonon interaction (E_{e-p}), electronic polarizability (α_e), molar volume (V_m), molar refraction (R_m) and molar electronic polarizability (α_{me}).

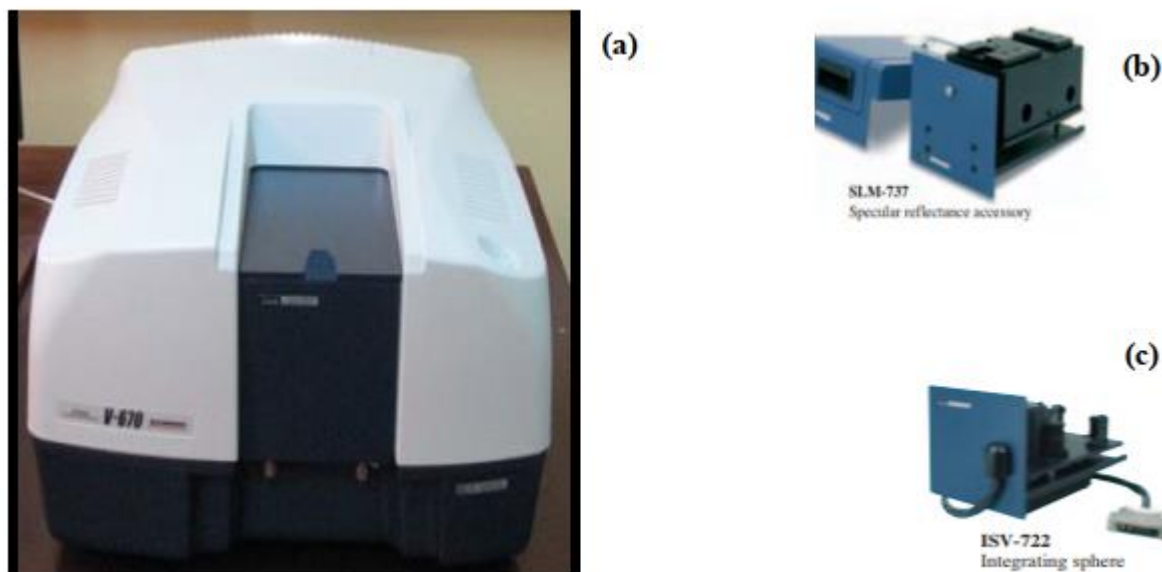


Figure 3.6: Photograph of (a) V-670 UV-Vis Spectrophotometer, (b) specular reflectance accessory, and (c) integrating sphere accessory.

3.4.3 High resolution transmission electron microscopy (HRTEM).

High resolution transmission electronic microscopy (HRTEM, JEOL JEM-2100 operated at 200KV with high-resolution Gatan CCD bottom camera, Orius SC200) at EL-Azhar university has been used. HRTEM is a powerful tool for morphology characterizations of NPs, which uses a highly energetic electron beam instead of light to "image" the specimen. The resolution of HRTEM is much higher than optical microscopes because the wavelength of an electron is much smaller than that of a photon of visible light. The point-to-point resolution of a commercial Field Emission TEM is as low as 0.19 nm. In the electron microscope, an electron has a mass that is approximately 1/1836 that of the proton.

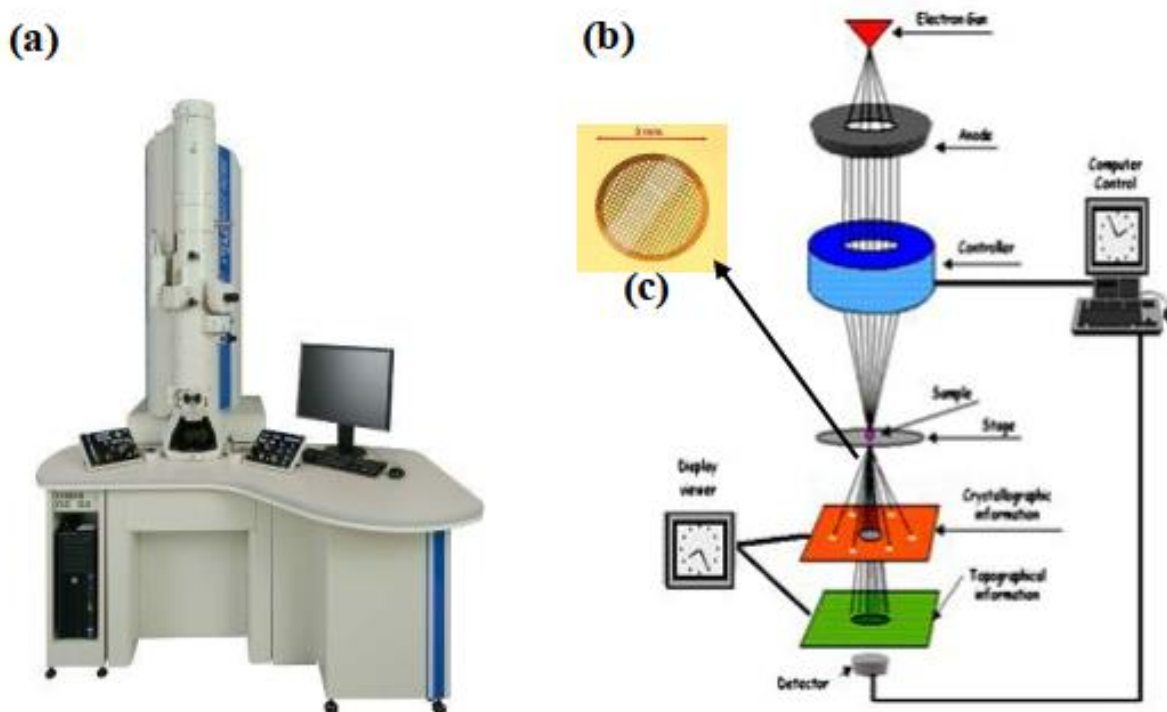


Figure 3.7: (a) Photograph, (b) Ray diagram for HRTEM, Model JEOLJEM-2100 and (c) Image of a grid used in sample preparation for HRTEM.

As shown in Fig. 3.7, the electron is transmitted through an ultra-thin specimen, interacting with the specimen as it passes through. An image is formed from the interaction of the electrons transmitted through the specimen; the image is magnified and focused onto an imaging device, such as a fluorescent screen, on a layer of photographic film or to be detected by a sensor such as a CCD camera. HRTEMs are capable of imaging at a significantly higher resolution than light microscopes, owing to the small de Broglie wavelength of electrons. Samples for HRTEM were prepared by placing a droplet of colloid suspension in a respective solvent on a Formvar carbon-coated, 300-mesh copper grid (Ted Pella) and allowing them to evaporate in the air at ambient conditions. The instrument works under a vacuum in the range 10^{-5} to 10^{-6} Pa.

3.4.4 Fourier transform infrared spectroscopy (FTIR)

Infrared, or IR, spectroscopy is a chemical analysis technique that takes advantage of the interaction between infrared light and matter. Infrared light is a part of the electromagnetic spectrum between visible light and microwaves, with wavelengths ranging

from 780 nm to 1 mm. Due to historical reasons however, we typically discuss IR light in spectroscopy in terms of wavenumbers rather than wavelengths. Wavenumbers tell us the number of wavelengths per unit distance and are given in units of cm^{-1} . Light with shorter wavelengths and higher energy will have a larger wavenumber, while light that has longer wavelengths will have lower energy and wavenumbers. Infrared light can be further divided into three categories: Near infrared (NIR), mid infrared (MIR), and far infrared (FIR). NIR has the shortest wavelength with higher wavenumbers while FIR has the longest wavelength with lower wavenumbers. Typically, when discussing IR spectroscopy MIR is the type of IR light that is used. The IR light in this range is useful because it coincides with an important property of chemical compounds: their vibrations. The atoms in chemical compounds are constantly moving and vibrating in different ways. Even in a simple molecule like water there are six different ways the molecule can vibrate: the symmetric stretch, the antisymmetric stretch, the deformation or bending vibration, rocking, twisting, and wagging. Each of these vibrations occurs at a different frequency that is unique to the chemical bond and compound. As mentioned earlier, those frequencies happen to match the frequencies of light in the MIR region of the electromagnetic spectrum.

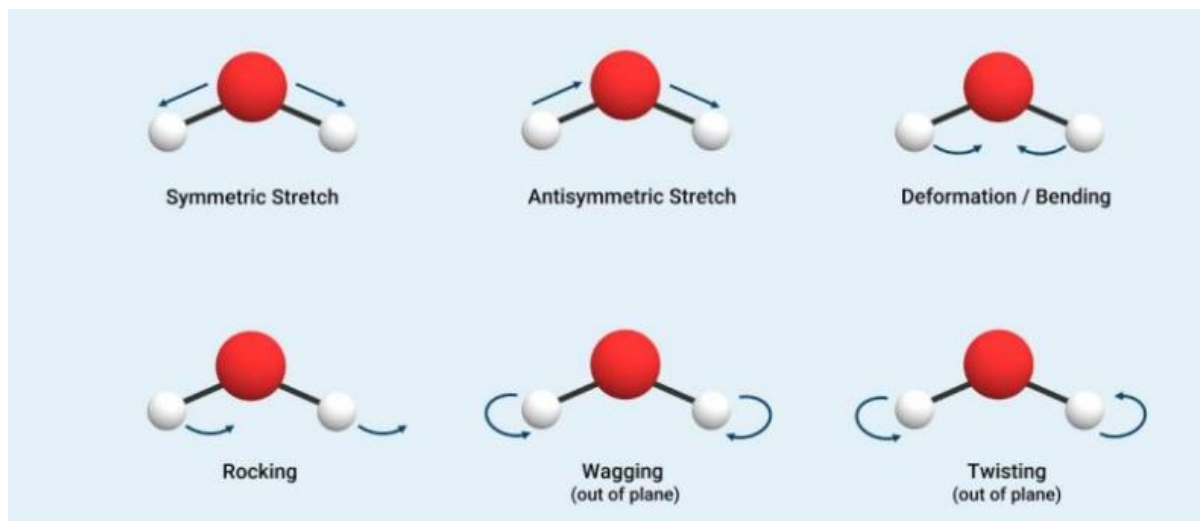
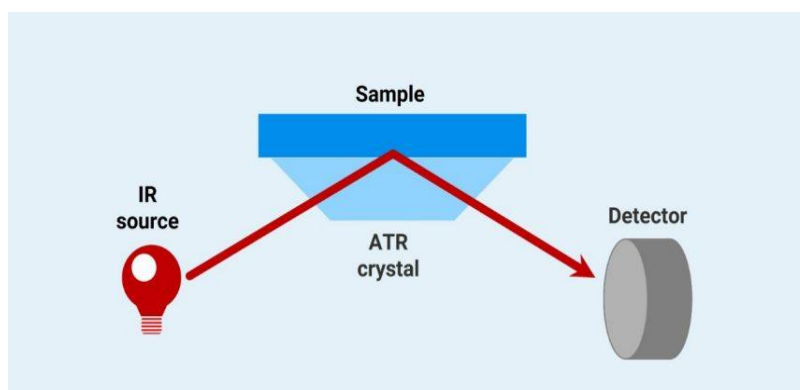
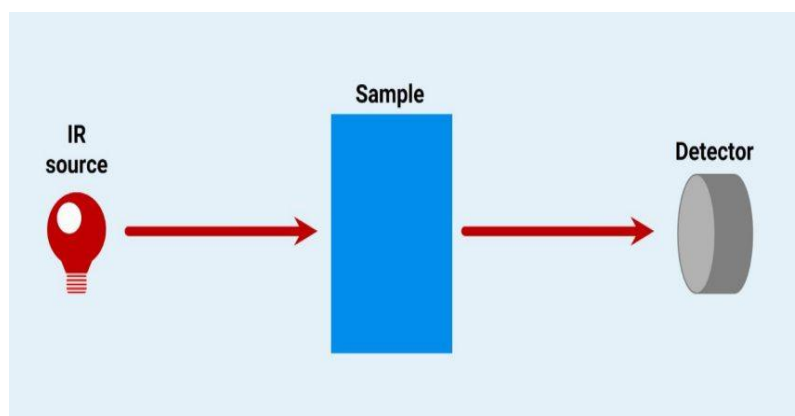


Figure 3.8: The different types of vibrations in infrared spectroscopy.

As these frequencies match those of the IR light, chemical compounds can absorb IR light which excites the vibrations in the molecules. Though IR spectroscopy has become a somewhat

general term for the chemical analysis technique where molecular vibrations are detected using IR light, the technique most frequently used is Fourier Transform IR Spectroscopy (FT-IR). In which a mathematical operation, called a Fourier transform, is used to convert the data into the familiar IR spectrum obtained from IR spectroscopy. There are three main measurement techniques that can be used during FT-IR spectroscopy: Transmission, Attenuated Total Reflection (ATR), and Reflection. Though all techniques rely on the underlying theory behind FT-IR spectroscopy, each technique uses a slightly different process to analyse the sample and is suitable for different purposes.



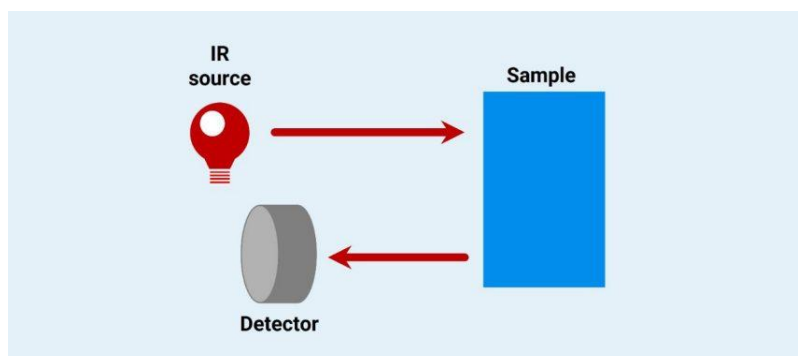


Figure 3.9: The three main measurement techniques Transmission, Attenuated Total Reflection (ATR), and Reflection respectively.

The FTIR is a Bruker Alpha II FTIR spectrometer with a diamond crystal ATR (Attenuated Total internal Reflectance) accessory at Ain-shams university was used. Measurements of liquid and solid samples can be made directly without the need for salt plate or specialized sample handling. The spectrometer runs Opus 7.8 software[50].

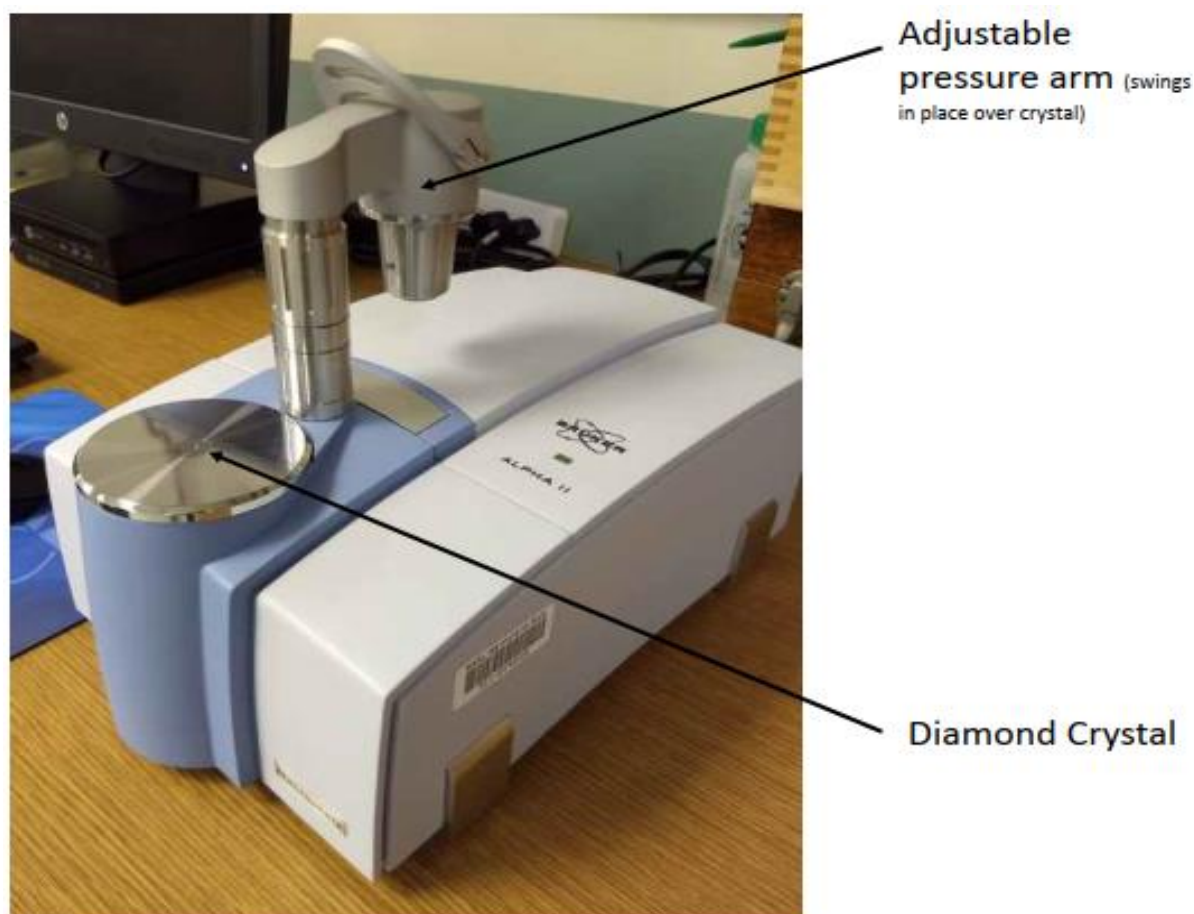


Figure 3.10: Alpha II FTIR with Platinum ATR Module

3.4.5 Photoacoustic characterization

The thermal properties measurements were carried out using Photoacoustic spectroscopy (PA) technique. The light beam from 6 W (450 nm) diode laser was mechanically modulated by an optical chopper (SR540), and focused onto the sample which was mounted carefully inside a PA cell (MTEC Model 300). The sound wave generated from the sample can be subsequently detected as an acoustic signal by a highly sensitive electrical microphone fixed in the PA cell. The PA signal was then amplified by a low noise preamplifier and further processed using a lock-in amplifier (Stanford Research System, Model SR830 DSP). A personal computer was interfaced to the system for automatic data acquisition and analysis. A schematic diagram of the PA experimental set-up for thermal properties measurements was shown in Fig. 3.11

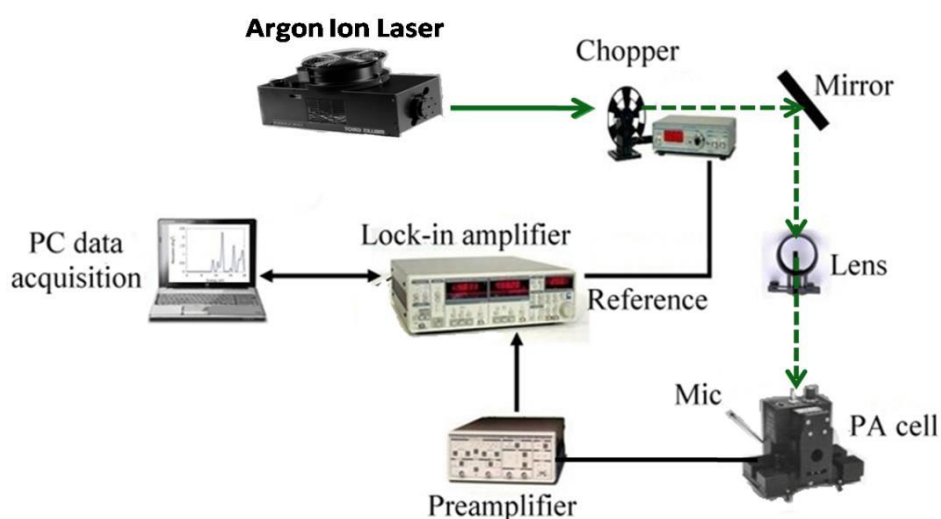


Figure. 3.11: A schematic diagram of photoacoustic technique.

Model MTEC 300 PA cell.

The Model 300 enables measurement of absorption spectra of solids primarily as an accessory in an FTIR spectrometer. The detector can be used for a wide range of measurements. The Model 300 (PAC300) as depicted in Fig. 3.12, is designed for ease of use. It mounts in the standard FTIR slide mount fixture. Sample changing, purging, and sealing are controlled by a single lever. Detector preamplifier gain is controlled by a 12 position switch on the detector, and the detector is powered by a 115/230 V, 60/50 Hz desktop power supply with an IEC 320 input jack. The photoacoustic detector increases laboratory productivity by quickly measuring FTIR spectra of solid, semi-solid, and liquid samples in any form without sample preparation.

The PAC300's operating modes include depth profiling, photoacoustic absorbance, diffuse reflectance, and transmittance with capabilities for both macro and micro samples. No other single accessory provides such a wide range of applicability

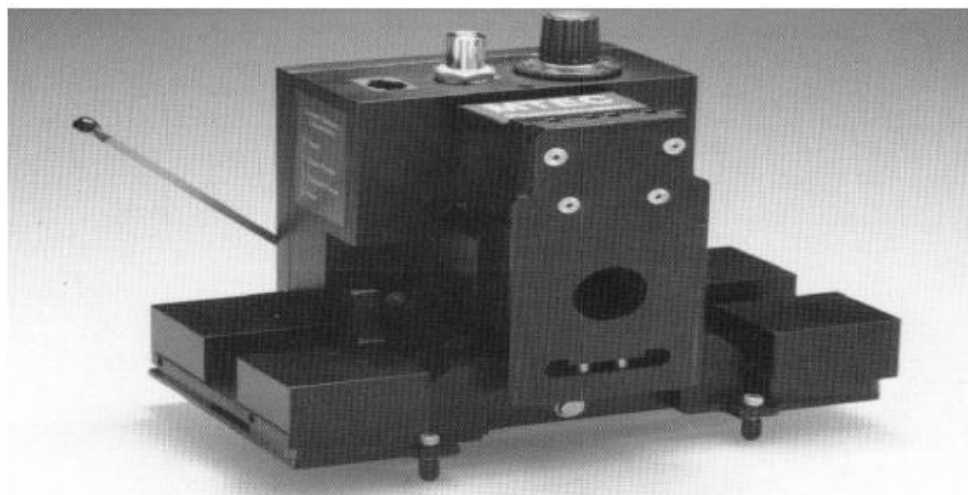


Figure. 3.12: Extra support screws installed at the front of the detector.

Sample Cup Loading.

The MTEC Model 300 is supplied with five small and five large sample cups and five brass spacer inserts. The cups and inserts fit into a brass holder which is attached to the black sample holder handle as shown in Fig. 3.13.



Figure. 3.13: Sample holder with brass inserts and small and large cups.

Model SR 830 lock-in amplifier.

Much of modern experimental physics involves pulling a small signal out of a forest of noise. The most common technique for this—and probably the most accessible—is phase-sensitive detection. While the implementation of this technique has evolved considerably since its

invention by Bob Dicke in the 1940s, the underlying principle remains the same as depicted in Fig. 3.14.



Figure 3.14: Lock - in amplifier model (SR 830)

Lock-in measurement requires a frequency reference. Typically, an experiment is excited at a fixed frequency (from an oscillator or function generator), and the lock-in detects the response from the experiment at the reference frequency. In the following diagram, the reference signal is a square wave at frequency (ω_r). This might be the sync output from a function generator. If the sine output from the function generator is used to excite the experiment, the response might be the signal wave shown below. The signal is:

$$V_{sig} \sin(\omega_r t + \theta_{sig}) \quad (3-1)$$

Where (V_{sig}) is the signal amplitude, (ω_r) is the signal frequency, and (θ_{sig}) is the phase of the signals. Lock-in amplifiers generate their internal reference signal usually by a phase-locked – loop locked to the external reference. In the diagram, the external reference, the lock-in's reference, and the signal are all shown. The internal reference is:

$$V_L \sin(\omega_L t + \theta_{ref}) \quad (3-2)$$

The lock-in amplifies the signal and then multiplies it by the lock-in reference using a phase-sensitive detector or multiplier. The output of the (PSD) is simply the product of two sine waves. The lock-in amplifies the signal and then multiplies it by the lock-in reference using a phase-sensitive detector or multiplier. The output of the (PSD) is simply the product of two sine waves.

$$\begin{aligned}
 V_{psd} &= V_{sig} V_L \sin(\omega_r t + \theta_{sig}) \sin(\omega_L t + \theta_{ref}) \\
 &= \frac{1}{2} V_{sig} V_L \cos([\omega_r - \omega_L]t + \theta_{sig} - \theta_{ref}) \\
 &= \frac{1}{2} V_{sig} V_L \cos([\omega_r + \omega_L]t + \theta_{sig} + \theta_{ref})
 \end{aligned}
 \tag{3-3}$$

The (PSD) output is two (AC) signals, one at the difference frequency ($\omega_r - \omega_L$) and the other at the sum frequency ($\omega_r + \omega_L$).

Chapter 4

Results and Discussions

Results and Discussions

This thesis represents the synthesis and surface modification of graphene oxide (GO) nanosheets using pulsed laser ablation in liquid (PLAL). Initially, GO was synthesized by ablating a graphite target in deionized water, resulting in high purity nanosheets. These GO nanosheets were then functionalized with magnetic Fe₃O₄ nanoparticles to enhance their magnetic and functional properties. To further improve their physicochemical characteristics and expand their potential for multifunctional applications, a bimetallic Au@Fe₃O₄ nanocomposite was subsequently added onto the GO surface. This chapter provides a detailed discussion of the structural, morphological, and compositional features observed at each stage of the process. The optical and thermal properties are also calculated.

4.1 Characterization of GO nanosheets

As presented in the experimental section, GO nanosheets were prepared using the PLA technique. The properties of the obtained samples were characterized by using various characterization techniques; HRTEM microscopy, FT-IR, UV-Vis spectroscopy and PA technique.

4.1.1 High resolution transmission electron microscopy

High resolution transmission electron microscopy (HRTEM) was employed to evaluate the morphology and shape of the prepared sample, The obtained micrographs of GO at resolution 200 nm and 20 nm are shown in Fig. 4.1(a,b) respectively.

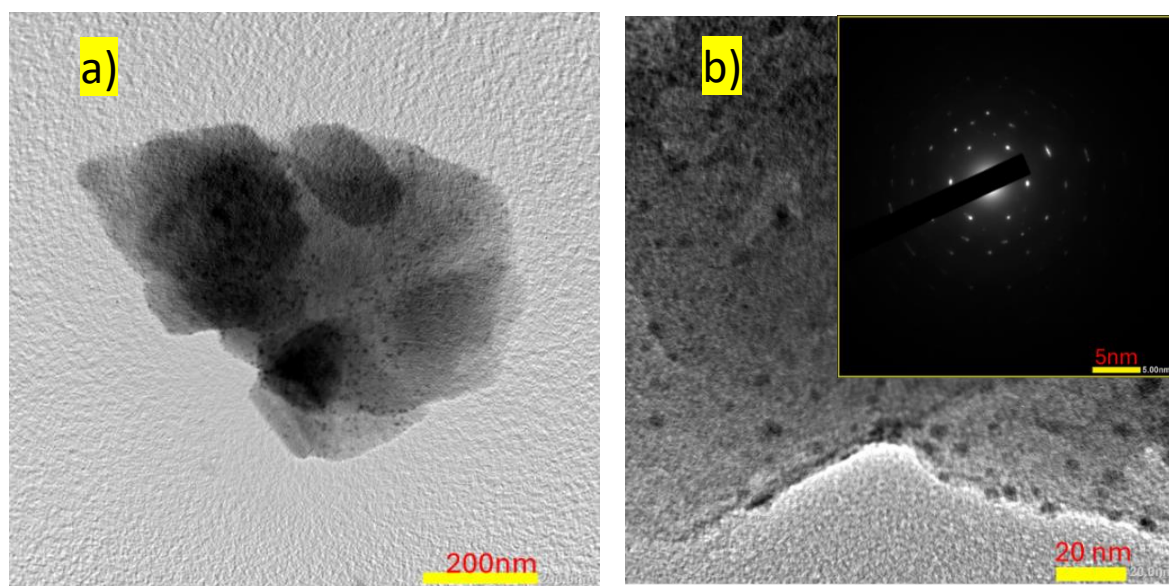


Figure. 4.1:HRTEM images of GO at different resolutions a) 200 nm, b) 20 nm and the inset of b) is the SAED image at 5 nm

They reveal the crumpled nature, some agglomerations may have occurred during drying of the samples on the TEM grid. It is easily observed that at resolution 20 nm some dots are observed which are not seen at lower resolution. This result is in a good agreement with Paola Russo, et al.[51]. In their work they found that laser ablation of a graphite target led to obtain porous graphene sheets as primary products and graphene quantum dots (GQDs) as secondary products. Fig.4.1b) shows also the selected area diffraction pattern of the sample, which reveals the single crystal structure of the sample[52][53].

4.1.2 Fourier Transform Infrared Spectroscopy (FT-IR)

Infrared spectra were measured in the range between 400 and 4000 cm^{-1} are given in Fig.4.2. The obtained spectra shows a broad band that starts from (3683) up to (2980) cm^{-1} which can be assigned to the absorbed water molecules over the nanoparticles [54]. GO Spectrum confirms the presence of carboxyl COOH (a combination of two functional groups attached to a single carbon atom, namely, hydroxyl (single-bonded OH) and carbonyl (double bonded O) groups.)(1422 cm^{-1}), the band at 1636 cm^{-1} is assigned to the bending mode of the unsaturated carbon double bond (C=C) which attributed to the fraction of sp^2 carbon atoms, and the one at 1038 cm^{-1} belongs to the stretching vibration of alkoxy C-O functional groups(containing a monovalent radical composed of an alkyl group- an alkane missing one hydrogen- united with oxygen).[17]

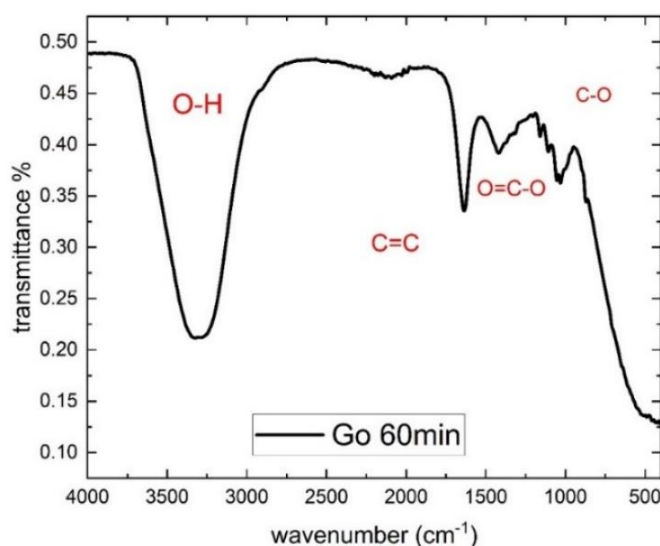


Figure. 4.2: FT-IR spectra of the prepared GO nanosheets

4.1.3 UV-Vis Absorption Spectra of GO nanosheets.

The UV-Vis absorption spectra of the prepared NP samples colloidal solution were measured and are given in Fig. 4.3.

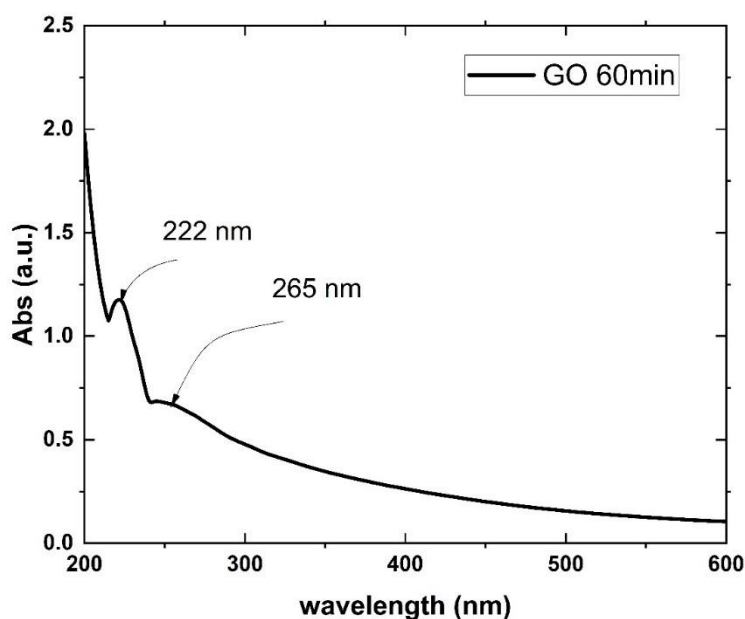


Figure. 4.3: The absorption spectra of the prepared GO nanosheets

It is observed that two absorption edges at 222 nm and 265 nm. In carbon materials containing a mixture of sp^2 and sp^3 bonding, the optoelectronic properties are determined by the π states of the sp^2 sites. The π and π^* electronic levels of the sp^2 clusters lie within the band gap of σ and σ^* states of the sp^3 matrix and are strongly localized [55]. The optical properties of disordered carbon thin films containing a mixture of sp^2 and sp^3 carbon have been widely investigated. In GO spectra the characteristic peak at 222 nm due to the aromatic transition of π - π^* belongs to the C-C bond and another peak at nearly 265 nm corresponds to n - π^* transitions of C=O [56].

The optical band gap is calculated by known Tauc's equation [57][58]:

$$(\alpha h\nu)^{1/n} = \beta(h\nu - E_g) \quad (4-1)$$

where β is a constant called the band tailing parameter, E_g is the energy of the optical band gap and n is the power factor of the transition mode = 0.5 for the direct transitions [59]. The bandgap values are established by analyzing the Tauc-plot curve of the $(\alpha h\nu)^2$ value on $(h\nu)$. Energy bandgap E_g is obtained by intercepting this linear part's extrapolation to the energy axis. Plotting $(\alpha h\nu)^2$ against photon energy $(h\nu)$ for the GO sample is shown included in Fig. 4.4, the bandgap was calculated to be 4.1 eV.

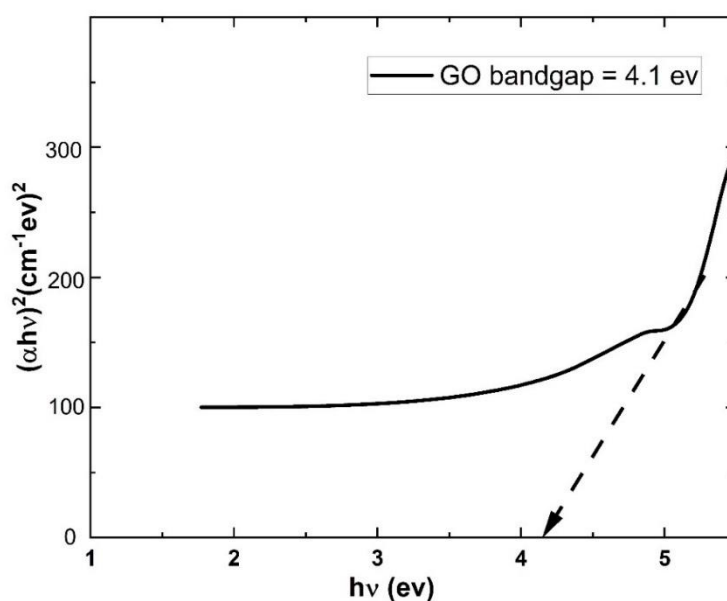


Figure. 4.4: Variation of $(\alpha h\nu)^2$ with the photon energy ($h\nu$) for GO

. Goki Eda. Et al,[60] calculated HOMO-LUMO gap of a single benzene ring is ~ 7 eV, which decreases down to ~ 2 eV for a cluster of 20 aromatic rings. So 4.1 eV bandgap is in a good agreement with [20] indicating intermediate size of the sheets.

4.2 Characterization of $\text{Fe}_3\text{O}_4/\text{GO}$ NCs

After GO nanosheets were prepared and characterized, Fe_3O_4 nanoparticles were prepared by the same technique (PLAL). $\text{Fe}_3\text{O}_4/\text{GO}$ samples were obtained by immersing Fe_3O_4 bulk in GO solution and ablated by laser for (5, 10, 15, 20, 25 and 30 minutes). The chemical and physical properties of the obtained samples were characterized by using HRTEM microscopy, FT-IR and UV-Vis spectroscopy.

4.2.1 High resolution Transmission Electron Microscopy of Fe_3O_4 NPs

Fe_3O_4 nanoparticles were prepared at different ablation times (5, 10, 15, 20, 25 and 30 minutes). Fig. 4.5 (a,b) shows the morphology of Fe_3O_4 NPs at different resolutions a) at 100 nm and b) 20 nm.

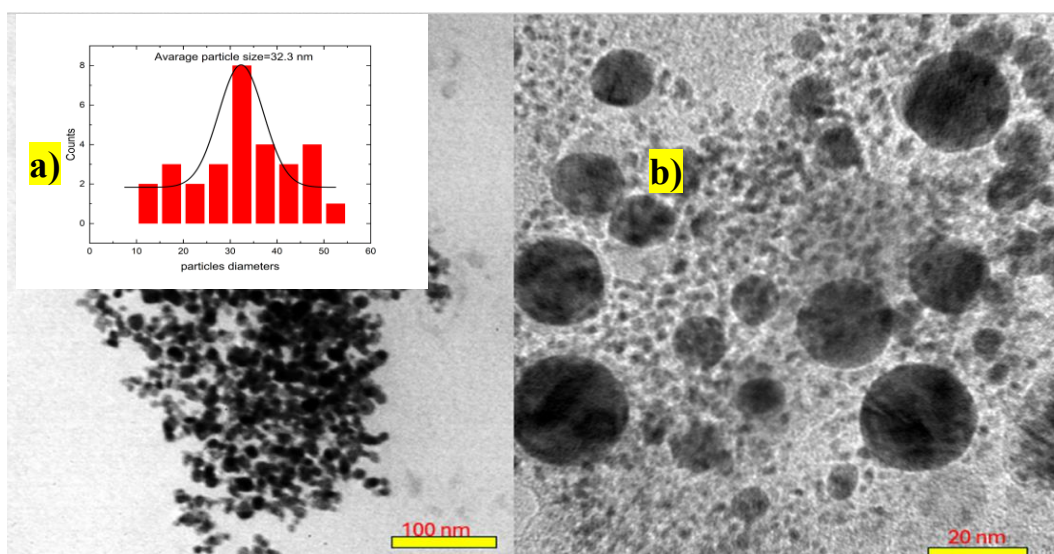


Figure. 4.5: HRTEM images of Fe_3O_4 NPs at different resolutions a) 100 nm, b) 20 nm. The inset image in a) is the histogram of NPs

It is observed that the magnetite nanoparticles have a spherical shape. Some aggregations are observed that may take place during the sample drying on the grid. The average particle size was estimated from HRTEM to be 32.3 nm. The obtained micrographs of $\text{Fe}_3\text{O}_4/\text{GO}$ at 10 min. and 25 min. ablation time as an example are shown in Fig. 4.6 (a,b).

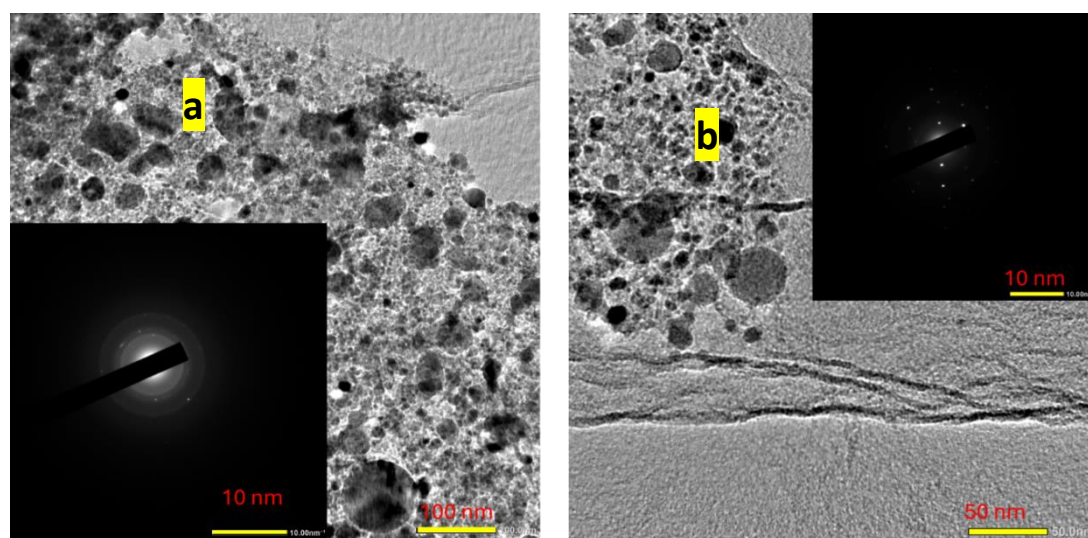


Figure. 4.6: HRTEM images of $\text{Fe}_3\text{O}_4/\text{GO}$ NCs at different resolutions a) 100 nm, b) 50 nm. The inset figure in a) and b) includes the SAED.

It is easily observed that at 10 min ablation time the Fe_3O_4 NPs have a spherical shape but the GO sheet not totally covered. The SAED images confirm the presence of NPs at some places only, where the covered sheet has a multi crystal structure otherwise it shows single crystallinity[43]. HRTEM images at 25 min. ablation time images are shown in Fig.4.7(a,b).

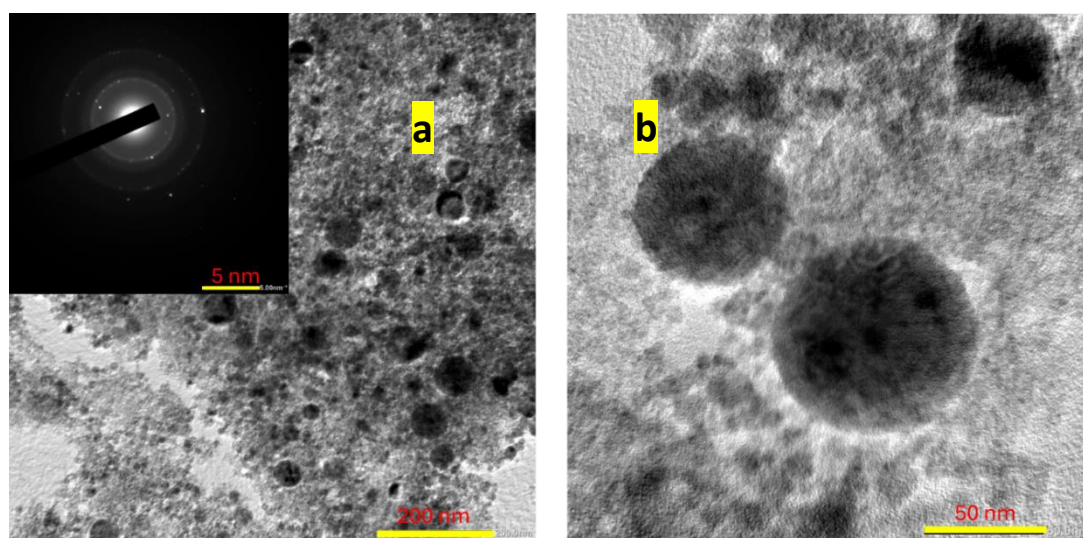


Figure. 4.7: HRTEM images of $\text{Fe}_3\text{O}_4/\text{GO}$ NCs at different resolutions a) 200 nm, b) 50 nm. The inset figure included SAED image at 5 nm.

The figure illustrates that Fe_3O_4 nano-spherical was loaded on GO nanosheets and uniformly distributed over the GO surface. It also reveals that some blanks or deformations took place in GO sheets as a result of the reduction that happened at this ablation time.

4.2.2 Fourier Transform Infrared Spectroscopy (FT-IR)

Fig.4.8 shows the transmittance curve of Fe_3O_4 NPs and $\text{Fe}_3\text{O}_4/\text{GO}$ NCs at 20 min ablation time.

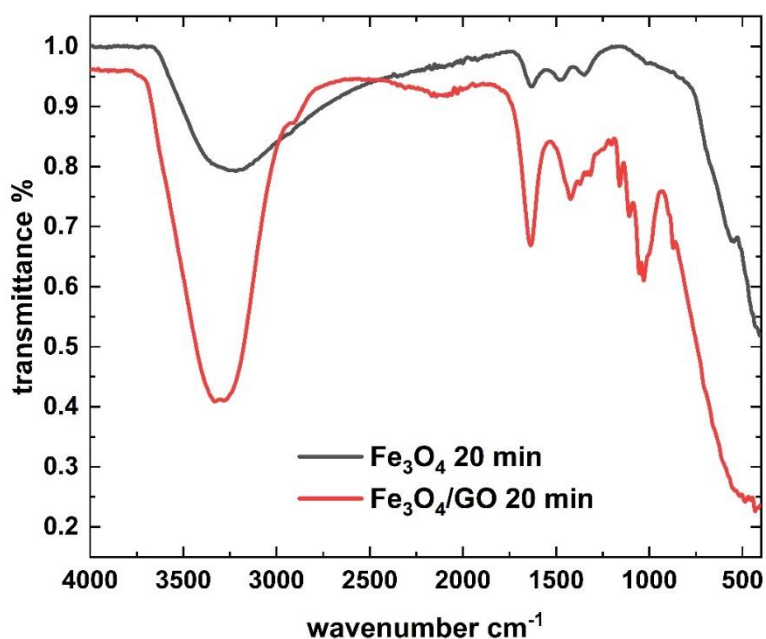


Figure. 4.8: FT-IR spectra of the prepared Fe₃O₄ NPs and Fe₃O₄/GO NCs at 20min.

The broad band that starts from (3683) up to (2980) cm⁻¹ assigned to the adsorbed water molecules over the nanoparticles. For Fe₃O₄ NPs the peak at (553 cm⁻¹) assigned to the Fe-O stretching modes of the magnetite lattice[53] and that peak at (425 cm⁻¹) suggest a cation vacancy arrangement that is creating a reduced symmetrical structure, most likely because of surface oxidation as no surfactant was used. For Fe₃O₄/GO NCs the bond of both GO and Fe₃O₄ are present and appear clearly at samples of longer ablation time. The transmittance spectrum of Fe₃O₄/GO NCs for 5, 10, 15, 20, 25 and 30 minutes is shown in Fig. 4.9.

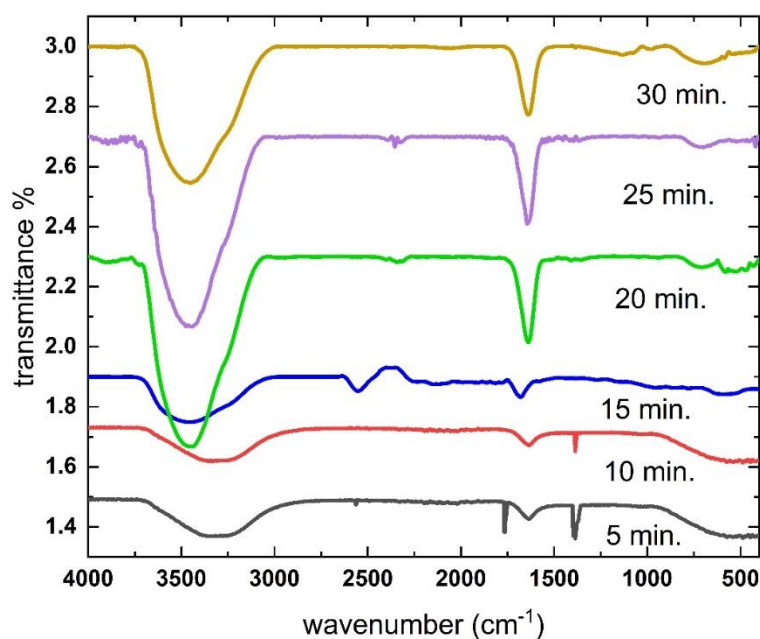


Figure. 4.9: FT-IR spectra of the prepared $\text{Fe}_3\text{O}_4/\text{GO}$ NCs at 5, 10, 15, 20, 25 and 30 min.

The graph reveals the change that has taken place with ablation time, the peak at 1636 cm^{-1} became sharper which reveal the larger ratio of sp^2 carbon atoms which reveal the reduction that has happened in the graphene oxide sheets at longer ablation time. Also some surface oxidation to magnetite exists because of its high activity. Fig. 4.10 shows spectrum of $\text{Fe}_3\text{O}_4/\text{GO}$ NCs for 20, 25 and 30 minutes from 1200 cm^{-1} to 450 cm^{-1} to focus on the change in Fe_3O_4 NPs at interacting with GO nanosheets. The band at 580 cm^{-1} and 420 cm^{-1} in the spectrum is ascribed to Fe–O stretching vibrations that indicate the formation of Fe_3O_4 nanoparticles on GO sheets which is strong at 30 min.[61]. The shift that has taken place at the peaks of magnetite confirms the interaction that happened. The presence of two bands of weak intensity at 700 and 470 cm^{-1} indicates some arrangement of cation vacancies generating a lower symmetry structure probably coming from some surface oxidation[12].

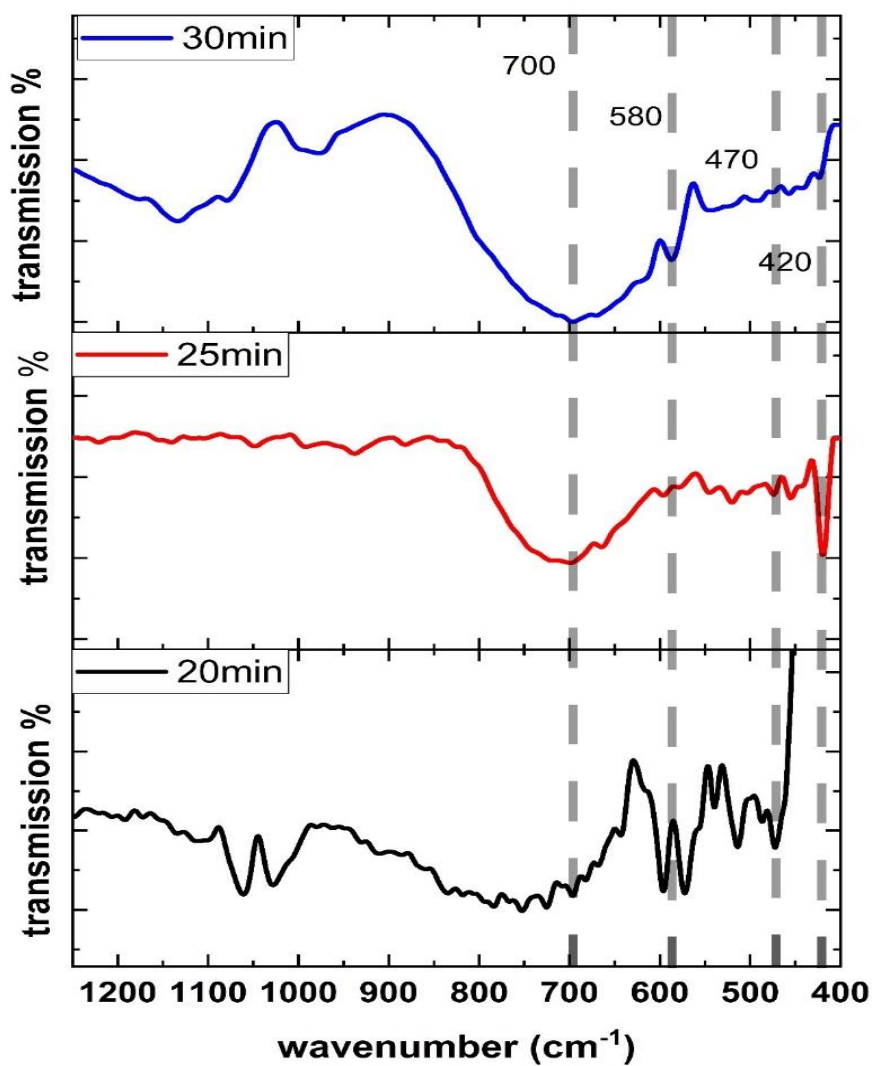


Figure. 4.10: FT-IR spectra of the prepared Fe₃O₄/GO NCs at 20, 25 and 30 min.

4.2.3 UV-Vis Absorption Spectra of Fe₃O₄ NPs

Fig. 4.11a) gives The UV-Vis absorption spectra of Fe₃O₄ NPs samples. The bandgap has been calculated for all the samples and given in Fig. 4.11b).

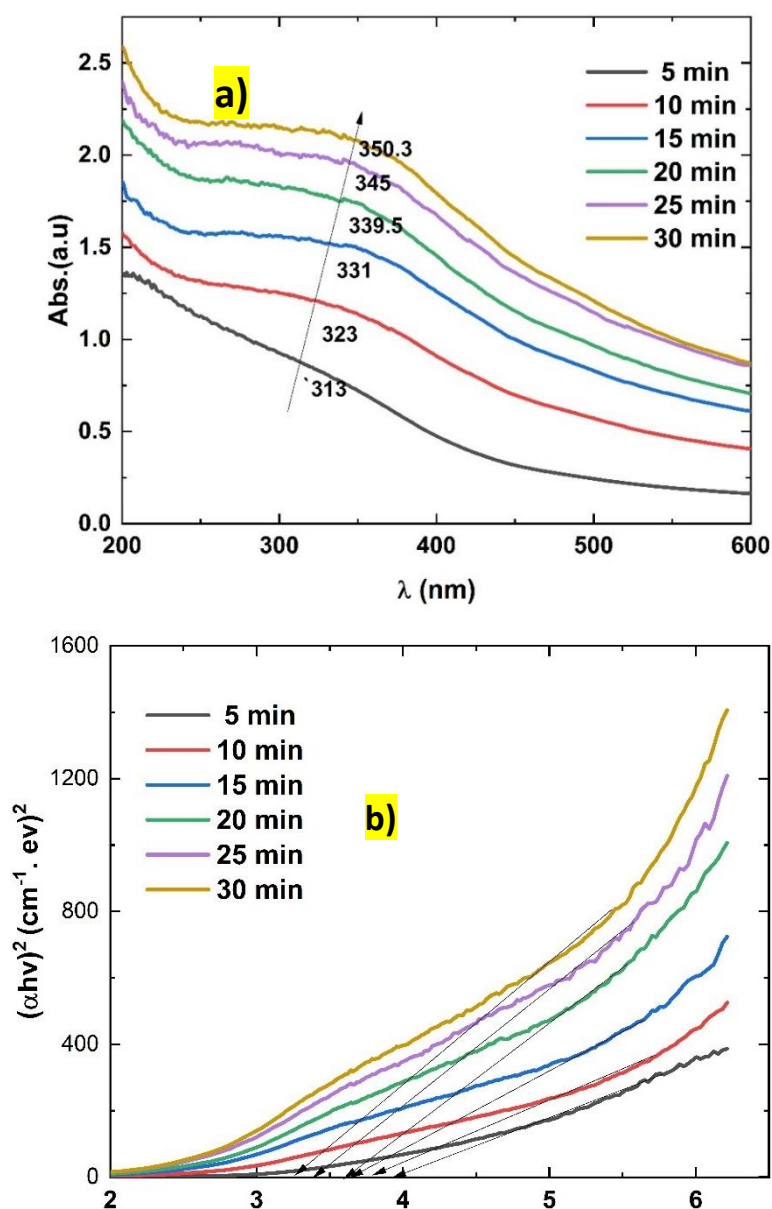


Figure. 4.11: a) The absorption spectra of the prepared Fe₃O₄ NPs, b) $\alpha h\nu^2$ was plotted versus $h\nu$ for Fe₃O₄ NPs.

Optical absorption spectra show a broad absorbance band for the Fe₃O₄ NPs samples which is mainly due to the half-metallic behavior (A half-metal is any substance that acts as a conductor to electrons of one spin orientation, but as an insulator or semiconductor to those

of the opposite orientation.) [62]. It shows an enhancement in the absorption intensity and a red shift as the ablation time increased. The absorption edges are at 313, 323, 331, 339.5, 345 and 350.2 nm for 5, 10, 15, 20, 25 and 30 minutes respectively. because longer times equate to longer growth, affording mainly larger particles during the ablation in the liquid [63]. The band gap was calculated using equation (4-1) see Fig.4.11 (b), it decreased from 3.96 eV to 3.1 eV as the ablation time increased from 5 min. to 30 min.

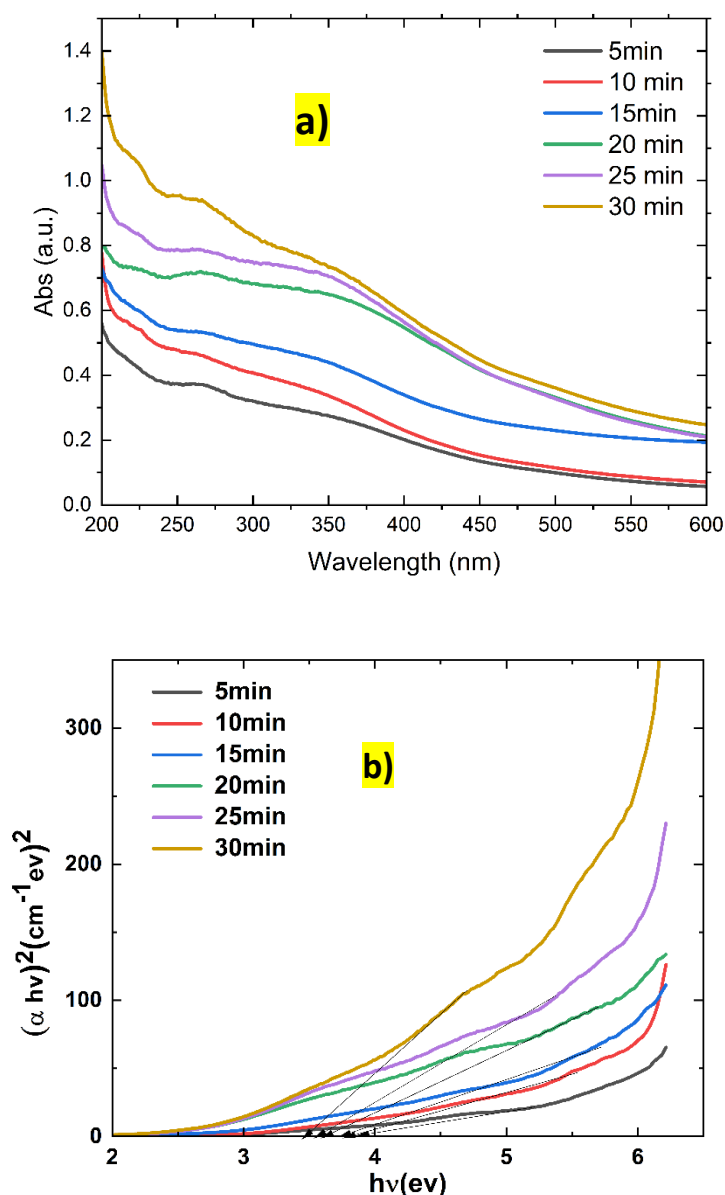


Figure 4.12: The absorption spectra of the prepared Fe₃O₄/GO and its band gap (a,b) respectively.

Fig. 4.12(a) shows the absorption curve for Fe₃O₄ /GO NCs for different ablation time. The absorption intensity increased as ablation time increased. Additionally, the peaks' width at 222 and 265 nm corresponding to GO started to increase, which confirm the change in electronic structure that has taken place or may be due to some reduction that has happened. Fig.4.12(b) gives the band gap, where it was calculated using equation (4-1) where it decreased from 3.9 eV to 3.5 eV as the ablation time increased. This change in E_g from pure GO solution is due to the presence of different oxidation states of iron in the magnetite (Fe²⁺ and Fe³⁺) which could introduce specific impurity states, particularly in the electronic structure of the material, altering the conductivity or introducing new energy levels within the band gap[64].

4.3 Characterization of Au@Fe₃O₄/GO NCs

To enhance the physical properties and develop a multifunctional nanomaterial, aiming to achieve multiple properties in a single material and after GO solution was prepared and characterized, Fe₃O₄ nanoparticles were added to GO as given in section 4.2. Au@Fe₃O₄ NCs were prepared by the same technique (PLAL) and added to GO, with different ratios of GO keeping Au@Fe₃O₄ NCs the same for all the NCs. The properties of the obtained samples were characterized by using UV-Vis spectroscopy, HRTEM microscopy, and FT-IR.

4.3.1 Characterization of Au@Fe₃O₄ NCs

As mentioned in chapter 3 Au@Fe₃O₄ NCs were prepared. First, 20 ml of deionized water in which a cube of Fe₃O₄ was placed at the bottom and ablated for 5 minutes, the cube was removed, a plate of gold was placed instead of it then ablated for 5, 10, 15, 25, 45 and 65 min.

4.3.1.1 High Resolution Transmission Electron Microscopy

Fig. 4.13 shows the HRTEM images of Au@Fe₃O₄ NCs at 65 min ablation time. It shows that the shape of the synthesized NPs was approximately spherical and their average size was about 14.3 nm. Fig.4.13 b shows a HRTEM image near the surface of Au@Fe₃O₄ NCs. The images reveal that the nanocomposite is successfully prepared.

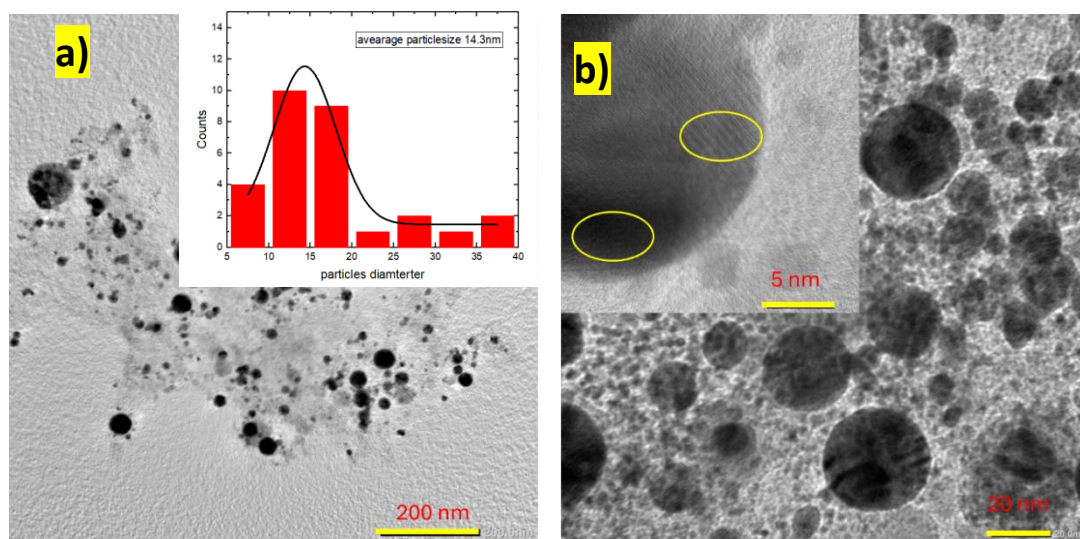


Figure. 4.13: HRTEM images of Au@Fe₃O₄ NCs at different resolutions a) 200 nm the inset image is the histogram, b) 20 nm, the inset image is at resolution 5 nm.

4.3.1.2 Fourier Transform Infrared Spectroscopy (FT-IR)

Fig.4.14 shows the FT-IR transmittance curve of Au@Fe₃O₄ NCs .

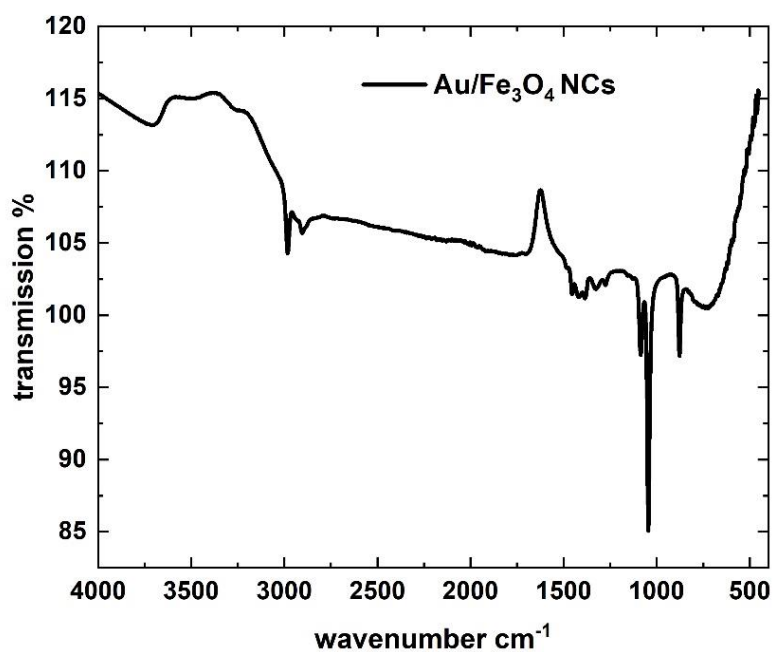


Figure 4.14: FT-IR spectra of the prepared Au@ Fe₃O₄ NCs

The transmission results in a strong bands at 3712 cm^{-1} (O-H stretching Alcohol), 2981 cm^{-1} (C-H stretching Alkane) and 2903 cm^{-1} (C-H stretching Aldehyde) and additional peaks at 1385 cm^{-1} (C-H bending Phenol), at 1086 cm^{-1} (C=O stretching of carboxylic) and 1044 cm^{-1} (CO-O-CO stretching Anhydride)[65]. The transmission bands at 581 cm^{-1} was confirmed as the Fe-O attributed to tetrahedral and octahedral sites of spinel structure, Also 461 and 724 cm^{-1} stretching frequencies due to some surface oxidation[66]. The shift that took place in magnetite peaks due to the interaction between gold and magnetite NCs. (see Fig.4.7 pure magnetite)

4.3.1.3 UV-Vis Absorption Spectra

The UV-Vis absorption spectra of the prepared NPs samples are measured and given in Fig. 4.15.

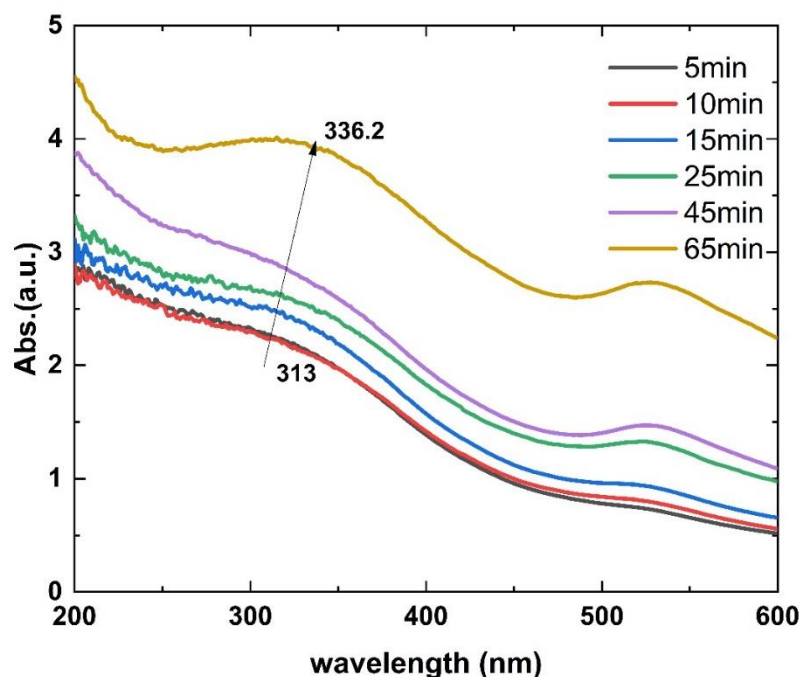


Figure. 4.15: The absorption spectra of the prepared Au@Fe₃O₄ NCs for different ablation time

As the ablation time increases from 5 to 65 minutes, there is a noticeable change in the absorption intensity and peak positions. This suggests that longer ablation times lead to increased nanoparticle concentration or changes in particle size and distribution. The shift from 313 nm to 336.2 nm is due the electronic change in Fe₃O₄ due to surface plasmon

resonance (SPR) effects of gold nanoparticles [45]. These results confirm that ablation time is a key parameter in controlling the physicochemical characteristics of the synthesized nanocomposites. The absorption spectra of Au, Fe₃O₄ and Au@Fe₃O₄ NCs are shown in Fig.4.15. The UV-Visible spectra of Au@Fe₃O₄ NCs were compared to that of bare magnetite and bare AuNPs. An absorption peak was not observed for magnetite NPs in the visible range. The characteristic SPR of bare AuNPs was observed at 520 nm, consistent with AuNPs exhibiting a mean size diameter of 10–15 nm. An SPR band was also present in the Au@Fe₃O₄ NCs, with a bathochromic (red) shift from 520 to 527 nm and a broadening of the absorption band, which can be attributed to the interaction between the pure NPs interfaces and changes in the NPs surface[67].

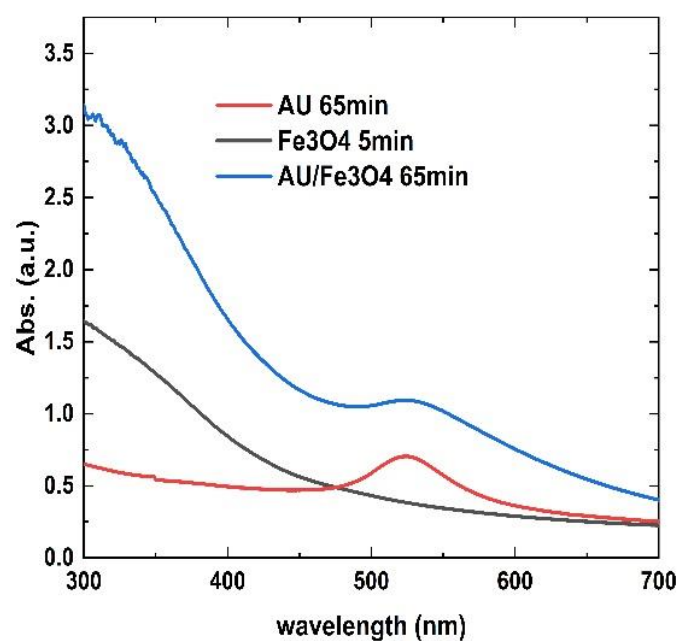


Figure 4.16: The absorption spectra of the prepared Au, Fe₃O₄ and Au@Fe₃O₄ NCs

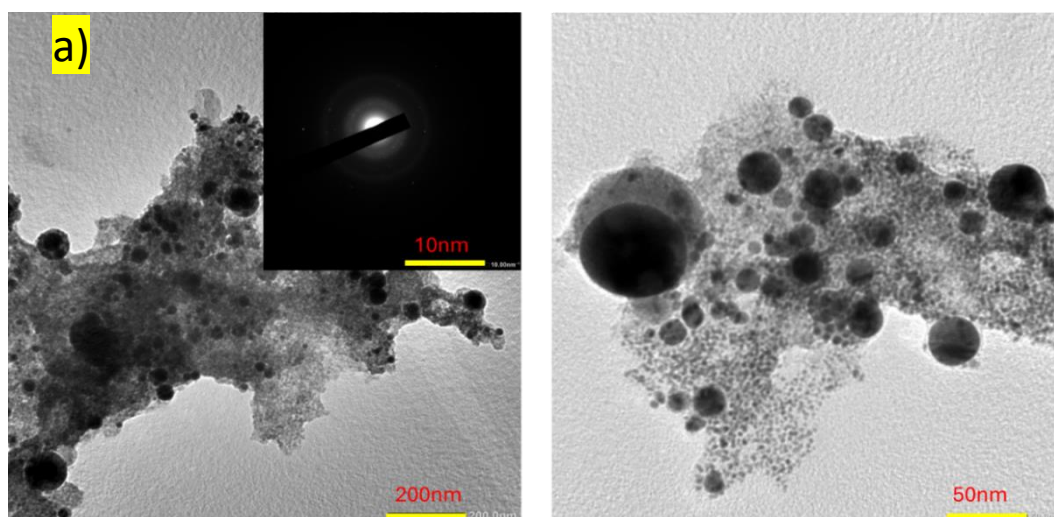
Bathochromic shifts are related to changes in the dielectric constant and interaction among nanoparticles, which can be ascribed to quantum-size effects and a higher electronic density provided by the gold in the modified nanostructures[68]. The band gap was calculated for Au@Fe₃O₄ NC where $E_g=2.55$ eV due to the introduction of nanogold which had zero bandgap.

4.3.2 Characterization of Au@Fe₃O₄ /GO NCs

After GO nanosheets and Au@Fe₃O₄ NCs were prepared and characterized, The solution of GO nanosheet (at 60 min.) and Au@Fe₃O₄ solution (at 56 min) were added to each other at different ratios, So four samples of Au@Fe₃O₄: GO at ratios 1:1, 1:2, 1:3 and 1:4. while maintaining a constant concentration of Au@Fe₃O₄ across all samples, the ratio of graphene oxide (GO) were increasing .The Au@Fe₃O₄ to GO ratios were adjusted as follows: **S1**: 1:1, **S2**: 1:2, **S3**: 1:3 and **S4**: 1:4. This systematic variation enables the investigation of how increasing GO content influences the structural, optical properties and of the nanocomposites.

4.3.2.1 High Resolution Transmission Electron Microscopy

Fig. 4.17(a,b) shows the HRTEM images of S3 as an example with and without sonication. The individual fragments of GO and Au@Fe₃O₄ are seen clearly in Fig.4.17 a), with different resolutions. They were just add to each other. On the other hand, Fig.4.17 b) shows the diffusion of the NCs in the GO sheets at different resolutions. This is due to the effect of sonication specially Cavitation When bubbles collapse, they generate localized hot spots with High Temperatures, Pressures and Rapid cooling rates, these extreme conditions create “micro-reactors” that can drive chemical reactions that would otherwise need harsh conditions[69]. Also improves mixing and diffusion, especially in heterogeneous systems, leads to more efficient contact between reactants. The SAED patterns are shown in the two cases which confirm the multicrystalline structure of both.



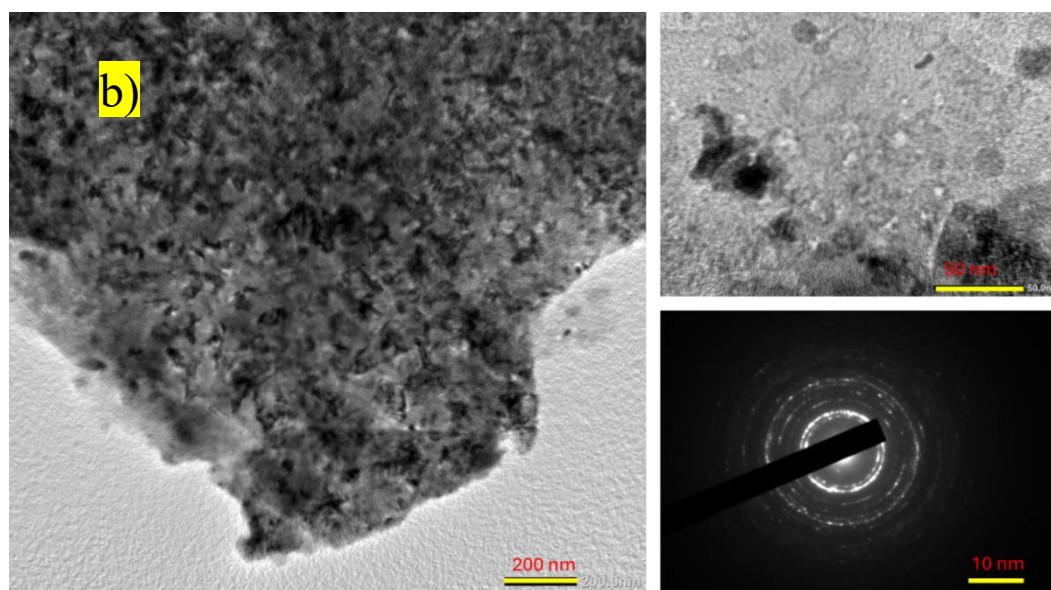


Figure. 4.17: HRTEM images of Au@Fe₃O₄/GO NCs at different resolutions 200 nm, 20 nm. a) without sonication, b) with 30 min. sonication.

4.3.2.2 Fourier Transform Infrared Spectroscopy (FT-IR)

Fig.4.18 shows the FT-IR transmittance curve of Au@Fe₃O₄/GO NCs S3 with sonication for 30 minutes.

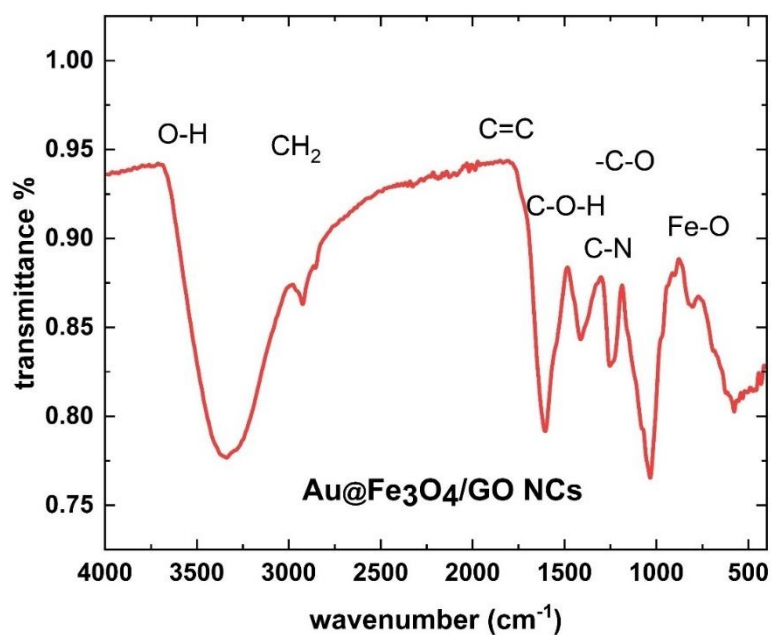


Figure 4.18: FT-IR spectra of the prepared Au@Fe₃O₄/GO NCs with sonication.

The FTIR spectrum provides insight into the functional groups present in the Au@Fe₃O₄/GO nanocomposites. The transmittance is plotted against wavenumber, ranging from 4000 to 500 cm⁻¹, revealing several characteristic peaks. O–H Stretching: A broad peak typically observed around 3400 cm⁻¹ indicates the presence of hydroxyl groups, suggesting surface-bound water functionalities. CH₂ Vibrations: Peaks in the region of ~2900 cm⁻¹ correspond to aliphatic C–H stretching, indicating organic residues or stabilizers which is gold nano particles [45]. C=C Stretching: The presence of a peak around ~1600 cm⁻¹ is characteristic of sp² hybridized carbon, confirming the graphitic nature of GO. C–O–H and C–N Groups: Peaks around ~1400–1300 cm⁻¹ suggest oxygen-containing functional groups. C–O Stretching: Observed near ~1100 cm⁻¹, this peak is typical of epoxy or ether groups on GO sheets. Fe–O Vibrations: A distinct peak below 600 cm⁻¹ confirms the presence of iron oxide (Fe₃O₄), validating successful decoration of GO with magnetic nanoparticles[70].

4.3.2.3 UV-Vis Absorption Spectra

The UV-Vis absorption spectra of the prepared NCs samples at different GO ratios were measured and given in Fig. 4.19. All curves follow a similar spectral shape, but with varying intensities, implying that the core structure of the nanocomposite remains consistent, and the changes are primarily due to GO concentration. Also The width of the absorption peak around 222 nm which assigned to the π – π^* transitions increased with no significant shift for S1, S2, S3 and S4. This is due to surface plasmon resonance effects from Au nanoparticles[71][72]. This also can be attributed to deoxygenation of the graphene oxide and formation of composite between the Fe₃O₄@Au nanoparticles and the graphene sheets under the synthesis reaction[45].

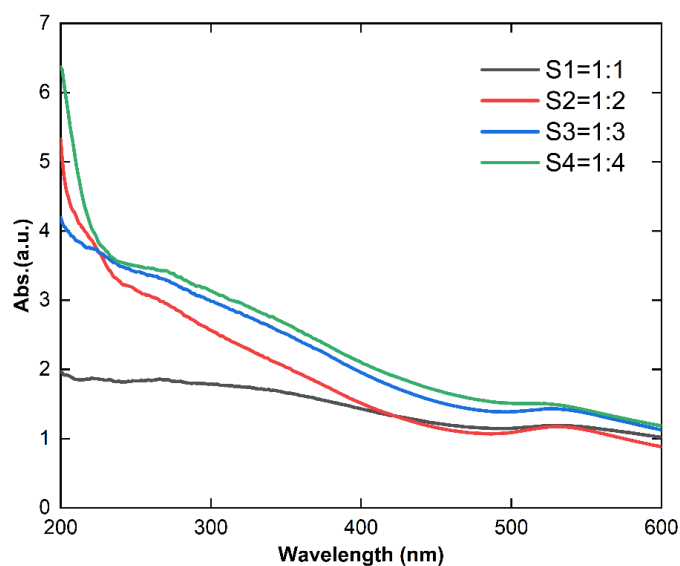


Figure 4.19: The absorption spectra of the prepared Au@Fe₃O₄/GO NCs at different GO concentration.

4.4 optical properties of GO, Fe₃O₄/GO and Au@Fe₃O₄/GO NCs

Fig. 4.20 represents the absorption spectra of GO, Fe₃O₄/GO and Au@Fe₃O₄/GO NCs. It reveals that the absorption of GO is enhanced by adding Fe₃O₄ due to its high absorption nature and more enhancement took place by adding Au@Fe₃O₄ due to the SPR of gold NPs.

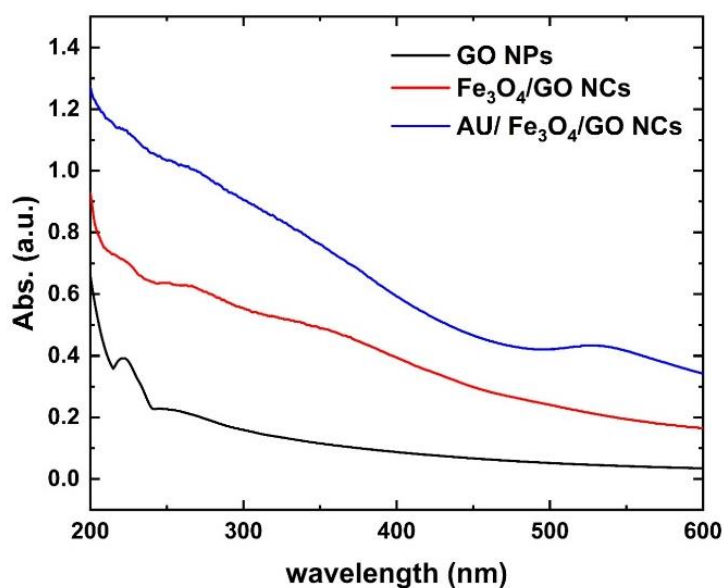


Figure 4.20 Absorption spectra of GO, Fe₃O₄/GO and Au@Fe₃O₄/GO NCs.

The absorption coefficient (α) of GO, Fe₃O₄/GO, and Au@Fe₃O₄/GO NCs can be obtained by using the following expression [73] :

$$\alpha = 2.303A/t \quad (4-2)$$

Where, A is the absorbance (unitless), t is the thickness of the sample (in cm). α was calculated and given in Fig.4.21 a). It shows that the decorated GO nanosheets have a much higher optical absorption coefficient than pure GO nanosheets, which indicates the high absorption nature of the nano Fe₃O₄ and Au@Fe₃O₄.

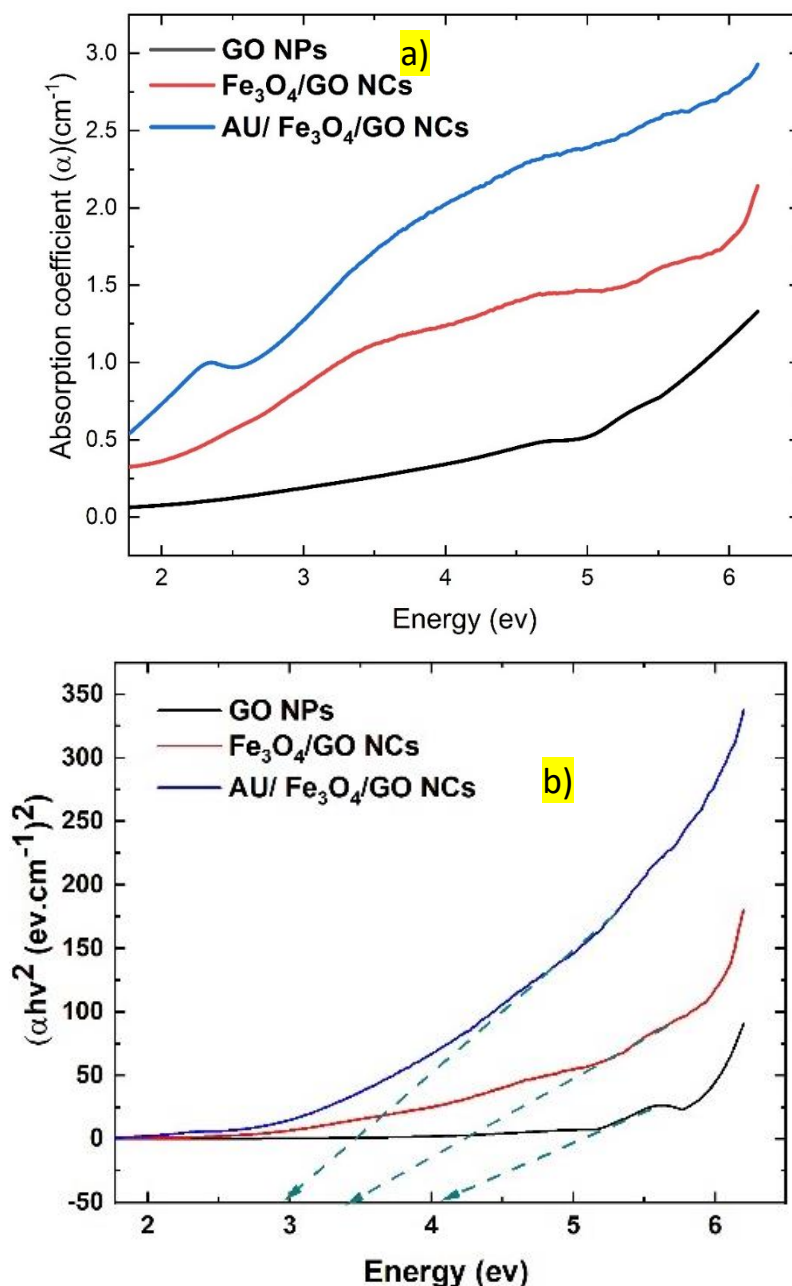


Figure 4.21, a) Absorption coefficient curve of GO, Fe₃O₄/GO and Au@ Fe₃O₄/GO NCs. b) Variation of $(\alpha h\nu)^2$ with the photon energy ($h\nu$) of GO, Fe₃O₄/GO and Au@Fe₃O₄/GO NCs.

Plotting $(\alpha h\nu)^2$ against photon energy ($h\nu$) for all the samples is displayed in Fig.4.21b. The values of E_g for GO, Fe₃O₄/GO, and Au@Fe₃O₄/GO NCs are 4.1 eV, 3.4 eV, and 3 eV, respectively. The presence of different oxidation states of iron in the magnetite (Fe²⁺ and Fe³⁺) could also introduce specific impurity states, particularly in the electronic structure of the

material, altering the conductivity or introducing new energy levels within the band gap[74]. Also, interaction between the graphene oxide, magnetite and gold could lead to charge transfer between the three materials, creating localized states in the graphene's conduction or valence bands[67]. The iron atoms in magnetite can also interact with the carbon atoms in graphene, leading to hybridized electronic states at the interface, which could behave as impurity states[59]. Because of this, the doped material's bandgap energy narrows, and it absorbs photons with bandgap energies between 3 and 4.1 eV, which causes more excited electrons to remain inside the doped sheets' conduction band. Urbach energy is calculated by the following equation[42][75]:

$$\ln\alpha = \ln\alpha_o + \frac{hv}{E_U} \quad (4-3)$$

α_o is a constant and E_U is the band tail width (Urbach energy) of the localized states in the optical energy gap. We have determined the E_U by calculating the equation's inverse slope. Table 1 tabulates the value of the band tailing. The relation between E_g and E_U is shown in Fig.4.22 for the three samples. It is clearly observed that by the addition of nanoparticles to GO sheets, the weak bonds of oxygen are replaced by decorating material. Increasing in the E_U value ashore that a broadening in localized states in the forbidden gap led to a decrement in it[46].

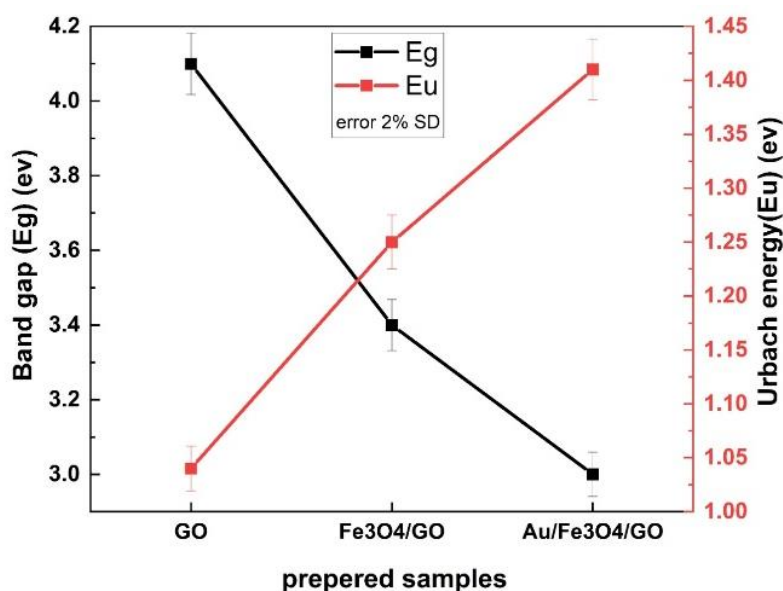


Figure4.22: Variation of the optical band gap (E_g) and Urbach energy (E_U) of GO, Fe₃O₄/GO and Au@ Fe₃O₄/GO NCs.

The steepness parameter (σ_s), which quantifies the sharpness or broadening of the Urbach tail, can be calculated empirically using this equation[76][46]:

$$\sigma_s = \frac{K_B T}{E_U} \quad (4-4)$$

We define k_B as the Boltzmann constant and T as the absolute temperature. Furthermore, σ_s determines how strongly the electron-phonon interacts (E_{e-p}), and they related to one another by the relationship[57]:

$$E_{e-p} = \frac{2}{3\sigma_s} \quad (4-5)$$

The σ_s and E_{e-p} values were calculated using equations (4) and (5), respectively, and tabulated in Table 1. The plot of the three prepared samples versus the three prepared samples is shown in Fig.4.23. A higher steepness parameter indicates a narrower Urbach tail and a sharper absorption edge, while a lower value signifies a broader tail and that was observed, suggesting a greater influence of electron-phonon interactions within the material.

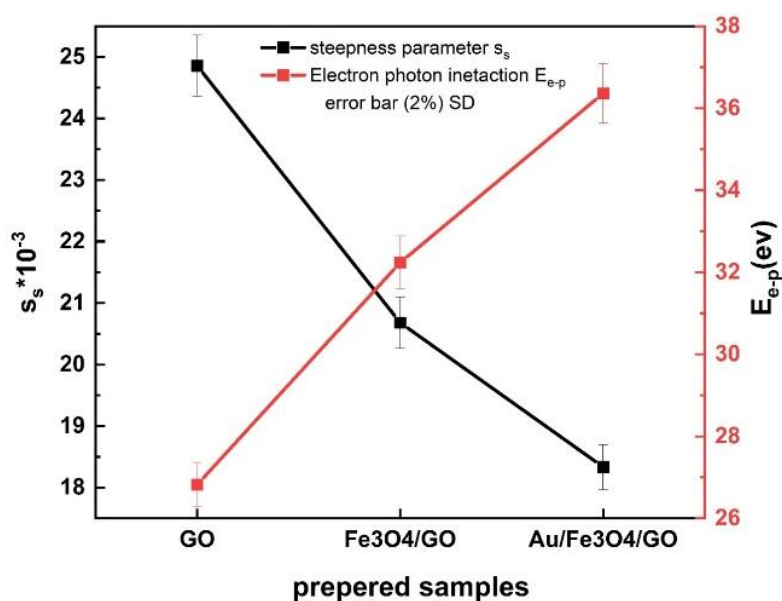


Figure 4.23: Variation of both steepness parameter (σ_s) and electron-phonon interaction (E_{e-p}) of GO, Fe₃O₄/GO and Au@Fe₃O₄/GO NCs.

A higher steepness parameter indicates a narrower Urbach tail and a sharper absorption edge, while a lower value signifies a broader tail and that was observed[77], suggesting a greater influence of electron-phonon interactions within the material and that is why the α_s decreases as the E_{e-p} increases. The total electronegativity difference ($\Delta\chi$) is an important parameter to

understand the chemical bonding. You can obtain the value of it by substituting the value of E_g into the Duffy relation [57]:

$$\Delta X = 0.2688E_g \quad (4-6)$$

Where $(\Delta\chi)$ value decreased from 1.04 to 0.806 as calculated in table 1. that is due to the direct relation between electronegativity and bandgap. Finding the refractive indices of materials is crucial, particularly for those that can be utilized to make any kind of optical device, such as switches, filters, modulation, etc. Many relations are presented between the refractive index (n) , (E_g) and $(\Delta\chi)$ shown in the following relations[46][78]:

$$n = -\ln(0.027E_g) \quad (4-7)$$

$$n = \sqrt{\left(\sqrt[6]{\frac{5}{E_g}} - 2\right)} \quad (4-8)$$

$$n = -\ln(0.102\Delta X) \quad (4-9)$$

Table 1 contains the calculated values for the refractive index (n) . The value of ΔX decreased from 1.102 to 0.806. The average refractive index (n_{avg}) was increased that assures the inverse proportional relation between E_g and n . Also, materials with small n are transparent in the visible region where the sample's colour becomes gradually darker.

Table 1-4: Bandgap (E_g), Urbach energy (E_u), electronegativity (ΔX), refractive index (n), steepness parameter (σ_s), electron phonon interaction (E_{e-p}) of GO, Fe_3O_4/GO and $Au@Fe_3O_4/GO$ NC respectively.

parameter	E_g (ev)	E_u (ev)	ΔX	Equation (n)			Average(n) (n_{avg})	σ_s	E_{e-p}
				Eq (6)	Eq (7)	Eq (8)			
Samples									
GO	4.1	1.04	1.102	2.2	2.15	2.18	2.17	24.8	26.8
Fe_3O_4/GO	3.4	1.25	0.913	2.38	2.29	2.37	2.39	20.6	32.2
$Au@Fe_3O_4/GO$	3	1.41	0.806	2.51	2.39	2.49	2.46	18.33	36.3

The optical response is studied for the samples in terms of optical conductivity calculated using the following relation:[46]

$$\sigma = \frac{\alpha nc}{4\pi} \quad (4-10)$$

Since (c) is the speed of light in vacuum, Fig.4.24 gives optical conductivity as a function of the photon energy.

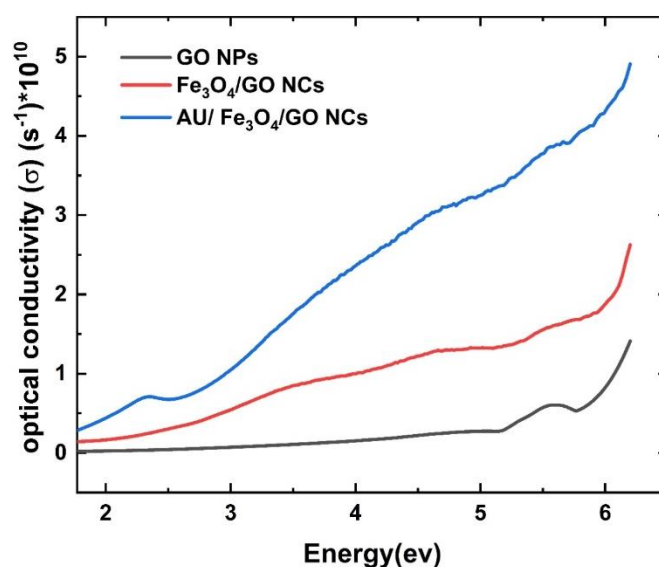


Figure 4.24: Optical conductivity spectrum of GO, Fe₃O₄/GO and Au@Fe₃O₄/GO NC.

The optical conductivity is higher at larger photon energy due to higher electron excitation at this energy, and the conductivity of decorated GO sheets is higher than pure GO sheets, which reveals the high photo-response. Using the values of n_{avg} obtained in Table 1, the electronic polarizability a fundamental optical parameter describing how the electron cloud of an atom or molecule distorts in response to an electric field. It can be calculated by using in the following equation:[79][80]

$$\alpha_e = \frac{3(n_{avg}^2 - 1)}{4\pi N_A(n_{avg}^2 + 2)} \quad (4-11)$$

Its value was increased, which reveals more response of the induced dipole moment and the applied electric field in the decorated graphene oxide sheets. V_m which is the molar volume, can be evaluated by the electronic polarizability (α_e) and by substitution in the following relation:[81]

$$\alpha_e = 0.395 \left(\frac{n_{\text{avg}}^2 - 1}{n_{\text{avg}}^2 + 1} \right) V_m \quad (4-12)$$

R_m is the molar refraction, which calculated based on the value of the average refractive index and molar volume by the Volf and Lorentz-Lorenz formula: [5][6]

$$R_m = \left(\frac{n_{\text{avg}}^2 - 1}{n_{\text{avg}}^2 + 1} \right) V_m \quad (4-13)$$

α_{me} is the molar electronic polarizability which used to understand how substances respond to electric fields and how this affects their optical and dielectric characteristics. Which can be calculated by: [44]

$$\alpha_{me} = \frac{R_m}{2.52} \quad (4-14)$$

The value of α_{me} increased for Fe₃O₄/GO and Au@Fe₃O₄/GO NCs due to strong SPR. The obtained values of (α_e), (V_m), (R_m) and (α_{me}) are present in Table2.

Table 4-2: Electronic polarizability (α_e), molar volume (v_m), molar refraction (R_m) and molar electronic polarizability (α_{me}) of GO, Fe₃O₄/GO and Au@Fe₃O₄/GO NCs respectively.

parameters	$\alpha_e * 10^{-25}$	$V_m * 10^{-25}$	$R_m * 10^{-25}$	$\alpha_{em} * 10^{-25}$
Samples				
GO	2.20	8.55	4.75	1.88
Fe₃O₄/GO	2.38	8.71	4.83	1.92
Au@ Fe₃O₄/GO	2.49	8.80	4.89	1.94

It's clearly seen that by the addition of Fe₃O₄ NPs and Au@Fe₃O₄ NCs, the electronic polarizability increased. There is a general thought by which the electronic polarizability of samples containing oxide ion increases with increasing refractive index and decreasing energy gap [82]. The (V_m), (R_m), and (α_{me}) are proportionally related to (α_e), so they also increased.

4.5 Thermal properties of GO, Fe₃O₄/ GO and Au@Fe₃O₄/ GO NCs.

As mentioned in chapter 2 the thermal diffusivity (α), thermal effusivity (e) and thermal conductivity (k) can be determined using the analysis of Poult and Chambron for thermally thick samples [37]. In the photoacoustic (PA) measurements, both the amplitude (q) and phase (ϕ) responses of the samples were recorded as functions of the modulation frequency. The relationship between the phase angle and frequency was plotted, and the experimental data were fitted according to the theoretical model described in Chapter 2 (Eqs.2-12 and 2-13). The value of optical absorption coefficient (β) was first obtained from the optical analysis at the wavelength of 450 nm (which corresponds to the laser source used in the PA technique) to be 0.161, 0.691 and 1.2 cm⁻¹ for GO, Fe₃O₄/GO and Au@Fe₃O₄/GO NCs respectively. Using these values of β , the thermal diffusivity (α) of the samples was calculated from the slope of the linear plots of $\tan(\phi) - 1$ versus (f)^{1/2}, as shown in Fig. 4-25 (a–c). The obtained values of α for pure water, GO, Fe₃O₄/GO and Au@Fe₃O₄/GO NC are given in Table 4.2. It can be seen that the values of α of GO is about 1.21 x 10⁻⁷ m²/s increase to 1.85 x 10⁻⁷ m²/s for Fe₃O₄/GO. Such an increase in the diffusivity is in reasonable agreement with the results of other authors[48][83]. For Au/Fe₃O₄/GO NC the value of α increase to about 140 % than that of Fe₃O₄/GO.

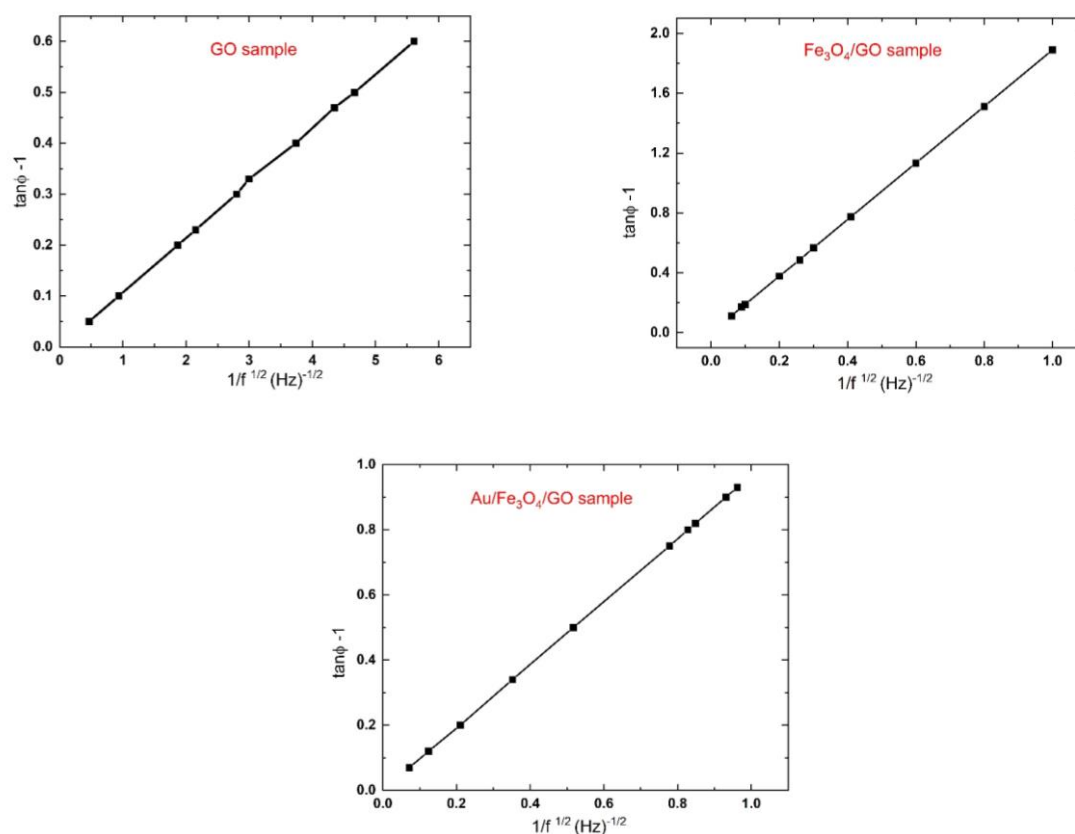


Figure 4.25: $\tan\phi - 1$ with $f^{-1/2}$ of a) GO, b) $\text{Fe}_3\text{O}_4/\text{GO}$ and c) $\text{Au}/\text{Fe}_3\text{O}_4/\text{GO}$ NC.

The thermal effusivity values of the samples were estimated by fitting the experimental results according to equation (2-13). The relation of (q) versus (f) is given in fig.4.26 a), b) and c) for GO, $\text{Fe}_3\text{O}_4/\text{GO}$ and $\text{Au}/\text{Fe}_3\text{O}_4/\text{GO}$ NCs respectively. The reference sample is methyl orange of known thermal parameters used in each case[84]. Again, there is an increase of the value of e by from $1.7 \times 10^3 \text{ ws}^{1/2}\text{m}^{-2}\text{k}^{-1}$ for $\text{Fe}_3\text{O}_4/\text{GO}$. To $1.85 \times 10^3 \text{ ws}^{1/2}\text{m}^{-2}\text{k}^{-1}$ for $\text{Au}/\text{Fe}_3\text{O}_4/\text{GO}$ NCs.

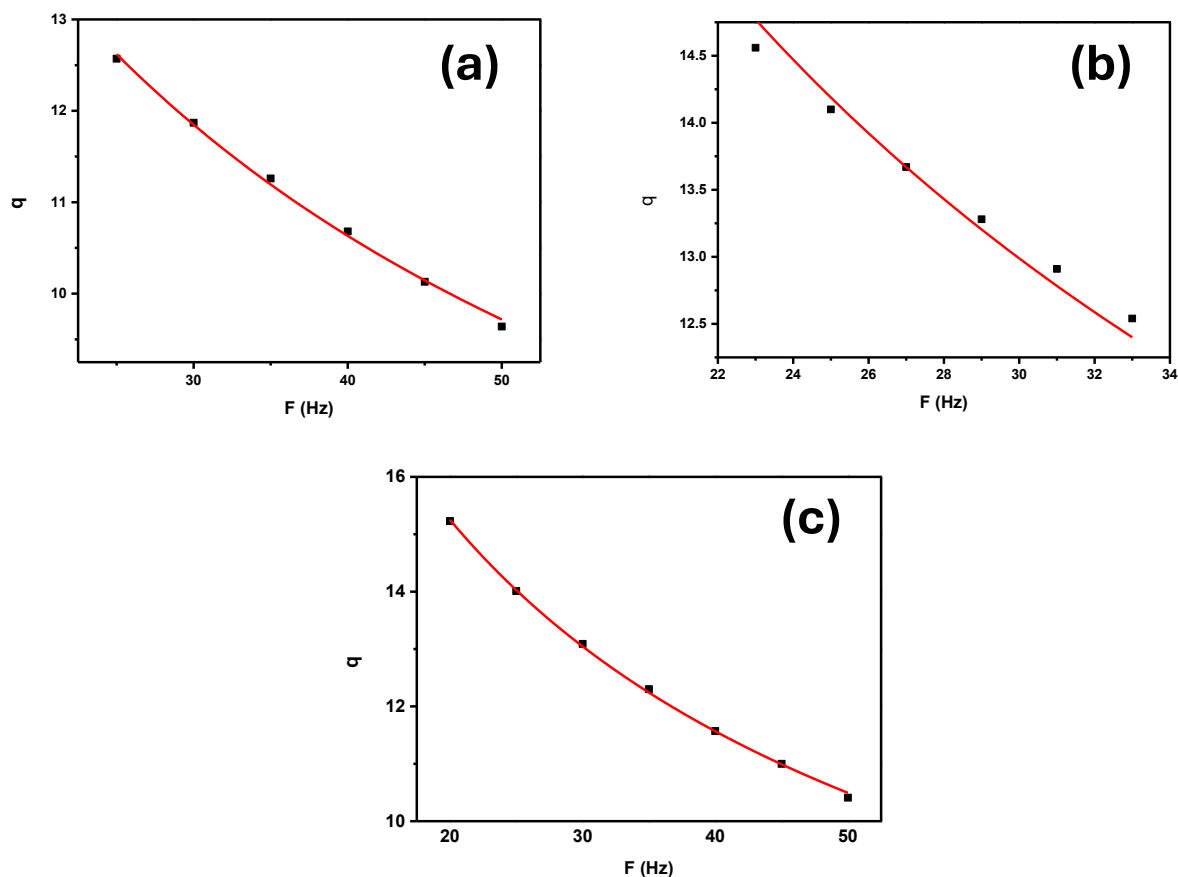


Figure 4.26: PA amplitude q versus frequency f of a) GO, b) $\text{Fe}_3\text{O}_4/\text{GO}$ and c) $\text{Au@Fe}_3\text{O}_4/\text{GO}$ NC.

The corresponding values of k ($= e\sqrt{\alpha}$) are calculated and displayed in Table 4.2. It can be seen that the values of k for GO is 0.3 increased to 1.2 W/m K when Fe_3O_4 is added to GO, which is very close to the reported value of k for [85]. This value increased to 2.5 W/m K for $\text{Au@Fe}_3\text{O}_4/\text{GO}$ NCs which is an enhancement of about 800% from that of GO.

Table4- 3: thermal diffusivity (α_t), thermal effusivity (e) and conductivity (k) of pure water as reference, GO, $\text{Fe}_3\text{O}_4/\text{GO}$ and $\text{Au@Fe}_3\text{O}_4/\text{GO}$ NC respectively.

parameters	Diffusivity ($\text{m}^2/\text{s}) \cdot 10^{-7}$	Effusivity ($\text{ws}^{1/2}\text{m}^{-2}\text{k}^{-1}) \cdot 10^3$	Conductivity ($\text{w m}^{-1}\text{k}^{-1}$)
samples			
Pure water	0.144	1.63	0.6
GO	0.121	1.55	0.3
$\text{Fe}_3\text{O}_4/\text{GO}$	0.185	1.70	1.2
$\text{Au/Fe}_3\text{O}_4/\text{GO}$	0.26	1.85	2.5

The conduction of heat in nanofluid may be considered as the propagation of a harmonic elastic waves through a continuum and propagation occurs via interaction of the quanta of thermal energy called “phonons”. In this case, the thermal conductivity, k , is given by [83]:

$$\alpha = k/\rho c$$

Where C is the specific heat capacity per unit volume and ρ is the density. The value of α depending on k and ρc in a different manner. However, the variations of ρc versus NPs content are weak, consequently, the effect of NPs on α is coming mainly from their effect on k . The significant increases of thermophysical (α , e , k) properties by adding Fe_3O_4 and Au were predicted. The presence of a phase with high thermal conductivity, which results in increase of the heat flow leads to an increase in the thermophysical properties of the alloyed sample. Furthermore, The value of α , e and k of $\text{Fe}_3\text{O}_4/\text{GO}$ and $\text{Au}@Fe_3O_4/\text{GO}$ are higher than of GO that is because GO contains oxygen groups that disrupt the pristine graphene lattice, These defects scatter phonons, which are the main carriers of heat, reducing thermal transport efficiency[86].the overall thermal properties of GO are also influenced by its oxidation degree, which limits the phonon mean free path and decreases thermal conductivity[87].

4.5.1 Thermal properties of $\text{Au}@Fe_3O_4/\text{GO}$ NCs with different ratios of GO.

The plot $\tan \phi - 1$ versus $(1/f)^{1/2}$ are shown in Fig 4.27 (a-d) for $\text{Au}@Fe_3O_4/\text{GO}$ with different ratios of GO. Given that the value of $\beta = 1.2, 2.505, 3.23$ and 4.79 cm^{-1} at the four ratios respectively at wave length 450 nm. The values of α is directly obtained from the slope of solid line which is the best fit for the experimental data and displayed in table 4-4. The results show that the value of α decreased from $0.26 \times 10^{-7} \text{ m}^2/\text{s}$ to $0.11 \times 10^{-7} \text{ m}^2/\text{s}$ as the ratio of GO increased.

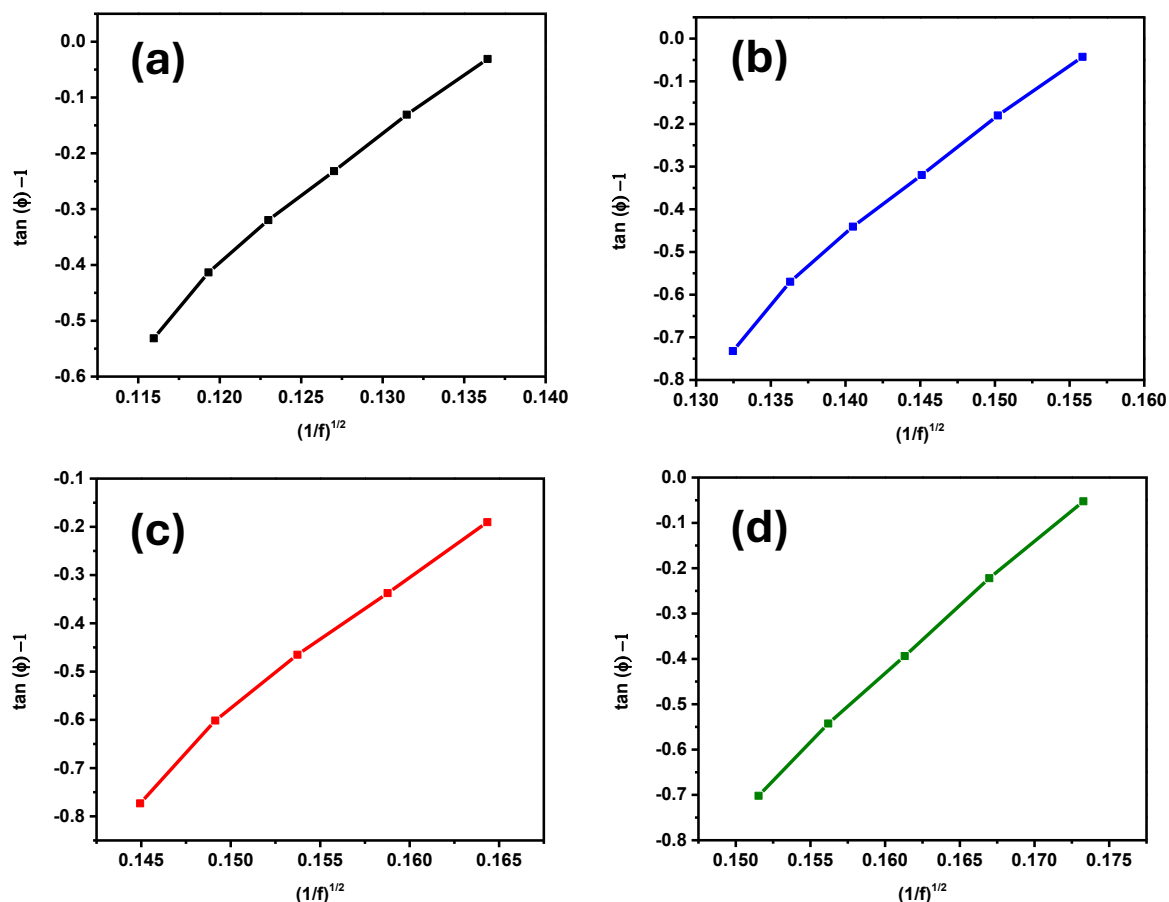


Figure 4.27: The plot between $[\tan(\phi)-1]$ with $(\frac{1}{f})^{1/2}$ for (a) S1=1:1, (b) S2=1:2 (c) S3=1:3 and (d) S4=1:4 .

The relation of (q) versus (f) are shown in Fig. 4.28 a, b, c, and d for Au@Fe₃O₄: GO ratios (1:1, 1:2, 1:3 and 1:4). The effusivity (e) can be obtained for each sample from Fig. 4.28 by using the best fitting of the experimental results according to equ.2-17. The calculated values of e are displayed in table 4-4. The results show that the values of e decrease from 1.85×10^3 to $1.17 \times 10^3 \text{ Ws}^{1/2}/\text{m}^2 \text{ K}^{-1}$ as the ratio of GO increases. The corresponding values of thermal conductivity $k (= e\sqrt{\alpha})$ are also tabulated in Table 4.4.

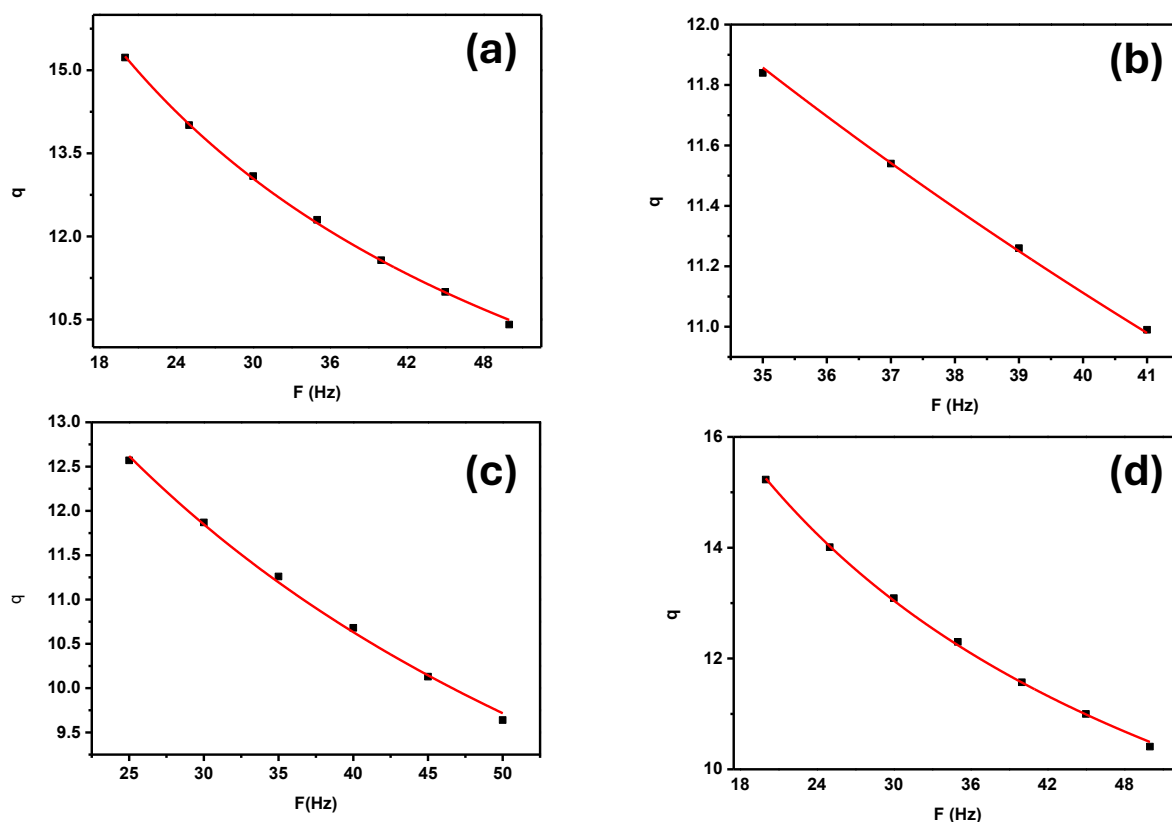


Figure 4.28 : PA Signal Vs chopper frequency for (a) S1, (b) S2 (c) S3 (d) S3.

Table 4- 4 Thermal diffusivity (α), thermal effusivity (e) and conductivity (k) Au@Fe₃O₄/GO NC with different concentration of Go respectively.

parameters			
Go concentration wt %	Diffusivity (m^2/s)* 10^{-7}	Effusivity ($ws^{1/2}m^{-2}k^{-1}$) $\times 10^3$	Conductivity ($w m^{-1}k^{-1}$)
0.05	0.33	2.3	2.88
0.10	0.3	2	2.8
0.15	0.28	1.9	2.68
0.20	0.26	1.85	2.5

It is clearly seen there is again decrease in k with increasing GO ratio. The value of k is 2.88 W/mK. While, upon increasing the amount of GO (S4) in heterostructure the k value decreased to 2.5 W/mK as illustrated in Table 4.4. Therefore, the significant decrease of composite thermophysical properties by adding a small amount of GO were predicted. Incorporation of

GO into the Au@Fe₃O₄/GO NC is accompanied by two effects influencing heat transport in the composite. The first one is the appearance of a surface of a new phase increase the number of interfaces, which increase of phonon scattering reduce the heat flow transport, thus resulting in an interfacial resistance. The second effect is the presence of a volume of a new phase with low thermal conductivity, which results a decrease of the heat flow. Our results showed that, the two effect became predominant.

5. Conclusion and future work

5.1 Conclusion

This study highlights the successful synthesis and characterization of ultrapure nanoparticle solutions using pulsed laser ablation in liquid (PLAL), a one-step, green, and highly effective technique.

We succeeded in preparing graphene oxide (GO) nanosheets using PLAL. HRTEM images show there are nanographene oxide sheets as a primary product and graphene quantum dots as a secondary product. FT-IR verified the presence of GO distinctive bonds.

The optical absorption spectra show an absorption edges at 222 nm and 265nm corresponding to π - π^* and n - π^* transitions respectively. The optical band gap of GO calculated to be 4.1 eV.

Magnetite (Fe_3O_4) was loaded on GO by the same technique to form $\text{Fe}_3\text{O}_4/\text{GO}$ NCs. HRTEM images show that the Fe_3O_4 NPs are uniformly distributed on GO sheets, which confirm the successful decoration process. FT-IR verified the presence of Fe_3O_4 bonds present below 600 cm^{-1} .

The optical absorption spectra show a broad absorption band from 300 to 400 nm due to Fe_3O_4 bimetallic nature, where the π - π^* and n - π^* transitions peaks width increased confirming the electronic structure change and NCs formation. The band gap of the NCs decreased to 3.5 eV as compared to GO.

$\text{Au}@/\text{Fe}_3\text{O}_4/\text{GO}$ NCs was prepared by the same technique. HRTEM images show after 30 of sonication the NCs is completely homogeneously dispersed in the GO sheet. FT-IR confirmed the presence of the $\text{Au}@/\text{Fe}_3\text{O}_4$ NCs beside GO bonds.

The optical absorption spectra show an increase in the absorption intensity as the percentage of GO increases. At 527 nm there is a distinguish peak of $\text{Au}@/\text{Fe}_3\text{O}_4$ NCs, where a widening in the peak at 222 nm was observed and this is due to the electronic structure change due to SPR effect of $\text{Au}@/\text{Fe}_3\text{O}_4$ NCs. The bandgap of $\text{Au}@/\text{Fe}_3\text{O}_4/\text{GO}$ NCs decreased to 3 eV as compared to GO.

$\text{Au}@/\text{Fe}_3\text{O}_4/\text{GO}$ NCs was prepared with different four GO ratios, where the $\text{Au}@/\text{Fe}_3\text{O}_4:\text{GO}$ changed as follow (S1=1:1, S2=1:2, S3=1:3 and S4=1:4).

Urbach energy was calculated, showing an inverse relationship with band gap, and the steepness parameter revealed a broadening of the Urbach tail upon addition of Fe₃O₄ and Au@Fe₃O₄, suggesting enhanced electron–phonon interactions.

Also, electronic polarizability (α_e) and molar electronic polarizability (α_{me}) were evaluated for GO, Fe₃O₄/GO, and Au@Fe₃O₄/GO nanocomposites, demonstrating improved responsiveness to magnetic and electric fields.

Furthermore, photoacoustic technique has been used to measure the thermal parameters (thermal diffusivity (α_t), thermal effusivity (e), and thermal conductivity (k)) for GO, Fe₃O₄/GO Au@Fe₃O₄/GO NCs. The results show there is an enhancement of α , e and k for Au@Fe₃O₄/GO NCs than that of GO and Fe₃O₄/GO, The increase of thermal properties NCs is due to the presence of a phase of high thermal parameters.

The thermal parameters of Au@Fe₃O₄/GO with different GO contents are also measured using PA technique. The results show there is a nearly 80% decrease in k up to S4. This decrease is due to the appearance of a surface of a new phase increase the number of interfaces, which increase of phonon scattering as well as the presence of a new phase with low thermal conductivity.

5.2 future work

The prepared nanoparticles will be used in specific application such as: water treatment, water desalination, cancer treatment and antibacterial reagent.

References

- [1] K. A. Altammar, "A review on nanoparticles : characteristics , synthesis , applications , and challenges," *Front. Microbiol.*, vol. 14, April, pp. 1–20, 2023, doi: 10.3389/fmicb.2023.1155622.
- [2] I. Chung, "KOREAN TEACHERS' PERCEPTIONS OF STUDENT SUCCESS IN MATHEMATICS: Concept versus procedure," *Math. Enthus.*, vol. 6, no. 1–2, pp. 239–256, 2009, doi: 10.54870/1551-3440.1147.
- [3] A. S. Mayorov *et al.*, "Micrometer-scale ballistic transport in encapsulated graphene at room temperature," *Nano Lett.*, vol. 11, no. 6, pp. 2396–2399, 2011, doi: 10.1021/nl200758b.
- [4] K. Kim, J. Y. Choi, T. Kim, S. H. Cho, and H. J. Chung, "A role for graphene in silicon-based semiconductor devices," *Nature*, vol. 479, no. 7373, pp. 338–344, 2011, doi: 10.1038/nature10680.
- [5] F. Xia, D. B. Farmer, Y. M. Lin, and P. Avouris, "Graphene field-effect transistors with high on/off current ratio and large transport band gap at room temperature," *Nano Lett.*, vol. 10, no. 2, pp. 715–718, 2010, doi: 10.1021/nl9039636.
- [6] F. Paquin, J. Rivnay, A. Salleo, N. Stingelin, and C. Silva, "Multi-phase semicrystalline microstructures drive exciton dissociation in neat plastic semiconductors," *J. Mater. Chem. C*, vol. 3, no. 207890, pp. 10715–10722, 2015, doi: 10.1039/b000000x.
- [7] G. Eda, C. Mattevi, H. Yamaguchi, H. Kim, and M. Chhowalla, "Insulator to semimetal transition in graphene oxide," *J. Phys. Chem. C*, vol. 113, no. 35, pp. 15768–15771, 2009, doi: 10.1021/jp9051402.
- [8] T. Gokus *et al.*, "Making graphene luminescent by oxygen plasma treatment," *ACS Nano*, vol. 3, no. 12, pp. 3963–3968, 2009, doi: 10.1021/nn9012753.
- [9] D. A. Dikin *et al.*, "Preparation and characterization of graphene oxide paper," *Nature*, vol. 448, no. 7152, pp. 457–460, 2007, doi: 10.1038/nature06016.
- [10] A. A. Menazea and M. K. Ahmed, "Synthesis and antibacterial activity of graphene oxide decorated by silver and copper oxide nanoparticles," *J. Mol. Struct.*, vol. 1218, p. 128536, 2020, doi: 10.1016/j.molstruc.2020.128536.
- [11] N. M. El-Shafai *et al.*, "Magnetite nano-spherical quantum dots decorated graphene oxide nano sheet (GO@Fe₃O₄): Electrochemical properties and applications for removal heavy metals, pesticide and solar cell," *Appl. Surf. Sci.*, vol. 506, no. October 2019, p. 144896, 2020, doi: 10.1016/j.apsusc.2019.144896.
- [12] A. G. Roca, J. F. Marco, P. Morales, and C. J. Serna, "Effect of Nature and Particle Size on Properties of Uniform Magnetite and Maghemite Nanoparticles Effect of Nature and Particle Size on Properties of Uniform Magnetite and Maghemite Nanoparticles," *Phys. Chem. C*, vol. 111, no. 50, pp. 18577–18584, 2007, doi: 10.1021/jp075133m.
- [13] A. S. Wasfi, H. R. Humud, and N. K. Fadhil, "Synthesis of core-shell Fe₃O₄-Au nanoparticles by electrical exploding wire technique combined with laser pulse

- shooting,” *Opt. Laser Technol.*, vol. 111, no. May 2018, pp. 720–726, 2019, doi: 10.1016/j.optlastec.2018.09.006.
- [14] F. Mafune, J. Kohno, Y. Takeda, and T. Kondow, “Formation and size control of silver nanoparticles by laser ablation in aqueous solution,” *Phys. Chem. B*, vol. 104, no. 39, pp. 9111–9117, 2000.
- [15] Z. Yan and D. B. Crissey, “Pulsed laser ablation in liquid for micro-/nanostructure generation,” *J. Photochem. Photobiol. C Photochem. Rev.*, vol. 13, no. 3, pp. 204–223, 2012, doi: 10.1016/j.jphotochemrev.2012.04.004.
- [16] G. K. Yogesh, E. P. Shuaib, P. Roopmani, M. B. Gumpu, U. M. Krishnan, and D. Sastikumar, “Synthesis, characterization and bioimaging application of laser-ablated graphene-oxide nanoparticles (nGOs),” *Diam. Relat. Mater.*, vol. 104, p. 107733, 2020, doi: 10.1016/j.diamond.2020.107733.
- [17] N. M. Dat *et al.*, “Synthesis of silver/reduced graphene oxide for antibacterial activity and catalytic reduction of organic dyes,” *Synth. Met.*, vol. 260, no. October 2019, p. 116260, 2020, doi: 10.1016/j.synthmet.2019.116260.
- [18] Z. Liu, J. T. Robinson, X. Sun, and H. Dai, “PEGylated Nanographene Oxide for Delivery of Water-Insoluble Cancer Drugs,” *Am. Chem. Soc.*, vol. 130, no. 33, pp. 10876–10877, 2008.
- [19] I. Diédhiou and S. Ben Aoun, “Simultaneous detection of trace Pb (II) and Cd (II) cations in ore samples by anodic stripping analysis using pMO / erGO-modified glassy carbon electrodes,” *Electroanalysis*, vol. 35, no. 12, p. e202300072, 2023, doi: 10.1002/elan.202300072.
- [20] N. M. El-Shafai *et al.*, “Magnetite nano-spherical quantum dots decorated graphene oxide nano sheet (GO@Fe₃O₄): Electrochemical properties and applications for removal heavy metals, pesticide and solar cell,” *Appl. Surf. Sci.*, vol. 506, Mar. 2020, doi: 10.1016/j.apsusc.2019.144896.
- [21] X. Yang, X. Zhang, Y. Ma, Y. Huang, and Y. Chen, “Superparamagnetic graphene oxide – Fe₃O₄ nanoparticles hybrid for controlled targeted drug carriers Superparamagnetic graphene oxide – Fe₃O₄ nanoparticles hybrid for controlled targeted drug carriers,” *Mater. Chem.*, vol. 19, no. 18, pp. 2710–2714, 2009, doi: 10.1039/B821416F.
- [22] L. Preserve and L. Blaney, “Magnetite (Fe₃O₄): Properties, Synthesis, and Applications,” *Lehigh Univ.*, vol. 15, p. 50, 2007, [Online]. Available: <http://preserve.lehigh.edu/cas-lehighreview-vol-15><http://preserve.lehigh.edu/cas-lehighreview-vol-15/5>
- [23] C. Ursino, R. Castro-muñoz, E. Drioli, M. H. Albeirutty, and A. Figoli, “Progress of Nanocomposite Membranes for Water Treatment,” *Membranes (Basel)*, vol. 8, no. 2, pp. 1–40, 2018, doi: 10.3390/membranes8020018.
- [24] M. Thangamuthu, K. Y. Hsieh, and P. V Kumar, “Graphene- and Graphene Oxide-Based Nanocomposite Platforms for Electrochemical Biosensing Applications,” *Mol. Sci.*, vol. 12, no. 20, p. 2975, 2019, doi: 10.3390/ijms20122975.
- [25] J. Hoffman *et al.*, “The effect of laser wavelength on the ablation rate of carbon,” *Appl. Phys. A Mater. Sci. Process.*, vol. 117, no. 1, pp. 395–400, 2014, doi: 10.1007/s00339-

014-8506-0.

- [26] B. Ashrafkhani, M. Bahreini, and S. H. Tavassoli, "Repeatability improvement of laser-induced breakdown spectroscopy using an auto-focus system," *Opt. Spectrosc. (English Transl. Opt. i Spektrosk.)*, vol. 118, no. 5, pp. 841–846, 2015, doi: 10.1134/S0030400X15050057.
- [27] A. Litavnieka, I. Adijāns, E. Yankov, L. Lazov, and A. Bikovs, "Investigation of the optimization process of laser surface marking on polyamide samples," *Vide. Tehnol. Resur. - Environ. Technol. Resour.*, vol. 3, pp. 413–418, 2024, doi: 10.17770/etr2024vol3.8168.
- [28] G. Z. Sakhvadze, L. V. Gavrilina, and O. G. Kikvidze, "Influence of laser spot overlap effect on residual stresses during laser-shock-wave processing of materials," *J. Mach. Manuf. Reliab.*, vol. 45, no. 3, pp. 258–265, 2016, doi: 10.3103/S1052618816030146.
- [29] V. A. Online, V. Amendola, and M. Meneghetti, "What controls the composition and the structure of nano- materials generated by laser ablation in liquid solution? †," *Phys. Chem. Chem. Phys.*, vol. 15, no. 9, pp. 3027–3046, 2013, doi: 10.1039/c2cp42895d.
- [30] A. Men, P. Wagener, and S. Barcikowski, "Transfer-Matrix Method for Efficient Ablation by Pulsed Laser Ablation and Nanoparticle Generation in Liquids," *Phys. Chem. C*, vol. 115, no. 12, pp. 5108–5114, 2011.
- [31] D. Perez, L. K. Béland, D. Deryng, L. J. Lewis, and M. Meunier, "Numerical study of the thermal ablation of wet solids by ultrashort laser pulses," *Condens. Matter Mater. Phys.*, vol. 77, no. 1, pp. 1–9, 2008, doi: 10.1103/PhysRevB.77.014108.
- [32] Z. Yan *et al.*, "Excimer Laser Production , Assembly , Sintering , and Fragmentation of Novel Fullerene-like Permalloy Particles in Liquid," *Phys. Chem. C*, vol. 114, no. 9, pp. 3869–3873, 2010.
- [33] R. Onsi, M. Nabil, S. Abdallah, and S. Negm, "Investigation of Thermophysical Properties of CuFeS₂ Nanoparticles Prepared by Pulsed Laser Ablation Technique .," vol. 46, no. 46, p. 15, 2024, doi: 10.21608/ejs.2024.323235.1052.
- [34] A. Rosencwaig and A. Gersho, "Theory of the photoacoustic effect with solids," *J. Appl. Phys.*, vol. 47, no. 1, pp. 64–69, 1976, doi: 10.1063/1.322296.
- [35] A. Rosencwaig, "Photoacoustic spectroscopy. New tool for investigation of solids," *Anal. Chem.*, vol. 47, no. 6, pp. 592A-604a., 1975.
- [36] A. Rosencwaig, "Photoacoustic spectroscopy.," *Annu. Rev. Biophys. Bioeng.*, vol. 9, pp. 31–54, 1980, doi: 10.1146/annurev.bb.09.060180.000335.
- [37] P. Poulet and J. Chambron, "Quantitative photoacoustic spectroscopy applied to thermally thick samples Quantitative photoacoustic spectroscopy applied to thermally thick samples," *Appl. Phys. A*, vol. 51, no. 3, pp. 1738–1742, 1980, doi: 10.1063/1.327785.
- [38] T. A. El-Brolossy and O. Saber, "Non-intrusive method for thermal properties measurement of nanofluids," *Exp. Therm. Fluid Sci.*, vol. 44, pp. 498–503, 2013, doi: 10.1016/j.expthermflusci.2012.08.011.
- [39] J. Oh *et al.*, "Energy-Dependent Spectral Analysis of Photon-Assisted Carrier Transport at Resonance in Graphene Oxide," *Adv. Opt. Mater.*, vol. 7, no. 5, pp. 1–8,

- 2019, doi: 10.1002/adom.201800861.
- [40] S. S. Fouad, I. M. El Radaf, P. Sharma, and M. S. El-bana, "Multifunctional CZTS thin films: Structural, optoelectrical, electrical and photovoltaic properties," *J. Alloys Compd.*, vol. 757, pp. 124–133, 2018, doi: 10.1016/j.jallcom.2018.05.033.
- [41] H. Zaka, B. Parditka, Z. Erdélyi, H. E. Atyia, P. Sharma, and S. S. Fouad, "Investigation of dispersion parameters, dielectric properties and opto-electrical parameters of ZnO thin film grown by ALD," *Optik (Stuttg.)*, vol. 203, 2020, doi: 10.1016/j.ijleo.2019.163933.
- [42] A. S. Hassanien and A. A. Akl, "Influence of composition on optical and dispersion parameters of thermally evaporated non-crystalline Cd₅₀S_{50-x}Se_x thin films," *J. Alloys Compd.*, vol. 648, pp. 280–290, Jul. 2015, doi: 10.1016/j.jallcom.2015.06.231.
- [43] S. Rajeshkumar, "Anticancer activity of eco-friendly gold nanoparticles against lung and liver cancer cells," *J. Genet. Eng. Biotechnol.*, vol. 14, no. 1, pp. 195–202, 2016, doi: 10.1016/j.jgeb.2016.05.007.
- [44] P. Hajipour, A. Bahrami, A. Eslami, A. Hosseini-Abari, and H. reza Hagh Ranjbar, "Chemical bath synthesis of CuO-GO-Ag nanocomposites with enhanced antibacterial properties," *J. Alloys Compd.*, vol. 821, p. 153456, 2020, doi: 10.1016/j.jallcom.2019.153456.
- [45] T. Shakerian Ardakani, A. Meidanchi, A. Shokri, and A. Shakeri-Zadeh, "Structural and optical properties of Fe₃O₄@Au/rGO nanocomposites synthesized by hydrothermal method and their photothermal effect under NIR laser irradiation," *Mater. Chem. Phys.*, vol. 258, p. 123956, 2021, doi: 10.1016/j.matchemphys.2020.123956.
- [46] M. Nabil, S. S. Fouad, K. Easawi, S. Abdallah, and H. F., "Novel correlations between optical absorption and water desalination of Ag/Fe₃O₄ nanocomposite prepared by pulsed laser ablation in liquid," *Opt. Laser Technol.*, vol. 164, no. April, 2023, doi: 10.1016/j.optlastec.2023.109545.
- [47] J. M. Jassim, M. S. Al-samak, W. T. Younes, and H. Kisov, "Near-Infrared Plasmonic Random Laser Emission Employing Gold Nanorods and LDS-821 Dye," *Plasmonics*, vol. 20, pp. 7657–7664, 2025, doi: 10.1007/s11468-025-02765-3.
- [48] T. L. Mon, N. Kamilah, S. Aziz, and S. M. Nazir, "Influence of Concentration of Graphene Oxide to Thermal Diffusivity in Nano-liquid Form Using Thermal Lens Method," vol. 35, no. 2, 2025.
- [49] Spectra-Physics, "Quanta-Ray® Nd:YAG Laser Family," 2014.
- [50] J. H. Grimes, "Introductory Training for Bruker Alpha II FTIR."
- [51] P. Russo, "Single-step synthesis of graphene quantum dots by femtosecond laser ablation of graphene oxide dispersions Paola," *Nanoscale*, vol. 8, no. 16, pp. 8863–8877, 2016, doi: 10.1039/C6NR01148A.
- [52] M. V. Reddy, T. Y. Aloysius Chan, and S. Adams, "Effect of molten salt synthesis temperature on TiO₂ and Li cycling properties," *J. Solid State Electrochem.*, vol. 22, no. 2, pp. 429–439, 2018, doi: 10.1007/s10008-017-3756-3.
- [53] G. Vinodha, L. Cindrella, V. Sithara, J. Philip, and P. D. Shima, "Synthesis,

- characterization, thermal conductivity and rheological studies in magnetite-decorated graphene oxide nanofluids,” *J. Nanofluids*, vol. 7, no. 1, pp. 11–20, 2018, doi: 10.1166/jon.2018.1435.
- [54] Z. Çiplak, N. Yildiz, and A. Çalimli, “Investigation of graphene/Ag nanocomposites synthesis parameters for two different synthesis methods,” *Fullerenes Nanotub. Carbon Nanostructures*, vol. 23, no. 4, pp. 361–370, 2015, doi: 10.1080/1536383X.2014.894025.
- [55] A. M. Dimiev, L. B. Alemany, and J. M. Tour, “Graphene Oxide . Origin of Acidity , Its Instability in Water , and a New Dynamic Structural Model,” *ACS Nano*, vol. 7, no. 1, pp. 576–588, 2013, doi: 10.1021/nn3047378.
- [56] G. Kumar, E. P. Shuaib, P. Roopmani, and M. Bhargavi, “Diamond & Related Materials Synthesis , characterization and bioimaging application of laser-ablated graphene-oxide nanoparticles (nGOs),” vol. 104, no. January, 2020.
- [57] M. Nabil, H. F. S. S. Fouad, and S. Negm, “Impact of Au nanoparticles on the thermophysical parameters of Fe₃O₄ nanoparticles for seawater desalination,” *Opt. Mater. (Amst.)*, vol. 128, no. April, p. 112456, 2022, doi: 10.1016/j.optmat.2022.112456.
- [58] F. Horia, K. Easawi, R. Khalil, S. Abdallah, M. El-Mansy, and S. Negm, “Optical and Thermophysical Characterization of Fe₃O₄nanoparticle,” in *IOP Conference Series: Materials Science and Engineering*, IOP Publishing Ltd, Oct. 2020. doi: 10.1088/1757-899X/956/1/012016.
- [59] N. M. El-Shafai, M. E. El-Khouly, M. El-Kemary, M. S. Ramadan, and M. S. Masoud, “Graphene oxide-metal oxide nanocomposites: Fabrication, characterization and removal of cationic rhodamine B dye,” *RSC Adv.*, vol. 8, no. 24, pp. 13323–13332, 2018, doi: 10.1039/c8ra00977e.
- [60] E. B.G. *et al.*, “Blue Photoluminescence from Chemically Derived Graphene Oxide. Advanced Materials,” *Phyl. Trans. R. Soc. London A*, vol. 22, pp. 505–509, 2010.
- [61] M. Asadi, H. Sereshti, and H. Rashidi, “Development of magnetic dispersive microsolid - phase extraction using lanthanum phosphate nanoparticles doped on magnetic graphene oxide as a highly selective adsorbent for pesticide residues analysis in water and fruit samples,” *Res. Chem. Intermed.*, vol. 46, no. 5, pp. 2789–2803, 2020, doi: 10.1007/s11164-020-04121-y.
- [62] F. Horia, K. Easawi, R. Khalil, S. Abdallah, M. El-Mansy, and S. Negm, “Optical and Thermophysical Characterization of Fe₃O₄nanoparticle,” *IOP Conf. Ser. Mater. Sci. Eng.*, vol. 956, no. 1, pp. 0–9, 2020, doi: 10.1088/1757-899X/956/1/012016.
- [63] X. Luo *et al.*, “Laser-Ablated Vortex Fluidic-Mediated Synthesis of Superparamagnetic Magnetite Nanoparticles in Water under Flow,” *ACS Omega*, vol. 3, no. 9, pp. 11172–11178, 2018, doi: 10.1021/acsomega.8b01606.
- [64] F. F. H. Aragón *et al.*, “Evidence of progressive Fe²⁺ to Fe³⁺oxidation in Fe²⁺-doped ZnO nanoparticles,” *Mater. Adv.*, vol. 4, no. 5, pp. 1389–1402, 2023, doi: 10.1039/d3ma00053b.
- [65] N. Barnawi, S. Allehyani, and R. Seoudi, “Biosynthesis and characterization of gold nanoparticles and its application in eliminating nickel from water,” 2022. doi:

10.1016/j.jmrt.2021.12.013.

- [66] K. S. Siddiqi, A. ur Rahman, Tajuddin, and A. Husen, "Biogenic Fabrication of Iron/Iron Oxide Nanoparticles and Their Application," *Nanoscale Res. Lett.*, vol. 11, no. 1, pp. 0–13, 2016, doi: 10.1186/s11671-016-1714-0.
- [67] R. J. Chung and H. T. Shih, "Preparation of multifunctional Fe@Au core-shell nanoparticles with surface grafting as a potential treatment for magnetic hyperthermia," *Materials (Basel)*, vol. 7, no. 2, pp. 653–661, 2014, doi: 10.3390/ma7020653.
- [68] C. W. Lin *et al.*, "Magneto-Optical Characteristics of Streptavidin-Coated Fe₃O₄@Au Core-Shell Nanoparticles for Potential Applications on Biomedical Assays," *Sci. Rep.*, vol. 9, no. 1, pp. 1–8, 2019, doi: 10.1038/s41598-019-52773-7.
- [69] A. Pradhan, R. C. Jones, D. Caruntu, C. J. O. Connor, and M. A. Tarr, "Gold – magnetite nanocomposite materials formed via sonochemical methods," vol. 15, pp. 891–897, 2008, doi: 10.1016/j.ultsonch.2008.01.004.
- [70] Y. Yuan *et al.*, "Hydrothermal preparation of Fe₂O₃/graphene nanocomposite and its enhanced catalytic activity on the thermal decomposition of ammonium perchlorate," *Appl. Surf. Sci.*, vol. 303, pp. 354–359, 2014, doi: 10.1016/j.apsusc.2014.03.005.
- [71] A. Kovtun, D. Jones, S. Dell'Elce, E. Treossi, A. Liscio, and V. Palermo, "Accurate chemical analysis of oxygenated graphene-based materials using X-ray photoelectron spectroscopy," *Carbon N. Y.*, vol. 143, pp. 268–275, 2019, doi: 10.1016/j.carbon.2018.11.012.
- [72] T. Tene *et al.*, "Optical properties of graphene oxide," *Front. Chem.*, vol. 11, no. July, pp. 1–14, 2023, doi: 10.3389/fchem.2023.1214072.
- [73] S. S. Fouad, M. Nabil, B. Parditka, and S. Negm, "Microstructural and optical duality of TiO₂/Cu/TiO₂ trilayer films grown by atomic layer deposition and DC magnetron sputtering," *Inorg. Chem. Commun.*, vol. 145, p. 110017, 2022, doi: <https://doi.org/10.1016/j.inoche.2022.110017>.
- [74] A. D. Rowan, C. H. Patterson, and L. V. Gasparov, "Hybrid density functional theory applied to magnetite: Crystal structure, charge order, and phonons," *Phys. Rev. B - Condens. Matter Mater. Phys.*, vol. 79, no. 20, 2009, doi: 10.1103/PhysRevB.79.205103.
- [75] M. H. Mamat, M. Z. Sahdan, S. Amizam, and H. A. Rifaie, "Optical and electrical properties of aluminum doped zinc oxide thin films at various doping concentrations," *Ceram. Soc. Japan*, vol. 117, no. 1371, pp. 1263–1267, 2009.
- [76] Z. El-Qahtani, A. Badawi, K. Easawi, N. Al-Hosiny, and S. Abdallah, "Photoacoustic study of optical and thermal properties of alloyed CdTe_xS_{1-x} nanocrystals," *Mater. Sci. Semicond. Process.*, vol. 20, no. 1, pp. 68–73, 2014, doi: 10.1016/j.mssp.2013.12.034.
- [77] G. V. Makhnovets, G. L. Myronchuk, L. V. Piskach, B. V. Vidrynskyi, and A. H. Kevshyn, "Study of optical absorption in TlGaSe₂:Zn²⁺ single crystals," *Ukr. J. Phys. Opt.*, vol. 19, no. 1, pp. 49–59, 2018, doi: 10.3116/16091833/19/1/49/2018.
- [78] M. Nabil, F. Horia, S. S. Fouad, and S. Negm, "Impact of Au nanoparticles on the

- thermophysical parameters of Fe₃O₄ nanoparticles for seawater desalination,” *Opt. Mater. (Amst.)*, vol. 128, no. May, p. 112456, 2022, doi: 10.1016/j.optmat.2022.112456.
- [79] S. A. Umar, M. K. Halimah, K. T. Chan, and A. A. Latif, “Polarizability, optical basicity and electric susceptibility of Er³⁺ doped silicate borotellurite glasses,” *J. Non. Cryst. Solids*, vol. 471, no. March, pp. 101–109, 2017, doi: 10.1016/j.jnoncrysol.2017.05.018.
- [80] V. Dimitrov and T. Komatsu, “AN INTERPRETATION OF OPTICAL PROPERTIES OF OXIDES AND OXIDE GLASSES IN TERMS OF THE ELECTRONIC ION POLARIZABILITY AND AVERAGE SINGLE BOND STRENGTH,” *J. Univ. Chem. Technol. Met.*, vol. 45, no. 3, pp. 219–250, 2010.
- [81] A. Hellal, H. Abdelsalam, W. Tawfik, and M. A. Ibrahim, “Assessment of doped graphene in the removal of atrazine from water,” *Sci. Rep.*, vol. 14, no. 1, pp. 1–17, 2024, doi: 10.1038/s41598-024-71886-2.
- [82] V. Dimitrov and T. Komatsu, “Electronic polarizability, optical basicity and non-linear optical properties of oxide glasses,” *J. Non. Cryst. Solids*, vol. 249, no. 2–3, pp. 160–179, 1999, doi: 10.1016/S0022-3093(99)00317-8.
- [83] M. Rafi, R. Lakshmi, H. John, and P. Gopinath, “Investigating thermal diffusivity in magnetite – graphene oxide nanoscrolls,” *Opt. Commun.*, vol. 592, no. March 2024, p. 132252, 2025, doi: 10.1016/j.optcom.2025.132252.
- [84] L. Hui and D. G. Leaist, “Thermal diffusion with stepwise association equilibria in aqueous solutions of the ionic dyes methylene blue and methyl orange,” *J. Solution Chem.*, vol. 19, no. 4, pp. 391–399, 1990, doi: 10.1007/BF00648143.
- [85] M. Hadadian, E. K. Goharshadi, and A. Youssefi, “Electrical conductivity, thermal conductivity, and rheological properties of graphene oxide-based nanofluids,” no. December, 2014, doi: 10.1007/s11051-014-2788-1.
- [86] V. R. Khabibullin, D. M. V. Ratova, D. N. Stolbov, I. V. Mikheev, and M. A. Proskurnin, “The Thermophysical and Physicochemical Properties of the Aqueous Dispersion of Graphene Oxide Dual-Beam Thermal Lens Spectrometry,” *Nanomaterials*, vol. 13, no. 14, 2023, doi: 10.3390/nano13142126.
- [87] J. Chen and L. Li, “Effect of oxidation degree on the thermal properties of graphene oxide,” *J. Mater. Res. Technol.*, vol. 9, no. 6, pp. 13740–13748, 2020, doi: 10.1016/j.jmrt.2020.09.092.

الملخص

تُظهر المواد النانوية المركبة من الذهب وأكسيد الحديد المغناطيسي المدعومة على أكسيد الغرافين ($\text{Au@Fe}_3\text{O}_4\text{-GO}$) كفاءةً عاليةً في التحفيز الكيميائي، مما يجعلها مرشحاً واعداً لتصميم أجهزة الاستشعار الكهروكيميائية والتطبيقات الحيوية التحليلية. كما تمتاز بإمكانية استخدامها في التطبيقات الضوئية، وتوصيل الدواء، ومعالجة المياه.

في هذا البحث، تمكّنّا من تحضير وتوصيف المركب $\text{Au@Fe}_3\text{O}_4/\text{GO}$ باستخدام تقنية بديلة حديثة، سهلة التطبيق، منخفضة التكلفة وغير سامة، وهي (تقنية الاستئصال بالليزر النبضي في السوائل **Pulsed Laser Ablation in Liquid**) وتم تحضير أكسيد الغرافين (GO) في الطور السائل باستخدام التقنية نفسها، ودُرست بنيتها المجهرية باستخدام المجهر الإلكتروني النافذ عالي الدقة (HRTEM)، كما تم تحديد المجموعات الوظيفية بواسطة مطيافية الأشعة تحت الحمراء بتحويل فوريير (FTIR) كذلك، جرى قياس أطياف الامتصاص البصري للعينات باستخدام مطياف الأشعة فوق البنفسجية – المرئية (UV-Vis)

تم تحميل مغنتيت (Fe_3O_4) على صفائح أكسيد الغرافين لتكوين المركب $\text{Fe}_3\text{O}_4/\text{GO}$ ، ثم تم تحضير المركب $\text{Au@Fe}_3\text{O}_4/\text{GO}$ باستخدام تقنية PLAL بنسب مختلفة من $\text{Au@Fe}_3\text{O}_4$ إلى GO، ($S1=1:1$)، ($S2=1:2$)، ($S3=1:3$ و $S4=1:4$) جرى توصيف المواد المركبة الناتجة بالطريقة ذاتها، وحُسبت المعاملات البصرية التالية: الناقلية البصرية (σ)، معامل الامتصاص (α)، فجوة الطاقة (E_g)، طاقة أورباخ (EU)، الكهرسالية (Δx)، معامل الانكسار (n)، معامل الانحدار (σ_s)، تفاعل الإلكترون-الفونون (E-p)، الاستقطابية الإلكترونية (α_e)، والاستقطابية الإلكترونية المولية (ame) أظهرت النتائج تحسناً ملحوظاً في هذه الخصائص مع إضافة Fe_3O_4 ، كما لوحظ تعزيز إضافي عند إدخال الذهب (Au) إلى البنية المركب.

إضافةً إلى ذلك، تم قياس الخصائص الحرارية — وتشمل الانتشارية الحرارية (α)، الانفعالية الحرارية (e)، والناقلية الحرارية (k) لمركبات GO، و $\text{Fe}_3\text{O}_4/\text{GO}$ ، و $\text{Au@Fe}_3\text{O}_4/\text{GO}$ باستخدام (تقنية التحليل الصوت الضوئي **Photoacoustic Tech**) وأظهرت النتائج تحسناً في القيم الحرارية α و k للمواد $\text{Au@Fe}_3\text{O}_4/\text{GO}$ مقارنةً بمركبات GO. و $\text{Fe}_3\text{O}_4/\text{GO}$ كما تبين أن زيادة نسبة GO إلى أربعة أضعاف نسبة $\text{Au@Fe}_3\text{O}_4$ أدت إلى انخفاض في الناقلية الحرارية (k) بنسبة تصل إلى 200%.

تعريف بمقدم الرسالة

الاسم	: بسمة سعيد حسن علي
تاريخ الميلاد	: 1995 / 4 / 5
محل الميلاد	: القاهرة
اخر درجة جامعية	: بكالوريوس الهندسة الكهربائية
الجهة المانحة	: كلية الهندسة بشبرا – جامعة بنها
تاريخ المنح	: 2019
الوظيفة الحالية	: معيدة



كلية الهندسة بشبرا
FACULTY OF ENGINEERING- SHOUBRA

قسم الفيزيكا والرياضيات الهندسية

بسمه سعيد حسن علي

تحضير وتوصيف أكسيد الجرافين المطعم بمواد نانومترية بطريقة تقنية الاستئصال
بالليزر النبضي

ماجستير العلوم في الهندسة

لجنة الاشراف:

أ.د/ سهير السيد نجم

أ.د/ سعيد عبد الله عبد الحليم

د/ حورية فوزي خطاب

تاريخ البحث :/...../.....

الدراسات العليا:

اجيزت الرسالة بتاريخ :/...../.....

ختم الإجازة:

موافقة مجلس الكلية :/...../.....

موافقة مجلس الجامعة :/...../.....

الموافقة على المنح

كلية الهندسة بشبرا

قسم الفيزيكا والرياضيات الهندسية

تحضير وتوصيف أكسيد الجرافين المطعم بمواد نانومترية بطريقة تقنية الاستئصال

بالليزر النبضي

إعداد

بسمة سعيد حسن علي

لجنة الحكم

التوقيع

الاسم

.....

..... أ.د./

.....

..... أ.د./

.....

..... أ.د./

.....

..... أ.د./

...../...../.....



كلية الهندسة بشبرا
FACULTY OF ENGINEERING- SHOUBRA

قسم الرياضيات والفيزياء الهندسية

تحضير وتوصيف أكسيد الجرافين المطعم بمواد نانومترية بطريقة تقنية الاستئصال بالليزر النبضي

رسالة مقدمة للحصول على درجة ماجستير العلوم

في الرياضيات والفيزياء الهندسة

تخصص الفيزياء الهندسية

اعداد

بسمه سعيد حسن علي

حاصل على بكالوريوس العلوم

في الهندسة الكهربائية

كلية الهندسة، جامعة بنها ، 2019

المشرفون

أ.د/ سهير السيد محمود محفوظ نجم

أ.د/ سعيد عبد الله عبد الحليم

د/ حورية فوزي خطاب